Springer Theses
Recognizing Outstanding Ph.D. Research

Ahmad Borzou

Theoretical and Experimental Approaches to Dark Energy and the Cosmological Constant Problem

Springer

Springer Theses

Recognizing Outstanding Ph.D. Research

Aims and Scope

The series "Springer Theses" brings together a selection of the very best Ph.D. theses from around the world and across the physical sciences. Nominated and endorsed by two recognized specialists, each published volume has been selected for its scientific excellence and the high impact of its contents for the pertinent field of research. For greater accessibility to non-specialists, the published versions include an extended introduction, as well as a foreword by the student's supervisor explaining the special relevance of the work for the field. As a whole, the series will provide a valuable resource both for newcomers to the research fields described, and for other scientists seeking detailed background information on special questions. Finally, it provides an accredited documentation of the valuable contributions made by today's younger generation of scientists.

Theses are accepted into the series by invited nomination only and must fulfill all of the following criteria

- They must be written in good English.
- The topic should fall within the confines of Chemistry, Physics, Earth Sciences, Engineering and related interdisciplinary fields such as Materials, Nanoscience, Chemical Engineering, Complex Systems and Biophysics.
- The work reported in the thesis must represent a significant scientific advance.
- If the thesis includes previously published material, permission to reproduce this must be gained from the respective copyright holder.
- They must have been examined and passed during the 12 months prior to nomination.
- Each thesis should include a foreword by the supervisor outlining the significance of its content.
- The theses should have a clearly defined structure including an introduction accessible to scientists not expert in that particular field.

More information about this series at http://www.springer.com/series/8790

Ahmad Borzou

Theoretical and Experimental Approaches to Dark Energy and the Cosmological Constant Problem

Doctoral Thesis accepted by
Baylor University, Waco, Texas, USA

Springer

Ahmad Borzou
EUCOS-CASPAR, Physics Department
Baylor University
Waco, TX, USA

ISSN 2190-5053 ISSN 2190-5061 (electronic)
Springer Theses
ISBN 978-3-319-69631-7 ISBN 978-3-319-69632-4 (eBook)
https://doi.org/10.1007/978-3-319-69632-4

Library of Congress Control Number: 2017955837

Printed on acid-free paper

This Springer imprint is published by Springer Nature
The registered company is Springer International Publishing AG
The registered company address is: Gewerbestrasse 11, 6330 Cham, Switzerland

To Paul Adrien Maurice Dirac for his beautiful and inspiring thinking

and

To Razi for being my inspiration.

Supervisor's Foreword

I am very pleased that Springer is publishing Ahmad Borzou's exceptional and unique dissertation entitled "Theoretical and Experimental Approaches to the Dark Energy and the Cosmological Constant Problem." The dark energy and cosmological constant problem is a very important question of the field and he tackled this problem both theoretically and experimentally. His dissertation has a unique mixture of the theoretical work discussing the Lorentz theory of gravity and experimental work searching for supersymmetry with the Compact Muon Solenoid (CMS) experiment at the Large Hadron Collider (LHC).

I would like to discuss his experimental research contributions a little more extensively. Although the standard model of particle physics describes many aspects of weak, electromagnetic, and strong interactions, it requires fine tuning to explain the observed value of the Higgs boson mass and it does not provide an explanation for dark matter. Supersymmetry is an attractive theory that can provide some insight into these problems, and in addition provide some solution to the cosmological constant problem as discussed in his dissertation. Supersymmetry search has been one of the major topics at the LHC, especially when Ahmad needed to perform his graduate research, since the supersymmetry discovery reach extended significantly with the LHC's new operation, Run 2, due to the LHC's energy increase after the 2013–2014 machine upgrade.

He joined a team effort of about 30 physicists to search for supersymmetry signatures in the all-hadronic final state with a large imbalance in transverse momentum, where by "all-hadronic" I mean events solely consisting of hadronic jets. Within this team, Ahmad specifically worked on the estimation of one of the most significant backgrounds in this search that mimic the supersymmetry signal, which arises from $t\bar{t}$ and $W+\text{jets}$ production in which the W boson decays to hadronically decaying tau leptons and neutrinos. For estimating this background, he employed an innovative method in which he uses $\mu+\text{jets}$ events in actual pp collision data and replaces this muon with the energy deposit expected from hadronically decaying tau leptons. This tau lepton response template method was used in earlier analyses too, but he made a few innovative improvements. In order

to improve sensitivities for signals with *b*-quarks, search regions are now defined based on the number of jets identified as *b*-quarks (b-jets) in the improved LHC Run 2 analysis. For estimating b-jet multiplicity for the hadronically decaying tau background, he came up with a new approach in which he uses the b-jet multiplicity in μ + jets control sample but additionally takes into account the probability that τ-jets erroneously tagged as b-jets. This improvement was the key to make this search powerful and sensitive to a wide class of supersymmetry signals. The paper reporting on this search was published in the *Physics Letters* journal.

The theoretical aspect of his dissertation is based on his single-author paper on the Lorentz gauge theory of gravity published in the *Classical and Quantum Gravity* journal. Because of the spectacular success of the standard model of particle physics, in this work he sought for a theory of gravity based on gauge theory analogous to the standard model's formulation. I thought it was a good idea, and I was very pleased to see that he carried out this work on his own and expanded this direction of research in his postdoctoral research.

Associate Professor of Physics
Baylor University
Waco, TX, USA

Kenichi Hatakeyama, Ph.D.

Parts of this thesis have been published in the following journal articles:

1. Ahmad Borzou, "A Lorentz Gauge Theory of Gravity", Class. Quantum Grav. 33 (2016) 025008. [arXiv:1412.1199 [gr-qc]]
2. CMS Collaboration, "Search for supersymmetry in the multijet and missing transverse momentum final state in pp collisions at 13 TeV", Phys. Lett. B 758 (2016) 152. [arXiv:1602.06581 [hep-ex]]

Acknowledgments

I would like to begin by thanking the entire CMS collaboration, whose collective hard work makes it possible to study the finest details of our world.

I would like to thank my supervisor Kenichi Hatakeyama for his advice and attention to detail, and for patiently proofreading the excessive number of pages I ended up writing. I must also thank my co-adviser Jay Dittmann for his crucial support that enabled me to finish my analysis and for carefully editing the grammar of my dissertation. I am grateful to Dr. Wang for supporting me, especially in the early years of my PhD program. I found his cosmology course very helpful. I am thankful to Dr. Cleaver for his support of my theoretical work, for his advice, and for his quantum field theory course. I shall thank Dr. Tim Sheng for being one of my dissertation committee members. I would like to thank the Department of Energy for providing support for my research assistantship for 4 years.

My special thanks are due to Dr. Hamid Reza Sepangi who has always been supportive. I always enjoy his recommendations. I would like to express my gratitude to the whole Baylor Physics Department for making a nice and friendly environment so that I could comfortably continue my research. I would like to thank my teachers from elementary school to the present for teaching me.

I am also enormously grateful to my parents, who raised me and supported me throughout this endeavor. I should express my gratitude to my wife Razi for being my best friend and my best companion and always being there for me.

Contents

Chapter 1
Introduction

The cosmological constant problem is one of the most pressing problems of physics at this time. In this dissertation the problem and a set of widely discussed theoretical solutions to this problem are reviewed. It is shown that a recently developed Lorentz gauge theory of gravity can provide a natural solution. In this theory presented here, the metric is not dynamical and it is shown that the Schwartzschild metric is an exact solution. Also, it is proven that the de Sitter space is an exact vacuum solution and as a result the theory is able to explain the expansion of the universe with no need for dark energy. Renormalizability of the theory is studied as well. It is also shown that, under a certain condition, the theory is power-counting renormalizable.

Supersymmetry provides an alternative solution to the cosmological problem as well. The idea behind supersymmetry is reviewed and an experimental search for supersymmetry is presented. The experimental search discussed in this dissertation is based on all-hadronic events with large missing transverse momentum produced in proton-proton collisions at $\sqrt{s} = 13\,\text{TeV}$. The data sample, corresponding to an integrated luminosity of $2.3\,\text{fb}^{-1}$, was collected with the CMS detector at the CERN LHC in 2015. The data are examined in search regions defined with jet multiplicity, tagged bottom quark jet multiplicity, missing transverse momentum, and the scalar sum of jet transverse momenta. The observed numbers of events in all search regions are found to be consistent with the expectations from standard model processes. Exclusion limits are presented for simplified supersymmetric models for pair production of gluinos, supersymmetric partners of gluons. Depending on the assumed gluino decay mechanism, and for a massless, weakly interacting, lightest neutralino, lower limits on the gluino mass from 1440 to 1600 GeV are obtained, significantly extending previous limits.

Assuming the correctness of the standard model of cosmology (ΛCDM), dark energy is believed to dominate the present energy content of the universe, making up around 68% of it. Dark energy is the form of energy with negative pressure responsible for the positive acceleration of the universe at the present time [1]. The standard model of particle physics, on the other hand, predicts a value for

A. Borzou, *Theoretical and Experimental Approaches to Dark Energy and the Cosmological Constant Problem*, Springer Theses,
https://doi.org/10.1007/978-3-319-69632-4_1

the vacuum energy naturally, and this should in principle also be the most likely candidate for the cosmological energy. A dilemma, however, arises when one compares predicted value of the vacuum energy from field theory with the one measured through cosmological observations. They are tens of orders of magnitude different [2]. This is perhaps one of the biggest open problems in physics today.

Generally speaking, two categories of solutions are most plausible. Either general relativity fails at very low energies or there is a correction to the standard model of particle physics. In this dissertation we have tried to study both options in order to better understand the potential and richness of each direction. Here, we study a specific model in each of the two categories. Through these studies, we will be able to see the weaknesses, potentials, and horizons of each category.

To understand how an alternative to general relativity can change the context of dark energy, we have studied a theory that is built on localizing the Lorentz gauge instead of the Poincare gauge and therefore is a Lorentz gauge theory. Our motivation for studying a gauge theory of gravity, rather than many other alternatives, comes from the fact that our best description of nature, the standard model of particle physics, is a gauge theory and it is very likely that a quantum theory of gravity can be developed around the same idea. General relativity is also a gauge theory but is different from the standard model of particle physics in that the former is a geometry of space-time and is not renormalizable while the latter is a description of internal geometries on the space-time and has been successfully renormalized. Therefore, if a formulation of gravity is found in which metric is not dynamical, one can hope to be able to put gravity and the standard model on the same footing. The Lorentz gauge theory has been an attempt to construct such a formulation. Here, using the power counting method, it is shown that the theory has a predictable quantum behavior and should not be ultraviolet divergent like general relativity. Any alternative to general relativity should first pass the tests that general relativity has already passed. Since most of these tests are performed within the solar system, a description of such a static and spherically symmetric space-time is essential for a new theory to be acceptable. For this reason we have also studied this case and have shown that the Schwarzschild space-time is an exact solution of the theory, which itself means that it passes most of the tests that general relativity has passed. It is also shown that the de Sitter space-time, which explains an exponentially expanding space-time, is an exact solution of the theory *without requiring dark energy*. Therefore, it is possible to explain the positive rate expansion of the universe without the need to introduce dark energy. In spite of this solution, we still cannot claim that the expansion of the universe is explained by the Lorentz gauge theory since the consistency of other cosmological observations has not yet been tested. This will be the subject of future studies.

The possibility that there are corrections to the standard model of particle physics and therefore the vacuum energy is not as large as what is predicted today is another workaround for the problem of dark energy, i.e., the cosmological constant problem. One can imagine that if there exist some other particles that are not yet listed in the standard model, they also will contribute to the vacuum energy. If contributions from different elements cancel each other in the end, the value for

the vacuum energy may be far smaller—consistent with the cosmological value. Supersymmetry is a well-motivated option. Here, by allowing anti-commutators in the group algebra, a rich framework arises that allows as many superparticles as particles in the standard model. One can hope that these new particles have the properties needed to obtain the appropriate cancellation in the vacuum energy. Since the theoretical development of supersymmetry has been done a long time ago and there is not much work to do on the theoretical aspects, I have focused on an experimental search for the superparticles. Here we target a search for pair production of gluinos, supersymmetric partners of gluons, which is motivated by phenomenological studies that suggest higher cross sections for these interactions than for the production of other superparticles. This is an inclusive search for supersymmetry performed using all-hadronic events with large missing transverse momentum produced in proton-proton collisions at a center of mass energy of 13 TeV. The data sample corresponds to an integrated luminosity of $2.3\,\text{fb}^{-1}$ and was collected in 2015 with the Compact Muon Solenoid (CMS) detector at the Large Hadron Collider. The search is performed using the H_T, H_T^miss, N_jet, and $N_\text{b-jet}$ variables. The data were consistent with the background predictions from standard model processes and therefore no supersymmetric signal was observed. Depending on the assumed gluino decay mechanism, and in the limit of a massless, weakly interacting lightest neutralino, a lower mass limit from 1440 to 1600 GeV is determined for the gluino.

This dissertation is organized as follows. In Chap. 2, the standard model of cosmology is first described and then the problem of dark energy is illustrated. Chapter 3 is devoted to the construction of a gravitational theory based on the Lorentz gauge. Here it is shown how the positive expansion of the universe can be explained without adding an unknown dark energy but instead by modifying gravity. In Chap. 4, a brief review of the standard model of particle physics is given, and we review supersymmetric theories and their possible solutions to the problem of dark energy. Here it is emphasized why an experimental search for supersymmetric particles is crucial. Chapter 5 gives an overall view of the Large Hadron Collider (LHC), while in Chap. 6 the CMS detector is described in detail. Chapter 7 details our experimental search for supersymmetric particles. The materials of this chapter are first published by the CMS collaboration.

References

1. P.J.E. Peebles, B. Ratra, Rev. Mod. Phys. **75**, 2 (2003) [arXiv:astro-ph/0207347]
2. S. Weinberg, Rev. Mod. Phys. **61**, 1 (1989) [arXiv:astro-ph/0005265]

Chapter 2
Dark Energy

2.1 Introduction

Soon after Einstein published his general theory of relativity, in order to derive a static solution out of his equations, he modified the equations by adding Λ, the cosmological constant term [1]. This extra term could be used to explain the observations of that time that were indicating a non-evolving universe. Although Einstein may not have been aware of this fact originally, this cosmological constant can be interpreted as the vacuum energy density [2], which generates a repulsive force that can balance the attractive gravitational forces due to matter and hence grant a static, although extremely unstable, universe. The cosmological term seemed unnecessary when Hubble observed the cosmic expansion of the universe [3], and Friedmann [4] and Lemaitre [5] developed a model that could well explain the new data. Therefore, Einstein and de Sitter [6] accepted a spatially flat, matter dominated, homogeneous, isotropic, and expanding universe as the cosmological model where the matter density (ρ_m) is equal to the critical density (ρ_c), $\Omega_m \equiv \frac{\rho_m}{\rho_c} = 1$, and there is no room for other types of energy. In the 1990s, two independent groups of cosmologists [7, 8] reported direct evidence of cosmic expansion with a positive rate from studies of supernova explosions, although other studies of the age of the universe together with cosmic microwave background (CMB) observations [9] were already indicating the shortcomings of the Einstein–de Sitter model.

Before moving forward any further, we would like to pause here and mathematically demonstrate the cosmological model with a constant vacuum energy. To start, one needs to make an assumption about the form of the metric that best represents the symmetries of the space-time one wishes to investigate. For a spatially homogeneous and isotropic space-time the metric can be written as

$$ds^2 = dt^2 - a^2(t)\left(\frac{dr^2}{1-kr^2} + r^2[d\theta^2 + \sin^2\theta d\phi^2]\right), \tag{2.1}$$

A. Borzou, *Theoretical and Experimental Approaches to Dark Energy and the Cosmological Constant Problem*, Springer Theses,
https://doi.org/10.1007/978-3-319-69632-4_2

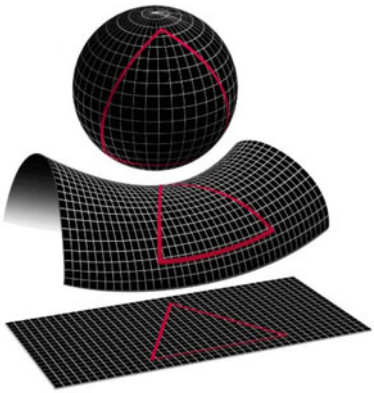

Fig. 2.1 Illustration of the geometry of the universe for a closed universe (top), an open universe (middle), and a flat universe (bottom): Adapted from the NASA/WMAP Science Team [10]

where $a(t)$ is the scale factor showing the expansion and contraction of the space-time and k can be 1, 0, or -1. If $k = -1$, spatial hypersurfaces have positive curvature and are usually called closed spaces. In such a universe, two parallel beams of light eventually converge at some point. If $k = 0$, the spatial hypersurfaces have zero curvature and are called flat. Here two parallel beams of light will remain parallel forever. Finally, if $k = 1$, the curvature of the hypersurfaces is negative and we get an open universe. In such a universe two parallel beams of light diverge. Figure 2.1 illustrates the concepts. In a flat universe, the sum of angles in radians of a triangle adds up to exactly π. In an open universe the summation of angles is less than π. In a closed universe this summation is more than π. Note that here the signature of our metric is chosen to be $(1, -1, -1, -1)$. The curvature of our universe can be measured by studying the fluctuations in the CMB. If the universe is flat, the brightest fluctuations in the CMB would be about 1° across. A larger angle means a closed universe while a smaller angle means an open universe. The WMAP [10] and Planck [11] satellites have investigated these fluctuations to very high accuracy, with the results in favor of a flat universe.

The energy-momentum distribution should also be homogeneous and isotropic. For the case of a perfect fluid it can be written in the following form:

$$T_{\mu\nu} = \begin{pmatrix} \rho(t) & 0 & 0 & 0 \\ 0 & -p(t) & 0 & 0 \\ 0 & 0 & -p(t) & 0 \\ 0 & 0 & 0 & -p(t) \end{pmatrix}, \tag{2.2}$$

where ρ is the matter density of the universe and p is the pressure. We usually consider two different types of energy-momentum. The first is radiation with $p = \frac{\rho}{3}$ and the second is matter with almost no pressure $p = 0$. Now all we need to do, in order to have the dynamics of the universe, is to insert Eqs. (2.1) and (2.2) into the Einstein's field equations[1]

[1]Natural units are in place in this dissertation.

$$R_{\mu\nu} - \frac{1}{2} g_{\mu\nu} R + \Lambda g_{\mu\nu} = 8\pi G T_{\mu\nu}, \tag{2.3}$$

resulting in the Friedmann equations which, after combining, take the form

$$\left(\frac{\dot{a}}{a}\right)^2 = H^2 = \frac{8\pi G\rho}{3} - \frac{k}{a^2} + \frac{\Lambda}{3}, \tag{2.4}$$

$$\frac{\ddot{a}}{a} = -\frac{4\pi G}{3}(\rho + 3p) + \frac{\Lambda}{3}. \tag{2.5}$$

One can rewrite Eq. (2.4) as

$$H^2 = H_0^2 \left(\frac{8\pi G\rho}{3H_0^2} - \frac{k}{a^2 H_0^2} + \frac{\Lambda}{3H_0^2}\right), \tag{2.6}$$

where H_0 is the Hubble constant and equals the present value of H. This equation in turn can be written in a more formal way as

$$H^2 = H_0^2 \left(\Omega_m \frac{\rho}{\rho_0} + \frac{\Omega_k}{a^2} + \Omega_\Lambda\right), \tag{2.7}$$

where

$$\begin{aligned} \Omega_m &= \frac{8\pi G\rho_0}{3H_0^2}, \\ \Omega_k &= -\frac{k}{H_0^2}, \\ \Omega_\Lambda &= \frac{\Lambda}{3H_0^2}. \end{aligned} \tag{2.8}$$

The subscript "0" indicates the present value of the quantities. Now we would like to know how the density of matter or radiation changes as a function of the scale factor, $a(t)$. For this we can use the conservation of energy-momentum tensor

$$\nabla_\mu T^\mu_{\ \nu} = \partial_\mu T^\mu_{\ \nu} + \Gamma^\mu_{\alpha\mu} T^\alpha_{\ \nu} - \Gamma^\alpha_{\nu\mu} T^\mu_{\ \alpha} = 0, \tag{2.9}$$

which contains four different equations. Here we only choose to deal with one of them and therefore substitute $\nu = 0$. The resulting equation is

$$-\frac{\partial\rho}{\partial t} - \Gamma^\mu_{0\mu}\rho - \Gamma^\alpha_{0\mu} T^\mu_{\ \alpha} = 0, \tag{2.10}$$

therefore

$$\frac{\partial\rho}{\partial t} + \frac{\dot{a}}{a}[3\rho + 3p] = 0. \tag{2.11}$$

For matter, $p = 0$, which yields

$$\frac{1}{\rho}\frac{\partial \rho}{\partial t} = -3\frac{\dot{a}}{a}. \tag{2.12}$$

A simple integration of this gives

$$\rho = \frac{\rho_0}{a^3}. \tag{2.13}$$

On the other hand, for the radiation case we have $p = \frac{\rho}{3}$, which results in

$$\frac{1}{\rho}\frac{\partial \rho}{\partial t} = -4\frac{\dot{a}}{a}, \tag{2.14}$$

and therefore gives

$$\rho = \frac{\rho_0}{a^4}. \tag{2.15}$$

The last two equations indicate that as the universe expands, the energy density of relativistic matter falls faster than that of nonrelativistic matter. This in turn means that at early times the universe was radiation-dominated, while after a crossing point, the density of matter is much greater and the universe becomes matter-dominated. These results can be used to rewrite Eq. (2.7) as

$$H^2 = H_0^2\left(\frac{\Omega_r}{a^4} + \frac{\Omega_m}{a^3} + \frac{\Omega_k}{a^2} + \Omega_\Lambda\right), \tag{2.16}$$

where Ω_r and Ω_m are radiation and matter densities. Here, one can conclude that after a long period of time, all of the densities vanish except that of the cosmological constant. Eventually the universe will be dominated by the cosmological constant. Evaluating this equality at the present time and substituting $a_0 = 1$, where the naught stands for the present time, we can conclude that

$$\Omega_r + \Omega_m + \Omega_k + \Omega_\Lambda = 1. \tag{2.17}$$

As was discussed earlier, current observations are all in favor of a flat universe with the consequence that $\Omega_k = 0$. Moreover, the radiation density at the current epoch of universe is perfectly negligible ($\Omega_r = 0$), and therefore

$$\Omega_m + \Omega_\Lambda = 1. \tag{2.18}$$

There have been several different attempts to measure the density of matter in the universe. The most accurate results come from data recently announced by the Planck collaboration [11]. An illustration of the best-fit confidence regions is shown

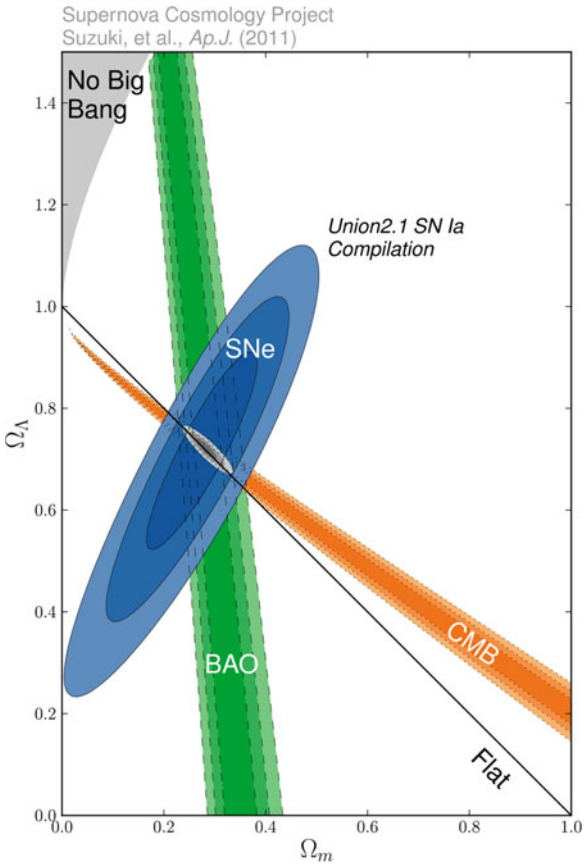

Fig. 2.2 Best fits regions in the $\Omega_m - \Omega_\Lambda$ plane obtained from a combination of different measurements on Type-Ia supernova (SN Ia), CMB, and baryon acoustic oscillations (BAO). Three curves around Supernovae (SNe), BAO, and CMB show 68.3, 95.4, and 99.7% confidence regions from each constraint: Adapted from the Supernova Cosmology Project [12]

in Fig. 2.2. Here, the Type-Ia supernova (SN Ia) data is combined with the expected Planck data to have an error of the size of the overlapped region. This plot suggests a matter density of $\Omega_m \simeq 0.3$ and dark energy density of $\Omega_\Lambda \simeq 0.7$.

Now that a sense of the energy content of the universe is reached, it can be used to work out the dynamics of the universe using the second set of Einstein's field equations in Eq. (2.5). In a universe with no dark energy, the equation has a positive rate expansion, $\ddot{a} > 0$, if

$$\rho + 3p < 0. \tag{2.19}$$

It is almost impossible to find matter with negative density and therefore we can safely assume that $\rho > 0$. Thus, the above equation indicates that pressure should be negative. The simplest model with a negative pressure is the cosmological constant. It can be shown that the equation of state for the vacuum energy is

$$p = -\rho, \tag{2.20}$$

which means

$$\rho + 3p = \rho - 3\rho = -2\rho, \tag{2.21}$$

which is negative due to the positiveness of ρ, and therefore as stated in Eq. (2.19), results in an expansion with positive rate.

2.2 The Cosmological Constant Problem

As was noted in the past section, around 70% of the energy content of our universe is made of an unknown dark energy. This has been confirmed by several different observations. A combination of all the experiments and the general theory of relativity suggest a model called Λ CDM that consists of a vacuum energy (Λ) and cold dark matter (CDM) and can explain all the current observations. However, there are also shortcomings. The first difficulty is the problem of fine-tuning, which states the discrepancy between the expected value of the cosmological constant based on the principles of particle physics and the cosmologically observed value. Here is a description of the problem. Lorentz invariance is an important symmetry of particle physics and all of the experimentally established theories of particle physics respect it. To preserve this symmetry, the energy-momentum tensor of the vacuum must take the form

$$\left\langle T_{\mu\nu} \right\rangle = \langle \rho \rangle \, g_{\mu\nu}. \tag{2.22}$$

One may argue that energy of the vacuum is not physically important, but in field theory, a zero point energy exists whose value is more than zero. This energy exists even when all the fields vanish. The effect of this vacuum energy was shown by Casimir [13] and was experimentally measured by Sparnaay [14]. Casimir considered the case of two conductor plates parallel to each other. He argued that the vacuum energy between the two plates is governed by the boundary condition that the two plates define. Here Casimir showed the quantum fluctuations within the two plates generate a force inversely proportional to the fourth power of the distance between the two plates. Sparnaay's experiment indicated the realness of this vacuum energy.

At this point we would like to calculate the expected amount of the vacuum energy. For the sake of simplicity, we restrict our calculations to a scalar field where

$$\Phi(x) = \int \frac{d^3k}{(2\pi)^{\frac{3}{2}}\sqrt{2\omega_k}} (a(\vec{k})e^{-ik\cdot x} + a^\dagger(\vec{k})e^{ik\cdot x}), \tag{2.23}$$

and

$$\left[a(\vec{k}), a^\dagger(\vec{k'})\right] = \delta^3(\vec{k} - \vec{k'}). \tag{2.24}$$

Knowing that the conjugate momentum of the scalar field is $\Pi(x) = \dot{\Phi}(x)$, the Hamiltonian of the field can be easily worked out:

$$H = \int d^3x \, (\Pi^2 + \vec{\nabla}\Phi \cdot \vec{\nabla}\Phi + m^2\Phi^2). \tag{2.25}$$

Substituting the field defined by Eq. (2.23) and its conjugate momentum into the Hamiltonian above gives a very simple expression in terms of the harmonic oscillator's basic operators:

$$H = \int d^3k \, \frac{1}{2}\omega_k(a^\dagger(\vec{k})a(\vec{k}) + a(\vec{k})a^\dagger(\vec{k})), \tag{2.26}$$

which can be further simplified using Eq. (2.24):

$$H = \int d^3k \, \omega_k a^\dagger(\vec{k})a(\vec{k}) + \frac{1}{2}\int d^3k \, \omega_k \delta^3(0). \tag{2.27}$$

Now we can use the identity that

$$\delta^3(0) = \int d^3x = V, \tag{2.28}$$

where V is the volume of the space. Energy of the vacuum is just the eigenvalue of this Hamiltonian when the system, the universe, is in its ground state $H\,|0\rangle = E_{\text{vac}}\,|0\rangle$. Knowing that $a(\vec{k})\,|0\rangle = 0$,

$$H\,|0\rangle = \frac{1}{2}V\int d^3k \, \omega_k \,|0\rangle\,, \tag{2.29}$$

and therefore

$$E_{\text{vac}} = \frac{1}{2}V\int d^3k \, \omega_k. \tag{2.30}$$

The density of vacuum energy is just this energy divided by the volume

$$\rho_{\text{vac}} = \frac{1}{2}\int d^3k \, \omega_k = \frac{1}{2}\int k^2 dk \, d\Omega \, \sqrt{k^2 + m^2} = \frac{4\pi}{2}\int_0^{M_{\text{cutoff}}} dk \, k^2\sqrt{k^2 + m^2}. \tag{2.31}$$

By working this integral out, one can see that the vacuum energy density is proportional to the fourth power of the cutoff mass

$$\rho_{\text{vac}} \sim M^4_{\text{cutoff}}. \tag{2.32}$$

The cutoff mass can be assumed to be the scale where gravity is not negligible ($M_{\text{cutoff}} \sim 10^{19}\,\text{GeV}$). Therefore,

$$\rho_{\text{vac}} \sim 10^{76}\,\text{GeV}^4. \tag{2.33}$$

This density is extremely higher than what is observed. As discussed in the preceding section, observation suggests a vacuum density of $\Omega_\Lambda = \frac{\Lambda}{3H_0^2} \sim 0.7$. Hence the observed vacuum density is

$$\rho_{\text{obs}} = \Lambda = 2.1H_0^2 \sim 10^{-47}\,\text{GeV}^4. \tag{2.34}$$

Here the disaster can be felt by calculating the ratio of the expected over the observed vacuum density

$$\frac{\rho_{\text{exp}}}{\rho_{\text{obs}}} \sim 10^{123}. \tag{2.35}$$

2.3 Proposed Solutions to the Dark Energy Problem

Several different solutions to the cosmological constant's fine-tuning problem have been proposed. These can be categorized into two main categories. The first category contains modified models of matter for which there is an unknown type of matter with a negative pressure. The second category contains modified theories of gravity for which there usually is no need for dark energy and the modified sector of gravity is in fact in charge of the late expansion of the universe. In the following subsections we compare a few arbitrary but well-studied models by presenting their attractive aspects and potential new problems that they raise.

2.3.1 Models of Modified Matter

Quintessence is one of the earliest alternatives to the cosmological constant [15–18]. Here, the unknown matter is a scalar field that varies with time and rolls toward the stable point of its potential. The unknown matter is introduced by the following action:

$$S = \int d^4x\,\sqrt{-g}\left[-\frac{1}{2}g^{\mu\nu}\partial_\mu\phi\partial_\nu\phi - V(\phi)\right]. \tag{2.36}$$

Variation of this action with respect to the metric gives the energy-momentum tensor and subsequently the energy density as well as the pressure:

$$\rho = \frac{1}{2}\dot{\phi}^2 + V(\phi),$$
$$p = \frac{1}{2}\dot{\phi}^2 - V(\phi). \tag{2.37}$$

Therefore, the equation of state is

$$\omega = \frac{p}{\rho} = \frac{\dot{\phi}^2 - 2V(\phi)}{\dot{\phi}^2 + 2V(\phi)}. \tag{2.38}$$

On the other hand, the condition for positive rate expansion is $\omega < -\frac{1}{3}$, which indicates that the following condition should hold:

$$\dot{\phi}^2 < V(\phi). \tag{2.39}$$

There are several different suggested potentials that can be listed under the following types: "freezing," "thawing," and "tracker" [18–20]. In general all of them can explain the smallness of the value of the energy density at the present time. However, this does not mean they have solved the cosmological constant problem. This is because the value of the Quintessence energy density will be close to today's critical energy density only if the Quintessence potential is fine-tuned by itself.

Another modified model that has been around for a long time is called k-essence. Here the idea is to introduce a noncanonical, nonlinear, kinetic term in Eq. (2.36) that leads to a negative pressure independent of the potential term [21]. The nonlinear kinetic energy terms are thought to be small and usually ignored since they will become inconsequential by the Hubble expansion. However, if an attractor solution exists that makes the nonlinear kinetic terms non-negligible, the negative pressure can be explained [22, 23]. Here the term attractor means there is a point for which every nearby point is attracted to it. In our case it means the k-essence term is attracted to an equation of state, different from matter or radiation, or the equation of state of the background component in the universe. A k-essence action is usually described by

$$S = \int d^4x \sqrt{-g} p(\phi, X), \tag{2.40}$$

where $X = \frac{1}{2}\partial_\mu\phi\partial^\mu\phi$ and $p(\phi, X)$ is the pressure. For some specific forms of this pressure term, the scalar field will obtain the equation of state of dark energy. One general concern about k-essence theories is their allowance of superluminal speeds. However, as was shown in [24], this may not lead to a paradox.

The fact that energy density of dark matter and dark energy are of the same order at the present time has led several people to suspect that there is a connection between the two. The resulting theories are called "coupled dark energy and matter" [25–27]. Here the dark energy and dark matter are related through the following conservation equations:

$$\dot{\rho}_m + 3H\rho_m = \delta,$$
$$\dot{\rho_\phi} + 3H(\rho_\phi + p_\phi) = -\delta, \tag{2.41}$$

where ϕ refers to dark energy, m refers to dark matter, and δ is a term to allow flow of energy between the two components and is a function of ρ_m and ρ_ϕ in general.

2.3.2 Models of Modified Gravity

There are several different classes of modified theories of gravity. In one class the idea is that instead of modifying the right-hand side, that is the matter section of general relativity, one can modify the left-hand side of the equations and therefore assume no dark energy. In general all the variants of this class are a special case of the following action:

$$S = \int d^4x \sqrt{-g}(R + a_1R^2 + a_2R_{\mu\nu}R^{\mu\nu} + \cdots). \tag{2.42}$$

Therefore, the modifications appear as higher derivative terms giving more degrees of freedom to the field. Perhaps the simplest model in this class is $f(R)$ gravity represented by

$$S = \int d^4x \sqrt{-g}f(R), \tag{2.43}$$

where $f(R)$ is an arbitrary function of the Ricci scalar. One can show, using the conformal transformation $g_{\mu\nu} \rightarrow \frac{\partial f}{\partial R}g_{\mu\nu}$, that $f(R)$ gravity is equivalent to general relativity (GR) with an extra scalar field [28, 29]. Just like the case of a scalar field in the previous section, if the slow roll condition is met by the scalar field, an inflationary solution will emerge. To show the details, the field equations are needed. This can be found by varying the action with respect to the metric

$$\frac{\partial f}{\partial R}R_{\mu\nu} - \frac{1}{2}fg_{\mu\nu} - \nabla_\mu\nabla_\nu\frac{\partial f}{\partial R} + g_{\mu\nu}\nabla_\alpha\nabla^\alpha\frac{\partial f}{\partial R} = 8\pi GT_{\mu\nu}. \tag{2.44}$$

Taking a trace and multiplying by $g^{\mu\nu}$ yield

$$\frac{\partial f}{\partial R}R - 2f + 3\nabla_\alpha\nabla^\alpha\frac{\partial f}{\partial R} = 8\pi GT. \tag{2.45}$$

An inflationary scenario can be reached if we assume a constant curvature R with no matter, $T = 0$, which is just a de Sitter space. Substituting these into the above equation gives

$$\frac{\partial f}{\partial R}R - 2f = 0. \tag{2.46}$$

Hence, if a model of $f(R)$ gravity satisfies this equation, the present accelerating expansion of the universe can be reached. Although $f(R)$ theories of gravity have some promising features, there is yet no well-established model of them. This is because of an extended range of conditions they need to satisfy. One drawback that many theories of higher derivatives are facing is existence of massive fields with negative norm, referred to as "ghosts," which violates unitarity [30, 31] although $f(R)$ theories are generally claimed to be ghost free [30]. Stability is another condition that any theory of gravity must respect. A massive field theory is in general unstable if its mass is complex. From this we can claim that only models with $\frac{\partial^2 f(R)}{\partial R^2} \geq 0$ are stable. This means a model defined with $f(R) = R - \frac{1}{R}$ is unstable. However, these are models that have non-negligible effects at low energies, equivalently at the present time. It is still possible to introduce models that meet all of the above-mentioned conditions [32]. In the end when all of the conditions are met and assuming no further difficulty will arise, one still can question why the kinetic part of the model is not the same as all of the well-established and empirically verified field theories that are all grouped under the standard model.

Another well-studied class of modified gravity comes with the idea that there may exist a fifth dimension or more that gives rise to the late accelerating expansion. The most prominent of these is perhaps the brane world model of Dvali et al. [33]. In this model, our universe is built on a four-dimensional brane floating in a five-dimensional bulk. Every field is constrained to live on the brane except gravity that can also exist in the extra dimension. This can also explain why gravity is so weak with respect to the other three fundamental forces. However, this model suffers from a ghost problem [34] which may be cured by introducing extra terms [35, 36]. The model is disfavored by the SN Ia, BAO, and CMB data [37].

Recently we have developed a Lorentz gauge theory of gravity for the purpose of curing the high energy ultraviolet divergences in general relativity. Here we have noticed that the de Sitter space is the natural exact solution of the theory without assuming an unknown form of matter or energy. Also, supersymmetry has several attractive features among which one can find promising solutions to the problem of dark energy. We will review these last two theories in the following two chapters.

References

1. A. Einstein, Sitzungsber. Preuss. Akad. Wiss. Berlin (Math. Phys.) **1915**, 844 (1915)
2. Y.B. Zeldovich, Sov. Phys. Uspekhi **11**, 381 (1968)
3. E. Hubble, Proc. Natl. Acad. Sci. **15**, 168 (1929)
4. A. Friedmann, On the curvature of space. Z. Phys. **10**, 377 (1922)
5. G. Lemaitre, Annales de la Societe Scietifique de Bruxelles **47**, 49 (1927)
6. A. Einstein, W. de Sitter, Proc. Natl. Acad. Sci. **18**, 213 (1932)
7. A.G. Riess et al., [Supernova Search Team Collaboration], Astron. J. **116**, 1009 (1998)

8. S. Perlmutter et al., [Supernova Cosmology Project Collaboration], Astrophys. J. **517**, 565 (1999)
9. C.L. Bennett, A.J. Banday, K.M. Górski, G. Hinshaw, P. Jackson, P. Keegstra, A. Kogut, G.F. Smoot, D.T. Wilkinson, E.L. Wright, Astrophys. J. Lett. **464**, L1 (1996)
10. http://map.gsfc.nasa.gov/site/citations.html. Accessed 12 Oct 2010
11. Planck Collaboration, Planck 2015 results. XIII. Cosmological parameters (2015) [arXiv:1502.01589]
12. N. Suzuki et al., [The Supernova Cosmology Project], Astrophys. J. **746**, 85 (2012) [arXiv:1105.3470]
13. H.B.G. Casimir, Proc. K. Ned. Akad. Wet. **51**, 793 (1948)
14. M.J. Sparnaay, Nature **180**, 334 (1957)
15. C. Wetterich, Nucl. Phys. B **302**, 668 (1988)
16. B. Ratra, P. Peebles, Phys. Rev. D **37**, 3406 (1988)
17. R. Caldwell, R. Dave, P.J. Steinhardt, Phys. Rev. Lett. **80**, 1582 (1998) [arXiv:astro-ph/9708069]
18. I. Zlatev, L.M. Wang, P.J. Steinhardt, Phys. Rev. Lett. **82**, 896 (1999) [arXiv:astro-ph/9807002]
19. S. Weinberg, Rev. Mod. Phys. **61**, 1 (1989) [arXiv:astro-ph/0005265]
20. R. Caldwell, E.V. Linder, Phys. Rev. Lett. **95**, 141301 (2005) [arXiv:astro-ph/0505494]
21. C. Armendariz-Picon, T. Damour, V.F. Mukhanov, Phys. Lett. B **458**, 209 (1999) [arXiv:hep-th/9904075]
22. C. Armendariz-Picon, V.F. Mukhanov, P.J. Steinhardt, Phys. Rev. Lett. **85**, 4438 (2000) [arXiv:astro-ph/0004134]
23. C. Armendariz-Picon, V.F. Mukhanov, P.J. Steinhardt, Phys. Rev. D **63**, 103510 (2001) [arXiv:astro-ph/0006373]
24. E. Babichev, V.F. Mukhanov, A. Vikman, JHEP **02**, 101 (2008)
25. C. Wetterich, Astron. Astrophys. **301**, 321 (1995) [arXiv:hep-th/9408025]
26. L. Amendola, Phys. Rev. D **62**, 043511 (2000) [arXiv:astro-ph/9908023]
27. S. Das, P.S. Corasaniti, J. Khoury, Phys. Rev. D **73**, 083509 (2006) [arXiv:astro-ph/0510628]
28. S. Capozziello, S. Carloni, A. Troisi, Recent Res. Dev. Astron. Astrophys. **1**, 625 (2003) [arXiv:astro-ph/0303041]
29. V. Mukhanov, *Physical Foundations of Cosmology* (Cambridge University Press, Cambridge, 2005)
30. I.L. Buchbinder, S.D. Odintsov, I.L. Shapiro, *Effective Actions in Quantum Gravity* (IOP, Bristol, 1992)
31. A. Codello, R. Percacci, Phys. Rev. Lett. **97**, 221301 (2006)
32. T.P. Sotiriou, V. Faraoni, Rev. Mod. Phys. **82**, 451 (2010) [arXiv:0805.1726]
33. G. Dvali, G. Gabadadze, M. Porrati, Phys. Lett. B **485**, 208 (2000) [arXiv:hep-th/0005016]
34. S. Dubovsky, V. Rubakov, Phys. Rev. D **67**, 104014 (2003) [arXiv:hep-th/0212222]
35. C. de Rham, G. Dvali, S. Hofmann, J. Khoury, O. Pujolas et al., Phys. Rev. Lett. **100**, 251603 (2008) [arXiv:0711.2072]
36. A. Nicolis, R. Rattazzi, E. Trincherini, Phys. Rev. D **79**, 064036 (2009) [arXiv:0811.2197]
37. J.Q. Xia, Phys. Rev. D **79**, 103527 (2009) [arXiv:0907.4860]

Chapter 3
A Lorentz Gauge Theory of Gravity

3.1 Introduction

Gauge theories have proven to be very successful in describing the fundamental interactions in physics. There are two different disciplines where the gauge theories work extremely well in terms of explaining the observations. On the one hand, the standard model (SM) is a gauge theory of the group $SU(3) \times SU(2) \times U(1)$, which describes three of the physics interactions in terms of the geometry of internal spaces over space-time. On the other hand, general relativity is a gauge theory of the Poincare group. Although they are both gauge theories, there is a glaring difference in their dynamical variables. In the former, the connections known as the vector bosons are the dynamical variables, while in the latter it is the metric and not the connections that is dynamical. Consequently, the standard model Lagrangian is only a fourth order polynomial, while that of general relativity is not even a polynomial. One, however, can always expand the metric around a classical background which results in a polynomial of infinite orders and the theory becomes more and more divergent as one goes to higher orders in the perturbative expansion. This is why the standard model has been successfully quantized, while general relativity has not until now. An excellent review of the subject is provided in [1]. On the basis of the standard model achievements, a thorough investigation of the relationship between the standard model and gravitational theories might unveil important tips for the quantization of gravity. In this regard, people have pursued two main directions of research. The first direction is to find a duality between a gauge theory and gravity such as AdS/CFT correspondence, introduced by Maldacena and further elaborated by others [2–4]. The work presented in [5], however, lies within

This chapter published as: Ahmad Borzou, "A Lorentz Gauge Theory of Gravity," Class. Quan. Grav., 33 (2016) 025008.

A. Borzou, *Theoretical and Experimental Approaches to Dark Energy and the Cosmological Constant Problem*, Springer Theses,
https://doi.org/10.1007/978-3-319-69632-4_3

the second class, namely, attempts to reformulate gravitational theory as a gauge theory. This is an approach to a gravitational theory that makes the gravitational interactions look more like the interactions that are familiar from the standard model of particle physics. This means recasting the theory from a metric formulation to a formulation of connections of some internal spaces over space-time. This avenue of investigation began with the work of Utiyama [6]. He localized the six parameters of the homogeneous Lorentz group and showed that this consistently gives rise to the Einstein's general relativity. The idea was further extended by the work of Sciama and Kibble [7, 8] by showing that a localized inhomogeneous Lorentz group realizes a well-defined framework for gravity with torsion. There is a vast literature on the subject, acknowledging it would be an exhausting task. Here we only refer to two of the review papers [9, 10]. Although there has been an enormous progress in placing gravity and the standard model onto one single footing, there are yet some remaining differences. In doing so the main hurdle is the dynamical role of the metric. Here we would like to study a formulation of gravity in which the metric is nondynamical. From the equivalence principle we know that at any point in space-time there is a free falling frame which comes with a unique feature, namely, being both a Lorentz and a coordinate frame. This fact enables one to split a given tetrad field into two parts. The first part contains the angle between the free falling frame and the arbitrarily chosen Lorentz frame at that point. The second part contains the angle between the free falling frame and that associated with the arbitrarily chosen coordinates at that point. In a more rigorous language

$$e_{i\mu} = \eta^{\bar{k}\bar{l}} e_{i\bar{k}} e_{\bar{l}\mu}, \tag{3.1}$$

where the bar indicates the free falling frame, while the Latin indices refer to the Lorentz frames and the Greek ones refer to the coordinate systems. Dynamics in the tetrad can be originated from either of the two constituents. Namely,

$$\delta e_{i\mu} = \begin{cases} \eta^{\bar{k}\bar{l}} e_{i\bar{k}} \delta e_{\bar{l}\mu} & \text{Case I,} \\ \eta^{\bar{k}\bar{l}} \delta e_{i\bar{k}} e_{\bar{l}\mu} & \text{Case II.} \end{cases} \tag{3.2}$$

The first case leads to the general theory of relativity and is not the subject of this chapter. The second case develops no dynamics in the metric. This is because the metric is independent of the choice of the Lorentz frame

$$g_{\mu\nu} = \eta^{ij} e_{i\mu} e_{j\nu} = \eta^{\bar{i}\bar{j}} e_{\bar{i}\mu} e_{\bar{j}\nu}.$$

Therefore, $\delta g_{\mu\nu} = 0$ in the latter case. This, however, doesn't mean that the metric is not affected at all. As will be shown later, this approach establishes a formulation with a propagating spin connection. In the presence of a nonzero connection the difference between two neighboring free falling frames does not vanish and therefore space-time departs from a Minkowskian form.

This chapter is organized as follows. A brief review of the tetrad formalism is presented in Sect. 3.2. In Sect. 3.3 the Lorentz gauge theory is introduced by a Lagrangian, where the conservation laws as well as the field equations are derived. Here, like the very original work of Utiyama, we employ the spin connections, gravitational gauge fields, to preserve the local homogeneous Lorentz invariance. Next, a weak field solution is found for a spherically symmetric space-time, where we show that it is the Schwarzschild solution at least to the first order of perturbation. In Sect. 3.4, to make the theory more like the standard model, a special case is introduced, where it is shown that the Schwarzschild as well as the de Sitter spaces are two exact vacuum solutions. Quantization of the theory is briefly studied next. Propagator of the gauge field and also the principal vertices are derived as well. Then it is shown that, under a certain condition, the theory is at least power-counting renormalizable. A conclusion of this chapter is presented in Sect. 3.5.

3.2 A Brief Review of the Tetrad Formalism

General relativity successfully describes gravity in the macroscopic level. To this level matter is sufficiently well represented by the energy momentum tensor. However, if one wishes to go down to the microscopic level, classical matter must be replaced by the elementary particles which are characterized not only by their masses but also by their spins. It is well understood that these elementary particles are explained by the Dirac Lagrangian. Therefore, one needs to deal with the Dirac matrices and spinors in a curved space-time. This requires a generalization of their fundamental properties in the flat space-time to more general forms that hold in any curved space-time. A simple breakthrough is to define a tangent space at any point on the manifold and solve physics in those flat Lorentz spaces. It is now necessary to find a connection between the coordinate space and the flat Lorentz spaces. This goal is reached by introducing at each point of the manifold a set of four vector fields, called tetrads. Now the Dirac Lagrangian reads

$$\mathcal{L}_{\text{Dirac}} = i\bar{\psi}\gamma^i e_i{}^\mu \partial_\mu \psi - m\bar{\psi}\psi, \tag{3.3}$$

with $e_i{}^\mu$ being the tetrad field. Here the Latin indices indicate the Lorentz vectors while the Greek indices denote the covariant components of the Lorentz vectors, $\hat{e}_i$, in the curved space-time. Both indices run from zero to three. This Lagrangian is invariant under the global homogeneous Lorentz transformations. Under a local transformation the partial derivative should be replaced by the following relation:

$$\partial_\mu \to D_\mu = \partial_\mu - \frac{1}{2} S^{mn} A_{mn\mu}, \tag{3.4}$$

where the commutator of the Dirac matrices, $S^{mn} = \frac{1}{4}[\gamma^m, \gamma^n]$, is the generator of the homogeneous Lorentz group and the spin connection, $A_{mn\mu}$, is the gauge preserving field. It is not hard to show that under homogeneous Lorentz transformations

$$\delta A_{mn\mu} = D_\mu \omega_{mn} = \partial_\mu \omega_{mn} - A_{mk\mu}\omega^k{}_n - A_{nk\mu}\omega_m{}^k. \tag{3.5}$$

Here ω_{mn} is an antisymmetric tensor that can take any arbitrary value. Since the Lorentz space is flat, the metric on the Lorentz space is always Minkowskian, with a zero covariant derivative in order to preserve angles. This makes the gauge field antisymmetric in the Lorentz indices. The equivalence of the connections in the coordinate and the Lorentz spaces implies the tetrad postulate, which denotes that the covariant derivative of the tetrad field is zero,

$$D_\mu e_{i\nu} = \partial_\mu e_{i\nu} - \Gamma^\alpha_{\mu\nu} e_{i\alpha} - A_{ij\mu} e^j{}_\nu = \nabla_\mu e_{i\nu} - A_{ij\mu} e^j{}_\nu = 0, \tag{3.6}$$

where $\Gamma^\alpha_{\mu\nu}$ are the metric compatible Christoffel symbols

$$\Gamma^\alpha_{\mu\nu} = \frac{1}{2} g^{\alpha\beta}(\partial_\nu g_{\mu\beta} + \partial_\mu g_{\nu\beta} - \partial_\beta g_{\mu\nu}). \tag{3.7}$$

In this dissertation we solely work with a torsion free space indicating that the symbols are symmetric with respect to the two lower indices. Using Eq. (3.6) the spin connections are

$$A_{ij\mu} = e_j{}^\nu \partial_\mu e_{i\nu} - \Gamma^\alpha_{\mu\nu} e_{i\alpha} e_j{}^\nu. \tag{3.8}$$

Using the principle of equivalence we can define at each point X an inertial coordinate system ζ^i in which the equation of motion of a freely falling particle is

$$\frac{d^2\zeta^i}{d\tau^2} = 0. \tag{3.9}$$

A straightforward calculation gives an equation for the Christoffel symbols

$$\Gamma^\lambda_{\mu\nu} = \frac{\partial x^\lambda}{\partial \zeta^\alpha} \frac{\partial^2 \zeta^\alpha}{\partial x_\mu \partial x_\nu}. \tag{3.10}$$

This can be used to find the locally inertial coordinates

$$\zeta^i(x) = e^i{}_\mu(X)(x^\mu - X^\mu) + e^i{}_\mu(X)\Gamma^\mu_{\alpha\beta}(x^\alpha - X^\alpha)(x^\beta - X^\beta) + \cdots. \tag{3.11}$$

More details can be found in [11–13].

3.3 Homogeneous Lorentz Gauge Theory of Gravity

We formally define the homogeneous Lorentz gauge theory by the following action:

$$S = \int e\, d^4x \left[\mathcal{L}_M + \mathcal{L}_A\right]. \tag{3.12}$$

Here e is the determinant of the tetrad field while $\mathcal{L}_M$ specifies the interaction between matter and gravity and is assumed to be the Dirac Lagrangian. A Lagrangian $\mathcal{L}_A$ is needed as well to describe the gauge field itself. The action must remain invariant under both general coordinate and local homogeneous Lorentz transformations which in turn implies the conservation laws. Under an infinitesimal homogeneous Lorentz transformation

$$\delta S = \int d^4x \left[\frac{\delta(e\mathcal{L}_M)}{\delta\psi}\delta\psi + \frac{\delta(e\mathcal{L}_M)}{\delta A_{mn\mu}}\delta A_{mn\mu} + \frac{\delta(e\mathcal{L}_M)}{\delta e_{i\mu}}\delta e_{i\mu}\right] = 0. \tag{3.13}$$

The first term is the Dirac field equation and is zero. Using Eq. (3.5) the second term reads

$$\frac{\delta(e\mathcal{L}_M)}{\delta A_{mn\mu}}\delta A_{mn\mu} = -D_\mu\left(\frac{\delta(e\mathcal{L}_M)}{\delta A_{mn\mu}}\right)\omega_{mn}, \tag{3.14}$$

where the surface term is neglected. We also know that in the third term

$$\delta e_{i\mu} = \omega_{ij}e^j{}_\mu, \tag{3.15}$$

which is because the tetrad transforms like a vector under Lorentz transformations. Therefore, Eq. (3.13) reads

$$\delta S = -\int d^4x \left[D_\mu\left(\frac{\delta(e\mathcal{L}_M)}{\delta A_{mn\mu}}\right) - \frac{1}{2}\frac{\delta(e\mathcal{L}_M)}{\delta e_{m\mu}}e^n{}_\mu + \frac{1}{2}\frac{\delta(e\mathcal{L}_M)}{\delta e_{n\mu}}e^m{}_\mu\right]\omega_{mn} = 0. \tag{3.16}$$

On the other hand ω_{mn} can take any arbitrary value implying that the bracket contains a zero. These altogether grant the conservation law of angular momentum

$$D_\mu\left(\frac{\delta(e\mathcal{L}_M)}{\delta A_{mn\mu}}\right) - \frac{1}{2}\frac{\delta(e\mathcal{L}_M)}{\delta e_{m\mu}}e^n{}_\mu + \frac{1}{2}\frac{\delta(e\mathcal{L}_M)}{\delta e_{n\mu}}e^m{}_\mu = 0. \tag{3.17}$$

Before proceeding further and deriving the field equations, the tetrad field should be investigated a little bit more. Because of the equivalence principle it is always possible to split a given tetrad field at any point X into two parts

$$e_{i\mu}(X) = \eta^{\bar{i}\bar{k}} e_{\bar{i}\bar{j}}(X) e_{\bar{k}\mu}(X). \tag{3.18}$$

This is because it is guaranteed that there exists a free falling frame whose coordinate system is locally Minkowskian, and as a result coincides with one of the possible Lorentz frames at that point which is what is shown with a bar in the equation above and corresponds with a set of four orthogonal unit vectors, $\hat{e}_{\bar{i}}$. Components of these vectors in any arbitrary Lorentz frame are shown with $e_{i\bar{j}}$. On the other hand, components of these free falling unit vectors in any arbitrary coordinate system are shown with $e_{\bar{k}\mu}$. An infinitesimal change in the tetrad field can be established in two ways. The first, which is the subject of the present study, is

$$\delta e_{i\mu}(X) = \eta^{\bar{i}\bar{k}} \delta e_{i\bar{j}}(X) e_{\bar{k}\mu}(X). \tag{3.19}$$

The second one, which results in the theory of general relativity, is well investigated before

$$\delta e_{i\mu}(X) = \eta^{\bar{i}\bar{k}} e_{i\bar{j}}(X) \delta e_{\bar{k}\mu}(X). \tag{3.20}$$

One of the consequences of Eq. (3.19) is that $\delta g_{\mu\nu} = 0$. This is because $g_{\mu\nu} = \eta^{ij} e_{i\mu} e_{j\nu} = \eta^{\bar{i}\bar{j}} e_{\bar{i}\mu} e_{\bar{j}\nu}$ is independent of the chosen Lorentz frame. Another consequence is that

$$\delta A_{ij\mu} = D_\mu (e_j{}^\nu \delta e_{i\nu}). \tag{3.21}$$

This is reached by varying Eq. (3.6) with respect to the tetrad

$$\begin{aligned} &\partial_\mu \delta e_{i\nu} - \delta \Gamma^\alpha_{\mu\nu} e_{i\alpha} - \Gamma^\alpha_{\mu\nu} \delta e_{i\alpha} - \delta A_{ij\mu} e^j{}_\nu - A_{ij\mu} \delta e^j{}_\nu \\ &= D_\mu \delta e_{i\nu} - \delta \Gamma^\alpha_{\mu\nu} e_{i\alpha} - \delta A_{ij\mu} e^j{}_\nu = 0, \end{aligned} \tag{3.22}$$

and the fact that

$$\begin{aligned} \delta g_{\mu\nu} &= 0, \\ \delta \Gamma^\alpha_{\beta\gamma} &= 0. \end{aligned} \tag{3.23}$$

This equation can be used to show that the tetrad field is not propagating at all. This is because a variation of the action in Eq. (3.12) with respect to the tetrad field reads

$$\frac{\delta(e\mathcal{L}_A)}{\delta e_{i\mu}} = -\frac{\delta(e\mathcal{L}_M)}{\delta e_{i\mu}}, \tag{3.24}$$

where

$$\delta(e\mathcal{L}_M) = \frac{\delta(e\mathcal{L}_M)}{\delta A_{ij\mu}} \delta A_{ij\mu} + \frac{\delta(e\mathcal{L}_M)}{\delta e_{i\mu}} \delta e_{i\mu}. \tag{3.25}$$

Using Eq. (3.21) and neglecting the surface terms

$$\begin{aligned}\delta(e\mathcal{L}_M) &= -D_\mu \frac{\delta(e\mathcal{L}_M)}{\delta A_{ij\mu}} e_j{}^\nu \delta e_{i\nu} + \frac{\delta(e\mathcal{L}_M)}{\delta e_{i\mu}} \delta e_{i\mu} \\ &= -D_\mu \frac{\delta(e\mathcal{L}_M)}{\delta A_{ij\mu}} e_j{}^\nu \delta e_{i\nu} + \frac{\delta(e\mathcal{L}_M)}{\delta e_{i\mu}} \left(\frac{1}{2} e^j{}_\mu e_j{}^\nu \delta e_{i\nu} - \frac{1}{2} e^j{}_\mu e_i{}^\nu \delta e_{j\nu} \right) \\ &= -\left[D_\mu \frac{\delta(e\mathcal{L}_M)}{\delta A_{ij\mu}} - \frac{1}{2} \frac{\delta(e\mathcal{L}_M)}{\delta e_{i\mu}} e^j{}_\mu + \frac{1}{2} \frac{\delta(e\mathcal{L}_M)}{\delta e_{j\mu}} e^i{}_\mu \right] e_j{}^\nu \delta e_{i\nu} \\ &= 0, \end{aligned} \tag{3.26}$$

where we have used

$$\begin{aligned} \delta e_{i\mu} &= g^\nu_\mu \delta e_{i\nu} = e^j{}_\mu e_j{}^\nu \delta e_{i\nu}, \\ e_j{}^\nu \delta e_{i\nu} &= -e_i{}^\nu \delta e_{j\nu}, \\ \delta \eta_{ij} &= 0, \end{aligned} \tag{3.27}$$

together with Eq. (3.17). Therefore the right-hand side, the source term, of Eq. (3.24) is zero which means no source exists to generate the tetrad field. It should be emphasized that this result holds only if the variation path is given by Eq. (3.19). If on the other hand the variation path is the one introduced by Eq. (3.20), it results in the general theory of relativity, which is well investigated. As is shown above, however, Eq. (3.19) results in no propagation of the tetrad field. Hence, in order to have a set of field equations, we are left with one option, namely, varying the action with respect to the spin connection and eliminating the tetrad in terms of that. The difficulty now is to write $\delta e_{i\mu}$ in terms of $\delta A_{ij\mu}$. This problem can be solved by the use of the Lagrange multiplier method by inserting the tetrad postulate in the action as a constraint

$$\mathcal{L}_C = S^{\mu\nu i} D_\mu e_{i\nu}, \tag{3.28}$$

where $S^{\mu\nu i}$ is the multiplier. Assuming conservation of parity, the most general Lagrangian for the gauge field is [14, 15]

$$\begin{aligned} \mathcal{L}_A = -\frac{1}{4} \Big(& c_1 F_{\mu\nu ij} e^{i\mu} e^{j\nu} + c_2 F_{\mu\nu ij} F^{\mu\sigma ik} e^{j\nu} e_{k\sigma} + c_3 F_{\sigma\nu mj} F_{\mu\alpha in} e^{j\nu} e^{i\mu} e^{m\sigma} e^{n\alpha} \\ & + c_4 F_{\mu\nu ij} F^{\alpha\beta mn} e^{i\mu} e^j{}_\beta e_{m\alpha} e_n{}^\nu + c_5 F_{\mu\nu ij} F^{\mu\nu ij} \Big), \end{aligned} \tag{3.29}$$

where

$$F_{\mu\nu ij} = \partial_\nu A_{ij\mu} - \partial_\mu A_{ij\nu} + A_i{}^m{}_\mu A_{mj\nu} - A_i{}^m{}_\nu A_{mj\mu}. \tag{3.30}$$

In the following we assume $c_1 = 0$ since it involves an odd number of derivatives and leads to a non-propagating interaction. Field equations can be derived by varying the Lagrangians in Eqs. (3.3), (3.28), and (3.29) with respect to $e_{i\mu}$, $A_{ij\mu}$, and $S^{\mu\nu i}$. Variation with respect to $S^{\mu\nu i}$ returns the tetrad postulate. Variation with respect to the gauge field reads

$$\begin{aligned}\frac{\delta(e\mathcal{L}_{\text{Total}})}{\delta A_{ij\mu}} = \frac{1}{4}D_\nu\Big(\{c_2F^{\mu\sigma ik}e^{j\nu}e_{k\sigma} + c_3F_{\sigma\alpha mn}e^{i\mu}e^{j\nu}e^{n\alpha}e^{m\sigma} + c_4F^{\alpha\beta mn}e_{m\alpha}e^{j}{}_{\beta}e^{i\mu}e_{n}{}^{\nu} \\ -(i\leftrightarrow j)\} - (\mu\leftrightarrow\nu)\Big) + c_5D_\nu F^{\mu\nu ij} \\ + \frac{\delta\mathcal{L}_M}{\delta A_{ij\mu}} - \frac{1}{2}S^{\mu\nu i}e^{j}{}_{\nu} + \frac{1}{2}S^{\mu\nu j}e^{i}{}_{\nu} = 0. \end{aligned} \tag{3.31}$$

Here $\frac{\delta\mathcal{L}_M}{\delta A_{ij\mu}}$ is the spin angular momentum of matter while the last two terms are of angular momentum type and acceptable only if defined locally. Variation with respect to $e_{i\alpha}$ reads

$$\begin{aligned}\frac{\delta\mathcal{L}_{\text{Total}}}{\delta e_{i\alpha}} = \frac{\delta\mathcal{L}_{\text{Matter}}}{\delta e_{i\alpha}} - D_\beta S^{\beta\alpha i} - \frac{1}{2}c_2F^{\beta\alpha}{}_{j}{}^{i}F_{\beta\lambda}{}^{jk}e_{k}{}^{\lambda} \\ -c_3F^{\mu\lambda mj}F^{\alpha\nu in}e_{m\mu}e_{n\nu}e_{j\lambda} - \frac{1}{2}c_4F^{\alpha\mu ij}F^{\nu\beta mn}e_{m\nu}e_{j\beta}e_{n\mu} \\ -\frac{1}{2}c_4F^{\mu\nu ji}F^{\beta\alpha mn}e_{j\mu}e_{m\beta}e_{n\nu} = 0. \end{aligned} \tag{3.32}$$

Note that we already set $c_1 = 0$ and also $S^{\mu\nu i}$ is a non-propagating field, i.e., is zero outside of matter. The solution to Eq. (3.32), by neglecting the second order terms in F, is

$$S^{\alpha\beta i} = T^{\alpha\beta}\xi^i, \tag{3.33}$$

where $T^{\alpha\beta}$ is the energy momentum tensor and ξ^i is defined as follows

$$\xi^i(x) = \begin{cases} e^{i}{}_{\alpha}(X)(x^\alpha - X^\alpha) & x < \delta, \\ 0 & x \geq \delta, \end{cases} \tag{3.34}$$

where δ is assumed to be very small and X refers to a local point.

3.3.1 Static Spherically Symmetric Case: A Weak Field Approximation

In this part we would like to find a static spherically symmetric solution. An approximate approach is sufficient for our purposes. We start with the following tetrad field:

$$e_{i\mu} = \begin{pmatrix} \sqrt{a(r)} & & & \\ & \sqrt{b(r)} & & \\ & & r & \\ & & & r\sin(\theta) \end{pmatrix}, \tag{3.35}$$

where

$$\begin{aligned} a &= 1 + \delta a, \\ b &= 1 + \delta b, \end{aligned} \tag{3.36}$$

with δa and $\delta b \ll 1$.

Here the results to the first order of perturbation in δa and δb are desired, and therefore for the rest of the section, only the first order terms will be kept. The Christoffel symbols, $\Gamma^{\lambda}_{\mu\nu}$, can be easily calculated using Eq. (3.7)

$$\begin{aligned} \Gamma^1_{00} &= \frac{1}{2}\delta a', & \Gamma^2_{12} &= \frac{1}{r}, & \Gamma^1_{22} &= -r(1-\delta b), \\ \Gamma^0_{01} &= \frac{1}{2}\delta a', & \Gamma^3_{13} &= \frac{1}{r}, & \Gamma^1_{33} &= -r\sin^2(\theta)(1-\delta b), \\ \Gamma^1_{11} &= \frac{1}{2}\delta b', & \Gamma^3_{23} &= \frac{\cos(\theta)}{\sin(\theta)}, & \Gamma^2_{33} &= -\sin(\theta)\cos(\theta), \end{aligned} \tag{3.37}$$

where prime indicates derivative with respect to r. The spin connections, $A_{ij\mu}$, using Eq. (3.8) are

$$\begin{aligned} A_{100} &= \frac{1}{2}\delta a', & A_{122} &= 1 - \frac{1}{2}\delta b, \\ A_{133} &= \left(1 - \frac{1}{2}\delta b\right)\sin(\theta), & A_{233} &= \cos(\theta), \end{aligned} \tag{3.38}$$

and the strength tensor, $F_{\mu\nu ij}$, using Eq. (3.30) reads

$$\begin{aligned} F_{1010} &= -\frac{1}{2}\delta a'', & F_{0220} &= \frac{1}{2}\delta a', & F_{0330} &= \frac{1}{2}\sin(\theta)\delta a', \\ F_{1221} &= -\frac{1}{2}\delta b', & F_{1331} &= -\frac{1}{2}\sin(\theta)\delta b', & F_{3232} &= \sin(\theta)\delta b. \end{aligned} \tag{3.39}$$

Here, and also in the rest of this chapter, only nonzero components are shown. Inserting everything into Eq. (3.31) and neglecting terms of second orders in δa and δb

$$\begin{cases} (c_2+2c_3+c_4+2c_5)\left(r^3\delta a'''+2r^2\delta a''-2r\delta a'\right) \\ \quad -(c_2+4c_3+c_4)\left(r^2\delta b''-2\delta b\right)=2r^3\left(S^{001}e^0{}_0-S^{010}e^1{}_1\right), \\ r^2\delta b''-2\delta b=\dfrac{c_2+4c_3+c_4}{3c_2+8c_3+3c_4+4c_5}\left(r^3\delta a'''+2r^2\delta a''-2r\delta a'\right). \end{cases} \tag{3.40}$$

These two can be used to write down one of the two final equations

$$r^2\delta a'''+2r\delta a''-2\delta a'=2r^2\lambda^{-1}\left(S^{001}e^0{}_0-S^{010}e^1{}_1\right), \tag{3.41}$$

where

$$\lambda=\frac{(c_2+2c_3+c_4+2c_5)(3c_2+8c_3+3c_4+4c_5)-(c_2+4c_3+c_4)^2}{3c_2+8c_3+3c_4+4c_5}, \tag{3.42}$$

and is a constant. The right-hand side of Eq. (3.41) is zero for a vacuum case. Therefore, the most general solution is

$$\delta a'=\frac{\alpha_1}{r^2}+\alpha_2 r. \tag{3.43}$$

This solution should go to zero at large distances, which implies that $\alpha_2=0$. The other constant can be determined by comparing with the Schwarzschild solution

$$\alpha_1=2GM, \tag{3.44}$$

where G is the Newton's gravitational constant and M is the mass of the object at the center. Using Eq. (3.40) and considering that the right-hand side of Eq. (3.41) is zero, the other equation is

$$r^2\delta b''-2\delta b=0, \tag{3.45}$$

with the most general solution

$$\delta b=\frac{\beta_1}{r}+\beta_2 r^2. \tag{3.46}$$

In order to have a proper behavior at infinity, $\beta_2=0$. The other constant is

$$\beta_1=2GM, \tag{3.47}$$

which comes from comparison with the Schwarzschild solution.

3.4 A Special Case

On the one hand, in the standard model of particle physics the field equations are of the following form:

$$D_\mu F^{\mu\nu} = J^\nu, \tag{3.48}$$

where F, the field strength, has no direct contribution to the source, J, i.e., $J \neq J(F)$. On the other hand, it is strongly desired to make our gravitational theory as close to the standard model as possible. That means the source of our theory should not depend on the strength tensor. In the theory presented above, the source can be read from Eq. (3.31) as

$$J^{\mu ij} = \frac{\delta \mathcal{L}_M}{\delta A_{ji\mu}} + S^{\mu\nu[i} e^{j]}_{\ \ \nu}, \tag{3.49}$$

where anti-symmetrization is denoted by a pair of square brackets and $S^{\mu\nu j}$ is determined through Eq. (3.32), from which it can be deduced that by setting c_1 through c_4 to zero, the direct contribution of the strength field to the source can be eliminated. Therefore, we are left with one single term in the gauge field Lagrangian, Eq. (3.29), which defines the special case

$$\mathcal{L}_A = -\frac{1}{4} c_5 F_{\mu\nu ij} F^{\mu\nu ij}. \tag{3.50}$$

The field equations now read

$$\begin{aligned} \frac{\delta \mathcal{L}_{\text{Matter}}}{\delta e_{i\alpha}} - D_\beta S^{\beta\alpha i} &= 0, \\ c_5 D_\nu F^{\mu\nu ij} &= J^{\mu ij}, \end{aligned} \tag{3.51}$$

with J given by Eq. (3.49). The first equation implies the exact solution, $S^{\mu\nu i} = T^{\mu\nu}\xi^i$, which can be used to eliminate $S^{\mu\nu i}$ in the source term and reduce the whole set to

$$\begin{aligned} c_5 D^\nu F_{\mu\nu ij} &= J_{\mu ij} \\ &= \frac{\delta \mathcal{L}_M}{\delta A^{ji\mu}} + \frac{1}{2} T_{\mu j}\xi_i - \frac{1}{2} T_{\mu i}\xi_j. \end{aligned} \tag{3.52}$$

3.4.1 Static Spherically Symmetric Case: An Exact Solution

For any proposed theory of gravity, it is crucial to address the experimental tests that general relativity has already passed and most of these experiments are performed within the solar system which is a static spherically symmetric case and this

makes the subject specifically important. See [16] for a thorough review of the subject. The Schwarzschild metric, the solution to a static spherically symmetric space in GR, has explained all the relevant experiments and, consequently, should be the solution of any theory of gravity at least to some higher than one orders of perturbation since the first order is not sufficient to explain all the existing observations. Fortunately it is not hard to show that this metric is an exact solution to the special case we have presented in this section. We start with the following tetrad:

$$e_{i\mu} = \begin{pmatrix} \sqrt{a(r)} & & & \\ & \frac{1}{\sqrt{a(r)}} & & \\ & & r & \\ & & & r\sin(\theta) \end{pmatrix}. \tag{3.53}$$

The Christoffel symbols, $\Gamma^{\lambda}_{\mu\nu}$, are

$$\begin{aligned} \Gamma^1_{00} &= \frac{1}{2}aa', & \Gamma^2_{12} &= \frac{1}{r}, & \Gamma^1_{22} &= -ra, \\ \Gamma^0_{01} &= \frac{1}{2}\frac{a'}{a}, & \Gamma^3_{13} &= \frac{1}{r}, & \Gamma^1_{33} &= -r\sin^2(\theta)a, \\ \Gamma^1_{11} &= -\frac{1}{2}\frac{a'}{a}, & \Gamma^3_{23} &= \frac{\cos(\theta)}{\sin(\theta)}, & \Gamma^2_{33} &= -\sin(\theta)\cos(\theta), \end{aligned} \tag{3.54}$$

where prime indicates derivative with respect to r. The spin connections, $A_{ij\mu}$, are

$$\begin{aligned} A_{100} &= \frac{1}{2}a', & A_{122} &= \sqrt{a}, \\ A_{133} &= \sqrt{a}\sin(\theta), & A_{233} &= \cos(\theta), \end{aligned} \tag{3.55}$$

and the strength tensor, $F_{\mu\nu ij}$, is

$$\begin{aligned} F_{1010} &= -\frac{1}{2}a'', & F_{0220} &= \frac{1}{2}\sqrt{a}a', & F_{0330} &= \frac{1}{2}\sqrt{a}\sin(\theta)a', \\ F_{1221} &= \frac{1}{2}\frac{a'}{\sqrt{a}}, & F_{1331} &= \frac{1}{2}\sin(\theta)\frac{a'}{\sqrt{a}}, & F_{3232} &= \sin(\theta)(1-a). \end{aligned} \tag{3.56}$$

Substituting everything into Eq. (3.52) and assuming a vacuum case result in two equations

$$\begin{aligned} a''' + \frac{2}{r}a'' - \frac{2}{r^2}a' &= 0, \\ a'' - \frac{2}{r^2}a + \frac{2}{r^2} &= 0. \end{aligned} \tag{3.57}$$

It is now easy to show that

$$a(r) = 1 - \frac{2GM}{r}, \tag{3.58}$$

satisfies both of the equations, i.e., the Schwarzchild metric is an exact solution of this special case of the theory.

3.4.2 Homogeneous Isotropic Case: A Cosmological Solution

Another important subject that any theory of gravity should somehow address is a homogeneous and isotropic space described by the Friedmann–Lemaître–Robertson–Walker metric, or equivalently, the following tetrad:

$$e_{i\mu} = a(t) \begin{pmatrix} a(t)^{-1} & & & \\ & 1 & & \\ & & r & \\ & & & r\sin(\theta) \end{pmatrix}. \tag{3.59}$$

The Christoffel symbols, $\Gamma^{\lambda}_{\mu\nu}$, are

$$\begin{aligned}
&\Gamma^1_{01} = \frac{\dot{a}}{a}, && \Gamma^2_{02} = \frac{\dot{a}}{a}, && \Gamma^3_{03} = \frac{\dot{a}}{a},\\
&\Gamma^0_{11} = a\dot{a}, && \Gamma^2_{12} = \frac{1}{r}, && \Gamma^3_{13} = \frac{1}{r},\\
&\Gamma^0_{22} = r^2 a\dot{a}, && \Gamma^1_{22} = -r, && \Gamma^3_{23} = \frac{\cos(\theta)}{\sin(\theta)},\\
&\Gamma^0_{33} = r^2\sin^2(\theta)a\dot{a}, && \Gamma^1_{33} = -r\sin^2(\theta), && \Gamma^2_{33} = -\cos(\theta)\sin(\theta),
\end{aligned} \tag{3.60}$$

where dot indicates derivative with respect to time. The spin connections, $A_{ij\mu}$, are

$$\begin{aligned}
&A_{101} = \dot{a}, && A_{022} = -r\dot{a}, && A_{033} = -r\sin(\theta)\dot{a},\\
&A_{122} = 1, && A_{233} = \cos(\theta), && A_{133} = \sin(\theta),
\end{aligned} \tag{3.61}$$

and the strength tensor, $F_{\mu\nu ij}$, is

$$\begin{aligned}
&F_{1010} = \ddot{a}, && F_{0220} = -r\ddot{a}, && F_{0330} = -r\sin(\theta)\ddot{a},\\
&F_{1221} = -r\dot{a}^2, && F_{1331} = -r\sin(\theta)\dot{a}^2, && F_{3232} = r^2\sin(\theta)\dot{a}^2.
\end{aligned} \tag{3.62}$$

The experimental data were gathered in 1998 when two independent groups of cosmologists observed that the universe is expanding with a positive rate. Within the context of general relativity this observation is commonly explained by introducing the cosmological constant, an unknown form of energy with negative pressure. Here in this chapter we would like to show that without the help of the cosmological constant, our theory is able to explain the observation. The problem will be dramatically simpler for a vacuum case where no matter exist at all. Indeed this is not an irrelevant assumption to make as the matter density in the current epoch of the universe is almost negligible. Substituting all the pieces into Eq. (3.52) and assuming $J^{\mu ij} = 0$ result in one single equation

$$\dddot{a} + \frac{\dot{a}}{a}\ddot{a} - 2\left(\frac{\dot{a}}{a}\right)^2 \dot{a} = 0. \tag{3.63}$$

It turns out that the solution to this equation is

$$a(t) = e^{Ht}, \tag{3.64}$$

where $H = \frac{\dot{a}}{a}$ is a constant. This is exactly the de Sitter space which also can be achieved in general relativity. The only difference is that in general relativity the cosmological constant is needed to achieve this solution while in the present theory the solution holds for a vacuum case.

3.4.3 *Feynman Rules and Renormalizability of the Lorentz Gauge Theory of Gravity*

Here we start from Eq. (3.52) where

$$\begin{aligned} T_{\mu i} &= e_{j\mu} e_{i\alpha} \frac{\delta \mathcal{L}_M}{\delta e_{j\alpha}} = e_{j\mu} e_{i\alpha} i\bar{\psi}\gamma^j g^{\alpha\beta} \left\{ \partial_\beta \psi - \frac{1}{2} S^{mn} A_{mn\beta} \psi \right\}, \\ \frac{\delta \mathcal{L}_M}{\delta A^{ij\mu}} &= -\frac{i}{2} e_{m\mu} \bar{\psi}\gamma^m S_{ij}\psi. \end{aligned} \tag{3.65}$$

To further simplify the calculations, a flat background will be chosen. This in turn means $e_{i\mu} = \delta_{i\mu}$, $g_{\mu\nu} = \eta_{\mu\nu}$ and $\Gamma^\gamma_{\mu\nu} = 0$. Since the constraint in Eq. (3.28) has been taken care of in Eq. (3.52), we choose to quantize using this field equation. This is despite the fact that the path integral approach is proven to be very strong method when working with gauge theories. In our approach one needs to take care of the gauge freedom because otherwise the inverse of the propagator would be singular and also unitarity may be violated. Therefore, the Lorentz gauge will be adopted in the following:

$$\partial^{\nu} A_{ij\nu} = 0, \tag{3.66}$$

which, together with Eq. (3.52), leads to the following field equations:

$$\partial^2 A_{ij\mu} = c_5^{-1}\left(-\frac{\delta \mathcal{L}_M}{\delta A^{ij\mu}} + \frac{1}{2} T_{\mu j}\xi_i - \frac{1}{2} T_{\mu i}\xi_j \right) - F(A)_{ij\mu}, \tag{3.67}$$

where

$$\begin{aligned} F(A)_{ij\mu} = {} & (\eta_i^a \eta_j^b - \eta_j^a \eta_i^b)\Big(2\eta^{mn}\eta^{\alpha\beta}\eta_{\mu}^{\gamma} - \eta^{\alpha\gamma}\eta^{mn}\eta_{\mu}^{\beta}\Big) A_{mb\alpha}\partial_{\beta} A_{an\gamma} \\ & + \eta^{\alpha\gamma}\eta_{\mu}^{\beta}\Big(2\eta_j^m \eta^{bs}\eta_i^a \eta^{nr} + \eta^{mn}\eta_i^b \eta^{ar}\eta_j^s - \eta^{mn}\eta_j^b \eta^{ar}\eta_i^s\Big) A_{mb\alpha} A_{an\gamma} A_{rs\beta}. \end{aligned} \tag{3.68}$$

It is now necessary to find the propagator of the gauge field, $D_{ij\mu,mn\nu}(y-x)$. It should be antisymmetric in the consecutive Lorentz indices because the gauge field also has the same property. Moreover, it should satisfy the following:

$$\begin{aligned} D_{ij\mu,mn\nu}(y-x) &= D_{mn\nu,ij\mu}(y-x), \\ A_{mn\nu}(x) &= -\int d^4 y\, A^{ij\mu}(y)\partial^2 D_{ij\mu,mn\nu}(y-x). \end{aligned} \tag{3.69}$$

Therefore the propagator has the form

$$D_{ij\mu,mn\nu}(x-y) = \frac{1}{2}\eta_{\mu\nu}\Big(\eta_{mi}\eta_{nj} - \eta_{mj}\eta_{ni}\Big) D(x-y), \tag{3.70}$$

with $D(x-y)$ satisfying

$$\partial^2 D(x-y) = -\delta^4(x-y), \tag{3.71}$$

where the solution is

$$D(x-y) = \int \frac{d^4 q}{(4\pi)^4} \frac{e^{-iq\cdot(x-y)}}{q^2 + i\varepsilon}. \tag{3.72}$$

In the field of particle physics we are usually interested in scattering problems. A particle in the distant past is moving toward the scattering area and is described by a plane wave, $\epsilon_{ij\mu} e^{-ik_i \cdot x}$, at the beginning. We would like to know the final state in the far future. This information is stored in the transition amplitudes known as the S matrix

$$S_{fi} = \lim_{t\to\infty} \left\langle A_{\text{final}}(\vec{x}, t) | A_{\text{initial}}(\vec{x}, t) \right\rangle. \tag{3.73}$$

Here A_{final} can be replaced by a plane wave, $\epsilon_{ij\mu}e^{-ik_f\cdot x}$, when time goes to infinity. On the other hand, A_{initial} is a plane wave only in the distant past, $\epsilon_{ij\mu}e^{-ik_i\cdot x}$, and develops to a somewhat more complicated in the future

$$A_{ij\mu}(x) = \epsilon_{ij\mu}e^{-ik_i\cdot x} + \int d^4y\, D_{ij\mu,mn\nu}(x-y) \times\left(c_5^{-1}\left(\frac{\delta\mathcal{L}_M}{\delta A_{mn\nu}} - \frac{1}{2}T^{\nu n}\xi^m + \frac{1}{2}T^{\nu m}\xi^n\right) + F(A)^{mn\nu}\right), \tag{3.74}$$

where the Green's function method is used. This is itself an integral equation, but if the interactions are weak enough, we can solve it perturbatively and keep as many terms as needed. Equations (3.73) and (3.74) can be used to derive any possible interaction to any desired order. Deriving all the possible interactions is out of the scope of the current work. We are instead interested in finding all the Feynman rules of the theory. These are the vertices and the propagator with which all the other interactions can be built and are also sufficient to investigate the renormalizability of the theory. The propagator is already derived and in the momentum space reads

$$= \frac{1}{2}\frac{\eta_{\mu\nu}\left(\eta_{mi}\eta_{nj} - \eta_{mj}\eta_{ni}\right)}{q^2 + i\varepsilon}. \tag{3.75}$$

The self interactions are cyphered in $F(A)^{mn\nu}$. These are

$$= iq_\beta(\eta_i^a\eta_j^b - \eta_j^a\eta_i^b)\left(2\eta^{mn}\eta^{\alpha\beta}\eta_\mu^\gamma - \eta^{\alpha\gamma}\eta^{mn}\eta_\mu^\beta\right),$$

$$= \eta^{\alpha\gamma}\eta_\mu^\beta\left(2\eta_j^m\eta^{bs}\eta_i^a\eta^{nr} + \eta^{mn}\eta_i^b\eta^{ar}\eta_j^s - \eta^{mn}\eta_j^b\eta^{ar}\eta_i^s\right). \tag{3.76}$$

Since all the spin connections that appear here have the same ranking, a permutation over them is in order. However, extra care should be taken when field equations are used for the sake of quantization. One of the fields, with indices (i, j, μ), is already distributed over all the legs of the diagrams. Therefore, only the remaining fields need to be permuted. There are also two types of interactions with matter.

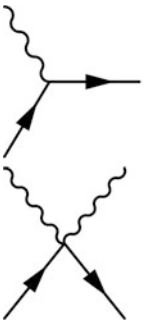

$$= \frac{1}{2}c_5^{-1}\left(q_\alpha \delta^{j\nu}\delta^{n\alpha}\gamma_j\xi^m - q_\alpha \delta^{j\nu}\delta^{m\alpha}\gamma_j\xi^n - i\delta^{k\nu}\gamma_k S^{mn}\right),$$

$$= \frac{i}{4}c_5^{-1}\left(\delta^{j\nu}\delta^{n\beta}\gamma_j S^{kl}\xi^m - \delta^{j\nu}\delta^{m\beta}\gamma_j S^{kl}\xi^n\right). \tag{3.77}$$

In order to preserve the gauge invariance in the presence of Feynman diagrams with loops, Faddeev–Popov ghost fields must be introduced and utilized as well. At this point we can start our investigation into the renormalizability of the theory. A detailed study of the subject is out of the scope of the present chapter. We instead use the simple method of power-counting which only gives an idea about the divergences and cannot be used as an alternative to an exact proof. A good description of the subject is given in [17]. In a given Feynman diagram of any order, there exist L number of loops, I number of internal lines, E number of external lines, and V number of vertices. The superficial degree of divergence in four dimensions reads

$$D = 4L + \sum_i v_i(d_i - w_i) - I_f - 2I_A. \tag{3.78}$$

Here summation is over the four vertices given by Eqs. (3.76) and (3.77), and v_i is the number of such vertices in the diagram while d_i is the number of derivatives in the ith vertex. Also, w_i is zero for the vertices which contain no ξ, namely Eq. (3.76), otherwise it is the momentum dependence, if any, of ξ, i.e., $\xi \propto q^{-w}$. The source of this momentum dependence is not known at this point. One naive way to achieve it is to assume δ in Eq. (3.34) is energy dependent. The subscripts f and A indicate fermionic field and the gauge field, respectively. It is now required to express the superficial degree of divergence in terms of the number of external lines and vertices. Here the following identities prove useful:

$$\begin{aligned} 1 &= L + V - I, \\ E_{(A/f)} &= \sum_i n^{(i)}_{(A/f)} v_i - 2I_{(A/f)}, \\ I &= I_f + I_A, \\ V &= \sum_i v_i, \end{aligned} \tag{3.79}$$

where $n^{(i)}_{(A/f)}$ refers to the number of gauge or fermionic fields at the vertex labeled by i. Gathering all the pieces, the superficial degree of divergence can be rewritten as

$$\begin{aligned} D &= 4\left(1-\sum_i v_i + I_f + I_A\right) + \sum_i v_i(d_i - w_i) - I_f - 2I_A \\ &= 4 + 3I_f + 2I_A - \sum_i v_i(4 + w_i - d_i) \\ &= 4 + \frac{3}{2}\left(\sum_i v_i n_f^{(i)} - E_f\right) + \frac{2}{2}\left(\sum_i v_i n_A^{(i)} - E_A\right) - \sum_i v_i(4 + w_i - d_i) \\ &= 4 - E_A - \frac{3}{2}E_f - \sum_i v_i\left(4 - n_A^i - \frac{3}{2}n_f^i + w_i - d_i\right). \end{aligned} \tag{3.80}$$

In principle we can have a graph with as many number of vertices as needed. In a renormalizable theory, the superficial degree of divergence does not increase with the order in the perturbation theory. This increase does not happen in our case only if at any given vertex

$$4 - n_A^i - \frac{3}{2}n_f^i + w_i - d_i \geqslant 0. \tag{3.81}$$

This factor is zero for both of the vertices in Eq. (3.76) since (n_A, n_f, w, d) is (3, 0, 0, 1) in the first vertex and (4, 0, 0, 0) in the second one. On the other hand, we have (1, 2, w, 1) for the first two terms in the first vertex in Eq. (3.77) and (1, 2, 0, 0) for the last term and (2, 2, w, 0) for the second vertex. Hence, Eq. (3.81) holds for the vertices in Eq. (3.77) only if $w_i \geqslant 1$. As mentioned above, this can be achieved if $\delta \propto \frac{1}{q^w}$ in Eq. (3.34). Investigation of methods by which this momentum behavior can be reached is beyond the scope of this work and is left for future studies. Although the renormalizability of the theory has not been proved, under this condition, the power-counting method suggests a good high energy behavior for the theory.

3.5 Conclusions

In this chapter we have presented a Lorentz gauge formulation of gravity in which the metric has no dynamics. To achieve this, we have used the equivalence principle that assures the existence of a free falling frame whose coordinate system is locally Minkowskian. Therefore, at any point in space-time there always exists a frame which is both of coordinate and Lorentz types. This leads to the fact that a tetrad field can be split into two parts, namely, $e_{i\mu} = \eta^{\bar{k}\bar{l}} e_{i\bar{k}} e_{\bar{l}\mu}$, where the free falling frame has been indicated with a bar. A variation in the tetrad field can therefore stem from any of the two constituents. One leads to the Einstein's theory of gravity while

the other to a formulation with no dynamics for metric. Because of the spectacular success of the standard model of particle physics both in terms of experiments and renormalizability, we have investigated the formulation that is more analogous to the standard model, the latter case, within which we have shown that a variation of the action with respect to the tetrad results in the trivial angular momentum conservation equation where there exists no source for the resulting field equations. Consequently, the field equations have been derived by varying the action with respect to the spin connections where the Lagrange multiplier method has been used to impose the tetrad postulate and eliminate the tetrad as a function of the spin connection.

A spherically symmetric weak field solution was also investigated and it was shown that to the first order of perturbation, it is in agreement with the Schwarzschild solution. A special case of the theory is also presented where the Schwarzschild metric is an exact solution. Moreover, a homogeneous and isotropic space has also been studied within this special case. It was shown that there exists a natural exponentially expanding vacuum solution where cosmological constant or any other type of dark energy is absent. In addition, quantization of the theory has been studied briefly and all the basic Feynman diagrams have been derived. The theory was also shown to be power-counting renormalizable if a certain condition is met.

References

1. S. Weinberg, Ultraviolet divergences in quantum theories of gravitation, in *General Relativity. An Einstein Centenary Survey*, ed. by S.W. Hawking, W. Israel (Cambridge University Press, Cambridge, 1980)
2. J.M. Maldacena, Adv. Theor. Math. Phys. **2**, 231 (1998) [arXiv:hep-th/9711200]
3. S.S. Gubser, I.R. Klebanov, A.M. Polyakov, Phys. Lett. B **428**, 105 (1998) [arXiv:hep-th/9802109]
4. E. Witten, Adv. Theor. Math. Phys. **2**, 253 (1998) [arXiv:hep-th/9802150]
5. A. Borzou, Class. Quantum Grav. **33**, 025008 (2016) [arXiv:1412.1199]
6. R. Utiyama, Phys. Rev. **101**, 1597 (1956)
7. T.W.B. Kibble, J. Math. Phys. **2**, 212 (1961)
8. D.W. Sciama, Rev. Mod. Phys. **36**, 463 (1964)
9. F.W. Hehl, J.D. McCrea, E.W. Mielke, Y. Neeman, Phys. Rep. **258**, 1 (1995)
10. D. Ivanenko, G. Sardanashvily, Phys. Rep. **94**, 1 (1983)
11. S. Weinberg, *Gravitation and Cosmology: Principles and Applications of the General Theory of Relativity* (Wiley, New York, 1972)
12. S.M. Carroll, *An Introduction To General Relativity: Spacetime and Geometry* (Benjamin Cummings, San Francisco, 2003)
13. F. De Felice, C.J.S. Clarke, *Relativity on Curved Manifolds* (Cambridge University Press, Cambridge, 1990)
14. K. Hayashi, T. Shirafuji, Prog. Theor. Phys. **64**, 866 (1980)
15. V.P. Nair, S. Randjbar-Daemi, V. Rubakov, Phys. Rev. D **80**, 104031 (2009) [arXiv:hep-th/0811.3781]
16. C.M. Will, Living Rev. Relativ. **9**, 3 (2006) [arXiv:gr-qc/0510072]
17. S. Weinberg, *The Quantum Theory of Fields* (Cambridge University Press, Cambridge, 1995)

Chapter 4
Standard Model and Supersymmetry

4.1 Review of the Standard Model

The standard model is a gauge theory of SU(3) × SU(2) × U(1) with twelve vector fields, forty-five fermion fields, and a doublet of complex scalar fields. It describes the strong, weak, and electromagnetic interactions and, with only a few exceptions, the behavior of all observed particles. All the particles described by the standard model are summarized in Fig. 4.1. The SU(2) × U(1) gauge is responsible for explaining the electroweak interactions of the standard model. Here, there is a left and right asymmetry in the sense that only left-handed fields go into the isodoublets of the SU(2) group, Ψ_L, while the right-handed fields are all isosinglets of the SU(2) group, ψ_R. In the leptonic case the doublets are shown as

$$P_L \begin{bmatrix} \psi_{\nu_l} \\ \psi_l \end{bmatrix}, \tag{4.1}$$

where "l" refers to the three lepton flavors, namely, the electron, muon, and tau. Also, P_L is the left-handed projection operator defined as

$$P_L = \frac{1 - \gamma^5}{2}. \tag{4.2}$$

The right-handed projection operator is defined similarly as

$$P_R = \frac{1 + \gamma^5}{2}. \tag{4.3}$$

On the other hand, in the case of quarks, the doublets are made of the six different quark flavors in the following way:

A. Borzou, *Theoretical and Experimental Approaches to Dark Energy and the Cosmological Constant Problem*, Springer Theses,
https://doi.org/10.1007/978-3-319-69632-4_4

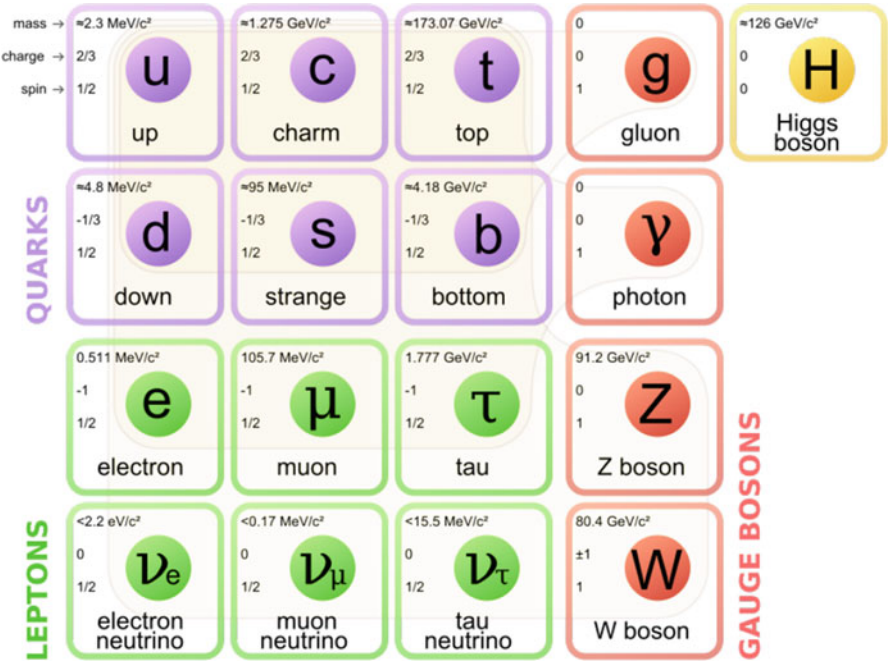

Fig. 4.1 Table of particles in the standard model

$$P_L \left\{ \begin{bmatrix} \text{up} \\ \text{down} \end{bmatrix}, \begin{bmatrix} \text{charm} \\ \text{strange} \end{bmatrix}, \begin{bmatrix} \text{top} \\ \text{bottom} \end{bmatrix} \right\} . \tag{4.4}$$

The Lagrangian of this theory is invariant under the following transformations

$$\begin{aligned} \Psi_L \to \Psi_L' &= \exp\left(\frac{i}{2} g \omega^i(x) \tau_i + \frac{i}{2} g' Y_L^{\text{doublet}} f(x)\right) \Psi_L, \\ \psi_R^{\text{up}} \to \psi_R^{\text{up}'} &= \exp\left(\frac{i}{2} g' Y_R^{\text{up}} f(x)\right) \psi_R^{\text{up}}, \\ \psi_R^{\text{down}} \to \psi_R^{\text{down}'} &= \exp\left(\frac{i}{2} g' Y_R^{\text{down}} f(x)\right) \psi_R^{\text{down}}, \end{aligned} \tag{4.5}$$

where τ_i are the three Pauli matrices, g and g' are coupling constants, and $\omega^i(x)$ and $f(x)$ are arbitrary functions. The labels "up" and "down" in the isosinglets refer to neutrinos and their corresponding leptons, respectively, in the leptonic case or up- and down-type quarks in the quark case. Moreover, the hypercharges are

	Y_L^{doublet}	Y_R^{up}	Y_R^{down}
Leptons	-1	0	-2
Quarks	$\frac{1}{3}$	$\frac{4}{3}$	$-\frac{2}{3}$

To ensure this invariance, one needs to introduce the covariant derivative

$$D_\mu = \partial_\mu + \frac{i}{2} g \Gamma \vec{\tau} \cdot \vec{W}_\mu + \frac{i}{2} g' Y B_\mu \tag{4.6}$$

where Γ is 0 or 1 for singlets or doublets, respectively, and Y refers to one of the three hypercharges given in the table above. Here, the $\vec{W}_\mu$ are the three SU(2) gauge fields and B_μ is the U(1) gauge field—a combination of which gives the famous W and Z vector bosons as well as the photon vector field. The two W bosons are described by

$$\begin{aligned} W_\mu &= \frac{1}{\sqrt{2}} \left(W_\mu^1 - i W_\mu^2 \right), \\ W_\mu^\dagger &= \frac{1}{\sqrt{2}} \left(W_\mu^1 + i W_\mu^2 \right), \end{aligned} \tag{4.7}$$

while the Z bosons and photons, A_μ, are given by

$$\begin{aligned} Z_\mu &= \cos\theta_W W_\mu^3 - \sin\theta_W B_\mu, \\ A_\mu &= \sin\theta_W W_\mu^3 + \cos\theta_W B_\mu. \end{aligned} \tag{4.8}$$

Here, θ_W is the weak mixing angle or Weinberg angle.

The SU(3) gauge explains the strong force. Quarks are introduced with a triplet of fermionic fields

$$\Psi = \begin{bmatrix} \psi_1 \\ \psi_2 \\ \psi_3 \end{bmatrix}, \tag{4.9}$$

where the subscripts 1, 2, and 3 represent three different colors. The idea is that the Lagrangian describing the strong interactions should remain invariant under a transformation of the following type:

$$\Psi \to \Psi' = \exp\left(\frac{i}{2} g \alpha^a(x) \lambda_a \right) \Psi, \tag{4.10}$$

where α^a is any arbitrary function of location and λ_a are the eight SU(3) matrices. This can be achieved by replacing the partial derivative with a covariant derivative defined as

$$\partial_\mu \to D_\mu = \partial_\mu - ig\vec{A}_\mu, \tag{4.11}$$

where $\vec{A}_\mu$ are the gluon fields that locally preserve this symmetry and are formed using the Gell-Mann SU(3) matrices as $\vec{A}_\mu = A^a_\mu \lambda_a$, where a runs from 1 to 8. So far, six different flavors of quarks have been observed. These are the up, down, charm, strange, top, and bottom. Therefore, $3 \times 6 = 18$ different fermionic plus 8 different bosonic fields are introduced to explain the strong interactions.

4.2 Supersymmetry as an Extension of the Standard Model

We present a brief review of supersymmetry in this section, where Refs. [1–3] are extensively used. In the standard model, fields satisfy the Poincare symmetry, i.e., they are invariant under the following transformation

$$x^\mu \to x'^\mu = \Lambda^\mu_{\ \nu} x^\nu + a^\mu \tag{4.12}$$

where $\Lambda^\mu_{\ \nu} = e^{i(M^{ij})_{\mu\nu}\omega_{ij}}$ is a Lorentz transformation, $a^\mu = e^{iP_\mu b^\mu}$ is a translation transformation, and ω_{ij} and b^μ are arbitrary parameters. $M_{\mu\nu}$ and P_μ are the generators of the Poincare group and satisfy the Poincare algebra:

$$\begin{aligned}
[P^\mu, P^\nu] &= 0, \\
[M^{\mu\nu}, P^\rho] &= i(g^{\nu\rho}P^\mu - g^{\mu\rho}P^\nu), \\
[M^{\mu\nu}, M^{\rho\sigma}] &= i(g^{\nu\rho}M^{\mu\sigma} + g^{\mu\sigma}M^{\nu\rho} - g^{\nu\sigma}M^{\mu\rho} - g^{\mu\rho}M^{\nu\sigma}),
\end{aligned} \tag{4.13}$$

where commutation is represented by [ ]. In 1967, Coleman and Mandula [4] proved a no-go theorem stating that space-time and internal symmetries cannot be combined in any but a trivial way. This means that general relativity is a Poincare gauge theory that can never be unified with the standard model in a nontrivial way. However, in proving this, they had assumed that every new theory will respect the Poincare algebra. Later, Golfand, Likhtman, Haag, Lopuszanski, Sohnius, and others [4–6] showed that there is a way around the no-go theorem, which is to build a theory upon the superalgebra instead of the Poincare algebra. Unlike the Poincare algebra, in which only commutators of the generators are allowed, in superalgebras anti-commutators are also introduced. The simplest superalgebra is the one with a single set of supercharges, the generators of the superalgebra that are two-component Weyl spinors Q_a. Therefore the superalgebra is defined as follows:

$$\begin{aligned}
\{Q_a, Q^\dagger_{\dot{a}}\} &= 2(\sigma^\mu)_{a\dot{a}}P_\mu, \\
\{Q_a, Q_b\} &= \{Q^\dagger_{\dot{a}}, Q^\dagger_{\dot{b}}\} = 0,
\end{aligned}$$

$$
\begin{aligned}
[Q_a, P^\mu] &= [Q_{\dot{a}}^\dagger, P^\mu] = 0, \\
[Q_a, M^{\mu\nu}] &= \frac{1}{2}(\sigma^{\mu\nu})_a{}^b Q_b, \\
\left[Q_{\dot{a}}^\dagger, M^{\mu\nu}\right] &= \frac{1}{2}(\bar{\sigma}^{\mu\nu})_{\dot{a}}{}^{\dot{b}} Q_{\dot{b}}^\dagger,
\end{aligned} \tag{4.14}
$$

where anti-commutation is represented by $\{\}$. $Q_{\dot{a}}^\dagger \equiv (Q_a)^\dagger$ is the Hermitian conjugate of Q_a, which exists in an independent space with respect to Q_a, and

$$
\begin{aligned}
\sigma^\mu &= (1, \sigma^i), \\
\bar{\sigma}^\mu &= (1, -\sigma^i), \\
\sigma^{\mu\nu} &= \frac{i}{2}(\sigma^\mu \bar{\sigma}^\nu - \sigma^\nu \bar{\sigma}^\mu), \\
\bar{\sigma}^{\mu\nu} &= \frac{i}{2}(\bar{\sigma}^\mu \sigma^\nu - \bar{\sigma}^\nu \sigma^\mu),
\end{aligned} \tag{4.15}
$$

where σ^i are the three Pauli matrices.

To see why fermions and bosons can transform to each other under the superalgebra, we can start with Eq. (4.14):

$$
[Q_1, M^{12}] = \frac{1}{2}(\sigma^3)_1{}^b Q_b = \frac{1}{2} Q_1. \tag{4.16}
$$

Let us assume there is a particle with mass m and spin s along the z axis:

$$
M^{12}|m, s\rangle = s|m, s\rangle. \tag{4.17}
$$

Now we can claim that $|m, s'\rangle \equiv Q_1|m, s\rangle$ is a particle with spin $s' = s - \frac{1}{2}$. To see this, all we need to do is to apply the z component of the angular momentum operator, M^{12}, to this new particle's ket state

$$
\begin{aligned}
M^{12}|m, s'\rangle &= M^{12} Q_1 |m, s\rangle \\
&= \left(Q_1 M^{12} - \frac{1}{2} Q_1\right) |m, s\rangle \\
&= \left(s - \frac{1}{2}\right) Q_1 |m, s\rangle \\
&= \left(s - \frac{1}{2}\right) |m, s'\rangle.
\end{aligned} \tag{4.18}
$$

Therefore $|m, s'\rangle$ is just an eigenstate of M^{12} with an eigenvalue equal to $s - \frac{1}{2}$. Also, it can be shown in the same way that there are eigenstates—particles—with

spin equal to $s + \frac{1}{2}$. On the other hand, the superpartners $|m, s\rangle$ and $Q_1|m, s\rangle$ have exactly the same mass. This can be seen by noting that the momentum operator, P^μ, commutes with the generators of supersymmetry, $[P^\mu, Q_a] = 0$, and also $P_\mu P^\mu |m, s\rangle = m^2 |m, s\rangle$. Hence,

$$\begin{aligned} P_\mu P^\mu |m, s'\rangle &= P_\mu P^\mu Q_a |m, s\rangle \\ &= m^2 Q_a |m, s\rangle \\ &= m^2 |m, s'\rangle, \end{aligned} \tag{4.19}$$

which means that the eigenstate $|m, s'\rangle$ has a mass equal to the eigenstate $|m, s\rangle$. All superpartners have identical gauge quantum numbers since Q_a and its Hermitian conjugate commute with gauge transformations. The fact that the superparticles have not been observed yet suggests that only a severely broken supersymmetry is consistent with current experimental data.

In supersymmetry, single particles are given by supermultiplets that are irreducible presentations of the superalgebra and contain both fermions and bosons. A multiplet with one Weyl fermion field and one scalar field is called a chiral multiplet. Each of the known fermionic particles as well as the Higgs boson are contained in one chiral multiplet. The known vector bosons like the W and Z, photons, and gluons each are grouped with a Weyl fermion to form a vector multiplet. Gravity resides in a multiplet of a third type that contains a graviton and a spin-$\frac{3}{2}$ fermion. A list of superparticles is shown in Fig. 4.2. In addition, it is natural to assume that there is a conserved quantum number in supersymmetry due to which there exists a light stable particle (LSP). The currently well-motivated conserved quantum number is called R-parity and belongs to Z_2 symmetry. All the standard model particles have an R-parity equal to $+1$ while superparticles have R parity equal to -1. This means that if R-parity is conserved there must exist a superparticle in the decay products of another superparticle. Therefore, the LSP remains stable and makes a good candidate for the long sought dark matter particles.

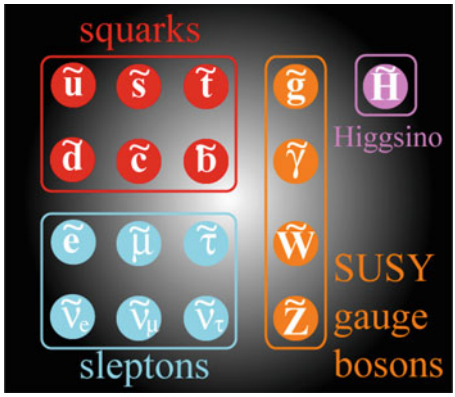

Fig. 4.2 Table of superparticles in supersymmetry

In the search presented in this dissertation, the lightest neutralino $\tilde{\chi}_1^0$, which is a mixture of the bino, wino, and Higgsino, the superpartners of electroweak bosons, is assumed to serve as the LSP. Since neutralinos interact very weakly, just like neutrinos, they cannot be detected by our current CMS detector, neither can they be detected by ATLAS. As a consequence, after their creation, if they are created, they leave the detector with no sign and appear as missing energy in the analysis.

Although in this dissertation the emphasis is put on the cosmological implications of supersymmetry, there are other motivations that make supersymmetry an exciting area. One of the important consequences of supersymmetry is its potential solution to the so-called hierarchy problem in the standard model. In the standard model, particles get their masses through the Higgs mechanism. Here, the Higgs field is introduced with the following potential:

$$V = \mu^2 \Phi^\dagger \Phi + \lambda (\Phi^\dagger \Phi)^2, \tag{4.20}$$

where $\mu^2 < 0$, which has a minimum at a Φ different from zero. This means that the vacuum expectation of the Higgs field is not zero:

$$\Phi_0 = \begin{bmatrix} 0 \\ \frac{v}{\sqrt{2}} \end{bmatrix}, \tag{4.21}$$

where $v = \sqrt{\frac{-\mu^2}{2\lambda}} \simeq 246\,\text{GeV}$, and therefore the Higgs mass $m_H = \sqrt{-2\mu^2} \simeq 125\,\text{GeV}$. The problem starts when one tries to calculate the quantum loop corrections to μ^2. It is shown that the correction is quadratically divergent with a huge cut-off value. This correction can be cancelled, within the standard model's framework, by tuning the value of the bare parameter $-\mu^2$; however, this is something very unlikely and we believe that the full standard model picture should break down at high energies.

This problem can be naturally solved in supersymmetry. The correction from a fermion like top quark is given by

$$-\frac{|\lambda_f|^2}{8\pi^2}\Lambda^2, \tag{4.22}$$

while the correction from a scalar field, like a superpartner, is

$$\frac{\lambda_s}{16\pi^2}\Lambda^2, \tag{4.23}$$

where Λ is the cut-off momentum which is often assumed to be the Planck mass. The corrections above have an opposite sign; furthermore, the couplings in supersymmetric theories are given by $\lambda_s = |\lambda_f|^2$. Moreover, in supersymmetry the fermionic and bosonic degrees of freedom should be equal. As a result, every fermion has two scalar superpartners that have the same mass. Therefore, the

second correction should be multiplied by a factor of 2. As a result, the two corrections cancel exactly and therefore the Higgs mass is protected to every order of perturbation theory.

4.3 SUSY Solution to the Cosmological Constant Problem

In this section, we closely follow the corresponding part in [7]. An interesting point about supersymmetry is that, although it is not made to solve the problems of dark energy, dark matter, or even the hierarchy problem, it has major impacts on them or even offers full solutions to them. To illustrate the cosmological impact of supersymmetry [8], we assume space-time is flat. This is certainly not a realistic assumption since the energy content of the universe is not zero. In supersymmetry, using the anti-commutation relation Eq. (4.14), the Hamiltonian takes the form

$$H = \sum_{\alpha} \{Q_\alpha, Q_\alpha^\dagger\}. \tag{4.24}$$

In a completely supersymmetric state when supersymmetry is not broken

$$Q_\alpha \left|0\right\rangle = Q_\alpha^\dagger \left|0\right\rangle = 0, \tag{4.25}$$

and the vacuum energy of the system can be calculated:

$$\left\langle 0\right| H \left|0\right\rangle = 0. \tag{4.26}$$

In other words, except for the sign that is opposite, contributions to the vacuum energy from fermions are equal to those of bosons and therefore the two cancel out and make the value of the cosmological constant vanish. Although this looks like a solution, it is only a trivial result and has no practical usage. The problem is that we haven't seen the superparticles yet and therefore there should not exist a completely supersymmetric state. Equation (4.14) means that the vacuum energy of the system is positive definite. If signs of supersymmetry are found in 2015 at the LHC, the cutoff mass in Eq. (2.32) will be $M_{\text{cut\_off}} = M_{\text{SUSY}} \sim 10^3$ GeV and therefore

$$\rho_{\text{vac}} \sim 10^{12}\,\text{GeV}^4, \tag{4.27}$$

hence

$$\frac{\rho_{\text{exp}}}{\rho_{\text{obs}}} \sim 10^{59}. \tag{4.28}$$

Comparing with Eq. (2.35), the ratio is improved from 10^{123} to 10^{59}. From this result one can claim that the cosmological constant problem is solved halfway [9]. Fortunately this is not the whole story. To measure the true value of the vacuum

energy, gravitational effects need to be taken into account. In fact, if supersymmetry is realized in nature, one has to measure the cosmological constant within the context of supergravity. This is also because our universe is not represented by a flat space-time. As a result, all our calculations above need to be done again within the new framework. In supergravity, the vacuum energy is equivalent to the vacuum expectation value of the following potential [10–13]:

$$V = \exp(8\pi GK)(K^{i\bar{j}} D_i W D_{\bar{j}} \bar{W} - 24\pi G|W|^2), \tag{4.29}$$

where W is the superpotential and is a function of the scalar field, if we are interested in a scalar field. K is the Kahler potential, where the Kahler derivative is defined as

$$D_i W = \frac{\partial W}{\partial \phi^i} + 8\pi G \frac{\partial K}{\partial \phi^i} W, \tag{4.30}$$

and the Kahler metric is

$$K^{i\bar{j}} = \frac{\partial^2 K}{\partial \phi_i \partial \bar{\phi}_{\bar{j}}}. \tag{4.31}$$

In a pure supersymmetric system, when the symmetry is not broken, $D_i W = 0$. Due to the existence of a negative sign in Eq. (4.29), it is always possible to find a scenario in which supersymmetry is broken in a way that $V \sim 0$. However, this does not solve the cosmological constant problem because another fine-tuning is introduced unless one can find a Kahler potential that automatically and without fine-tuning provides an equilibrium in which $V \sim 0$. As is shown by Cremmer et al. in 1983, there exists at least a class of such potentials. Here the Kahler potential is given by

$$K = -\frac{3}{8\pi G} \ln \mid T + T^* - h(C^a, C^{a*}) \mid + \tilde{K}(S^n, S^{n*}) \tag{4.32}$$

and the superpotential is given by

$$W = W_1(C^a) + W_2(S^n), \tag{4.33}$$

where T, C^a, and S^n are all chiral scalar fields, and h and $\tilde{K}$ are both real. There is no further restriction on the functionality of h, $\tilde{K}$, W_1, and W_2 and therefore we can make sure that there is no fine-tuning in place. There are other problems that need to be addressed before one can claim that supersymmetry can solve the dark energy problem. One is the fact that supergravity is not a renormalizable theory. This is something inherited from the general theory of relativity and has less to do with supersymmetry principles; it may be fixed if one day a renormalizable theory of gravity is realized. Another problem with supergravity solutions to the cosmological constant problem is that the form of the potentials in Eqs. (4.32) and (4.33) is not supported by any known physical principle.

Although supersymmetry is an interesting and more importantly self-consistent theory that offers a couple of solutions to existing problems in physics, the author remains skeptical about it. By reviewing the history of physics, we can find no example that resembles supersymmetry. When special relativity was introduced, one only needed to assume that speeds we observe in daily life are much smaller than the speed of light in order to recover Newtonian physics. The same story is true about quantum mechanics. If one assumes that the Planck constant, h, is extremely small compared to values that are encountered in daily life, one can recover every piece of Newtonian physics. We would like to mention that in Dirac's relativistic field theory, the fact that the number of particles was suddenly doubled could be taken, mistakenly, analogous to supersymmetry. However, Dirac only assumed quantum mechanics and special relativity and nothing else. Supersymmetry is different from all of these examples in the sense that simply assuming superalgebras does not lead to a physically acceptable theory. To rescue supersymmetry from being killed by current observations, one needs to make too many assumptions about the values of too many parameters that exist in supersymmetry. Although there is no principle in physics that rules out such a theory, the author would like to wait for a confirmation of the theory through experimental data before starting to believe in supersymmetry. This is exactly the justification for the author's contribution to experimental searches for supersymmetry, to be discussed in later chapters.

References

1. S.P. Martin, Adv. Ser. Direct. High Energy Phys. **18**, 1 (1998) [arXiv:hep-ph/9709356]
2. I. Aitchison, *Supersymmetry in Particle Physics: An Elementary Introduction* (Cambridge University Press, Cambridge, 2007)
3. H. Müller-Kirsten, A. Wiedemann, *Introduction to Supersymmetry* (World Scientific, Singapore, 2010)
4. S.R. Coleman, J. Mandula, Phys. Rev. **159**, 1251 (1967)
5. Y.A. Golfand, E.P. Likhtman, JETP Lett. **13**, 323 (1971)
6. R. Haag, J.T. Lopuszanski, M. Sohnius, Nucl. Phys. B **88**, 257 (1975)
7. S. Weinberg, Rev. Mod. Phys. **61**, 1 (1989) [arXiv:astro-ph/0005265]
8. B. Zumino, Nucl. Phys. B **89**, 535 (1975)
9. S.M. Carroll, Living Rev. Relativ. **4**, 1 (2001) [arXiv:astro-ph/0004075]
10. E. Cremmer, B. Julia, J. Scherk, S. Ferrara, L. Girardello, P. van Nieuwenhuizen, Phys. Lett. B **79**, 231 (1978)
11. E. Cremmer, B. Julia, J. Scherk, S. Ferrara, L. Girardello, P. van Nieuwenhuizen, Nucl. Phys. B **147**, 105 (1979)
12. R. Barbieri, S. Ferrara, D.V. Nanopoulos, K.S. Stelle, Phys. Lett. B **113**, 219 (1982)
13. E. Witten, J. Bagger, Phys. Lett. B **115**, 202 (1982)

Chapter 5
The Large Hadron Collider

The Large Hadron Collider (LHC), located at the European Organization for Nuclear Research (CERN) in Geneva, Switzerland, is the largest particle accelerator in the world. With this extraordinary machine, physics at the TeV scale is within human reach. It is a 27 km double ring located 100 m underground.

The decision to build the LHC at CERN was strongly influenced by the cost savings associated with reusing the Large Electron-Positron (LEP) tunnel and its injection chain. The original LEP machine was only made possible by something that was once referred to as the exo-geographic transition. Although CERN was endowed with a generous site in the Swiss countryside at the time it was founded, with an adjacent site for expansion into the even emptier French countryside, the need for space was felt when the super-proton synchrotron was proposed. In this instance, the problem was solved by extensive land purchases, but the next machine, LEP, with its 27 km ring, made this solution impractical. In France, the ownership of land includes the underground volume extending to the center of the earth, but, in the public interest, the government can buy the rights to the underground part for a purely nominal fee. In Switzerland, a real estate owner only owns the land down to a reasonable depth. Accordingly, the host states reacted quickly and gave CERN the right to make tunnels under the two countries, effectively opening an infinite site that only needed a few islands of land ownership for shafts. In 1989, CERN started operating LEP, the world's highest energy electron-positron collider. In 2000, LEP was closed and made its tunnel available for the LHC. The LHC design depends on some basic principles linked with the latest technology. Being a particle-particle collider, there are two rings with counter-rotating beams, unlike particle-antiparticle colliders that can have both beams sharing a single ring. The LHC ring was originally designed for LEP, and there were eight crossing points connected by long straight sections for RF cavities that compensated for high synchrotron radiation losses. A proton machine such as LHC does not have the same synchrotron radiation problem and would, ideally, have longer arcs and shorter straight sections for the same circumference, but accepting the tunnel as built was

A. Borzou, *Theoretical and Experimental Approaches to Dark Energy and the Cosmological Constant Problem*, Springer Theses,
https://doi.org/10.1007/978-3-319-69632-4_5

the cost effective solution. However, it was decided to equip only four of the possible eight interaction regions and to suppress beam crossings in the other four to prevent unnecessary disruption of the beams. Of the four chosen interaction points, two were equipped with new underground caverns.

5.1 Principal Parameters

The LHC is designed to collide proton beams at a center-of-mass energy $\sqrt{s}$ of 14 TeV, although this design energy has not been achieved yet. The highest proton-proton collision energy so far is $\sqrt{s} = 13$ TeV, recorded during 2015–2016 operation.

The number of a particular type of particle collision occurring at the LHC is given by the equation

$$N = \sigma L, \tag{5.1}$$

where σ is the cross section of that particular type of collision and L defines the instantaneous luminosity, which can be given with beam parameters by

$$L = \frac{N_b^2 n_b f_{\text{rev}} \gamma_r}{4\pi \epsilon_n \beta *} F. \tag{5.2}$$

A description of these parameters as well as their values, based on [1], is given in Table 5.1.

The bunch mentioned in the table refers to a group of protons that are arranged in a small volume of space. In the LHC, protons are arranged in a large number of these bunches in order to help accelerating and steering the protons and controlling

Table 5.1 A description of parameters defining the instantaneous luminosity in early Run 2

Item	Value	Description
N_b	1.15×10^{11}	The number of particles per bunch
n_b	2240	The number of bunches per beam
f_{rev}	11.245 kHz	The revolution frequency
γ_r	$\frac{1}{\sqrt{1-(\frac{v}{c})^2}}$	The relativistic gamma factor set by the energy of the beam
ϵ_n	3.5 μm	The normalized beam emittance, a measure of the spread of the beam in the plane transverse to its motion
$\beta *$	0.8 m	The value of the beam amplitude function β at the point of collision, a measure of the focusing strength of the magnets at the collision point
F		The geometric luminosity reduction factor due to the crossing angle at the interaction point

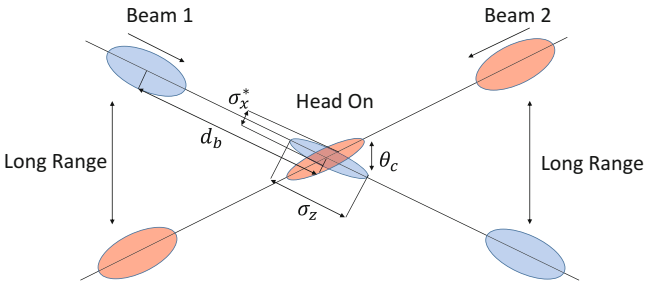

Fig. 5.1 The crossing angle θ_c, the RMS bunch length σ_z, and the transverse RMS beam size $\sigma*$, which are used in determining the geometric luminosity

their collision points. The number of protons per bunch and the number of bunches per beam during the nominal operation of the LHC in 2015 are presented in the table. Also, the geometric luminosity, F, is defined as

$$F = \left(1 + \left(\frac{\theta_c \sigma_z}{2\sigma*}\right)^2\right)^{-1}, \tag{5.3}$$

where the crossing angle θ_c, the RMS bunch length σ_z, and the transverse RMS beam size $\sigma*$ are illustrated in Fig. 5.1.

In addition to the instantaneous luminosity L, we often talk about the integrated luminosity L_{int} defined by

$$L_{\text{int}} = \int L dt. \tag{5.4}$$

The delivered luminosity is defined as the integrated luminosity delivered from the start of stable beams until the LHC requests the experiments like CMS to turn off its sensitive detectors. On the other hand, the recorded luminosity is defined as the subset of the delivered luminosity that was recorded. These two are in general different because the CMS detector is not always fully operational due to technical issues, for example. The delivered and recorded luminosities in the early phase of Run 2 are shown in Fig. 5.2.

There are two general purpose experiments at the LHC, CMS, and ATLAS. There are two other experiments at the LHC called LHCb, which is used to study bottom-quark physics, and ALICE, which is optimized to study heavy ion collisions. The CMS and ATLAS detectors are designed for operating with an instantaneous luminosity of $L \sim 10^{34}\,\text{cm}^{-2}\,\text{s}^{-1}$, while the LHCb detector is designed for proton collisions around $L \sim 10^{32}\,\text{cm}^{-2}\,\text{s}^{-1}$. The ALICE detector's target luminosity is $L \sim 10^{27}\,\text{cm}^{-2}\,\text{s}^{-1}$. The locations of these experiments around the LHC ring are shown in Fig. 5.3.

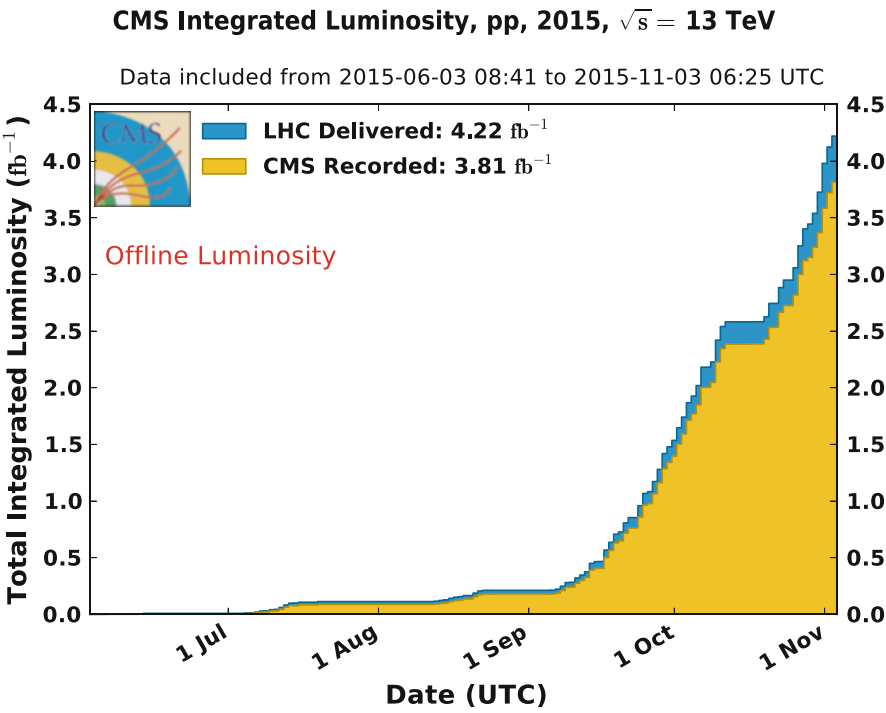

Fig. 5.2 Total delivered luminosities in 2015 at the center-of-mass energy of 13 TeV

5.2 Acceleration Chain

In this section we give a brief review of the beam injection chain at CERN, which is illustrated in Fig. 5.4. Protons that are used for the collisions are first produced by applying an electric field and ionizing the hydrogen gas in a tank. The protons then enter the Linac2 (http://home.cern/about/accelerators/linear-accelerator-2), which has linear conductors and uses radiofrequency cavities to accelerate them. The protons pass through the conductors, and due to the electric field that exists inside the conductors, they get accelerated to an energy of 50 MeV. Next they are guided through the Proton Synchrotron Booster (PSB) (http://home.cern/about/accelerators/proton-synchrotron-booster) and accelerated to an energy of 1.4 GeV. The PSB is made of four superimposed synchrotron rings. Next, protons are injected into the Proton Synchrotron (PS) (http://home.cern/about/accelerators/proton-synchrotron), a 628 m ring containing 277 conventional magnets to bend the beam around the synchrotron. Here the protons reach an energy around 25 GeV. After this the protons enter the second largest machine in the CERN's accelerator complex, the Super Proton Synchrotron (SPS) (http://home.cern/about/accelerators/super-proton-synchrotron), which is 7 km long and contains 1317 conventional electromagnets to keep the protons in the ring around the machine and accelerate

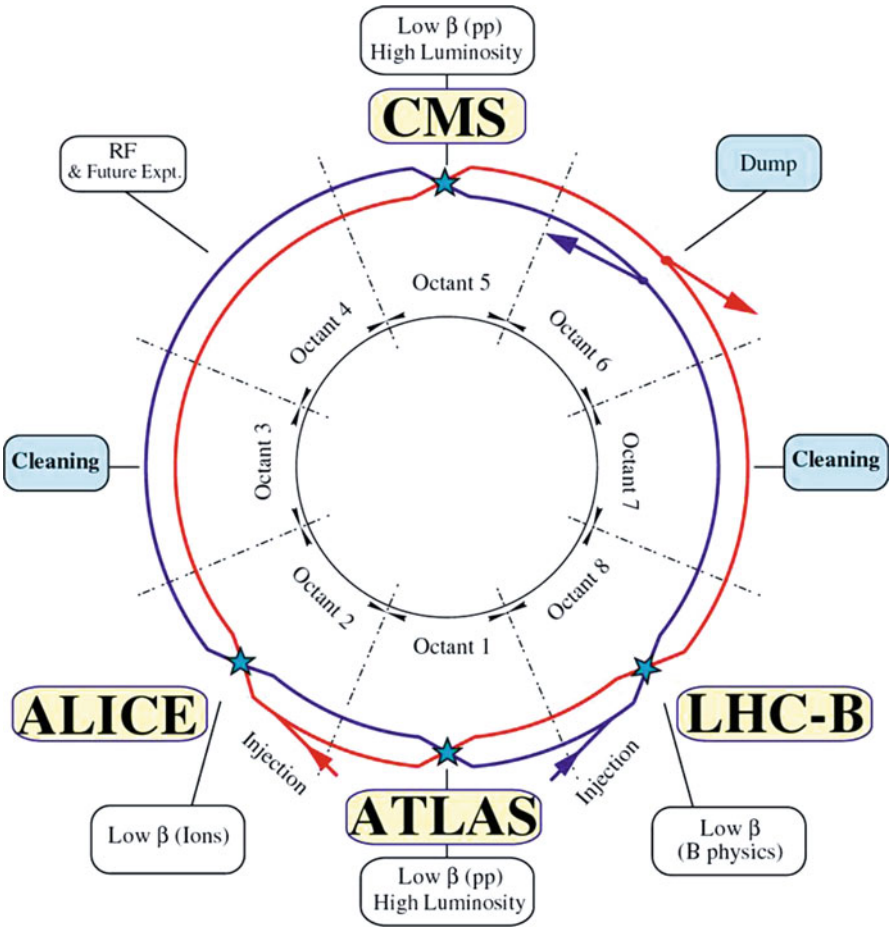

Fig. 5.3 The LHC ring is divided into eight different octants. Blue stars locate the position of four major experiments around the LHC

them to 450 GeV. The SPS was the major particle accelerator at CERN in 70s and 80s when physicists used the machine to probe the exotic forms of matter, the inner structure of protons, and matter-antimatter asymmetry. Also, the Nobel winning discovery of the W and Z bosons was made by the Underground Area 1 (UA1) and Underground Area 2 (UA2) experiments at the SPS. When the protons reach the energy of 450 GeV, they are injected into the principal ring of the LHC from two different points and circulate for up to 20 min to reach the desired energy of 6.5 TeV.

Significant amounts of information in this chapter come from [1].

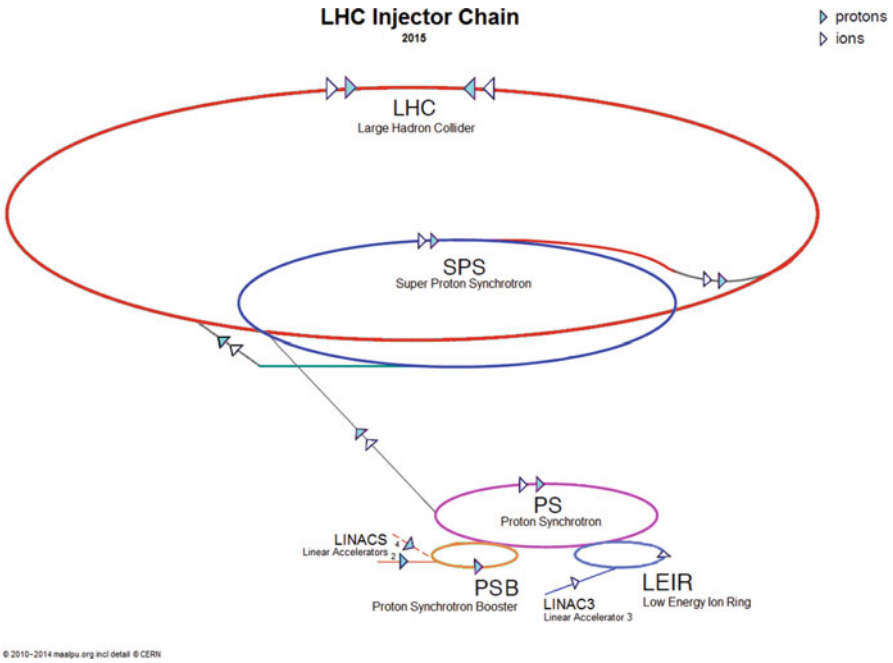

Fig. 5.4 Accelerator chain for the LHC at CERN

Reference

1. L. Evans, P. Bryant, JINST **3**, S08001 (2008)

Chapter 6
The Compact Muon Solenoid

6.1 Overview

In this chapter we briefly review the key elements of the CMS detector. A detailed description of the CMS detector can be found in [1].

The Compact Muon Solenoid (CMS) is one of the two general purpose detectors designed to examine not only all of the particles known to exist in the standard model (SM) but also particles that may exist beyond the standard model. The dimensions of the CMS detector are shown in Table 6.1. The location of the CMS detector is shown in Fig. 6.1, where the conventional coordinate system used by the CMS collaboration is also presented. As the figure indicates, the coordinate system is chosen such that the x axis is toward the center of the LHC ring, the y axis is pointing upward, and the z axis is in the direction of the beams, such that the coordinate system is right handed. The ϕ angle is defined in the x–y plane measured from the x axis. The θ angle, as in spherical coordinates, is defined with respect to the z axis. However, it is more convenient to define the pseudorapidity

$$\eta = -\ln\left[\tan\left(\frac{\theta}{2}\right)\right], \tag{6.1}$$

which can be seen in Fig. 6.1. One important phrase that we often encounter in the CMS collaboration is the word "transverse," which refers to quantities measured in the x–y plane. Therefore, the transverse momentum, for example, is defined as $p_{\mathrm{T}} = |\vec{p}|\sin\theta$.

The shape of the CMS detector is approximately cylindrical with its z axis aligned to that of the coordinate system. It is made of several layers, each of which are subdetectors. There are endcaps at the two ends of the cylinder that extend the coverage of the detector. A layout of different CMS subdetectors is shown in Fig. 6.2 and described in more detail in the following sections.

A. Borzou, *Theoretical and Experimental Approaches to Dark Energy and the Cosmological Constant Problem*, Springer Theses,
https://doi.org/10.1007/978-3-319-69632-4_6

Table 6.1 Dimensions of the CMS detector

Item	Value
Length	21.6 m
Diameter	14.6 m
Weight	13,800 tons

Fig. 6.1 Location of the CMS detector and its conventional coordinate system

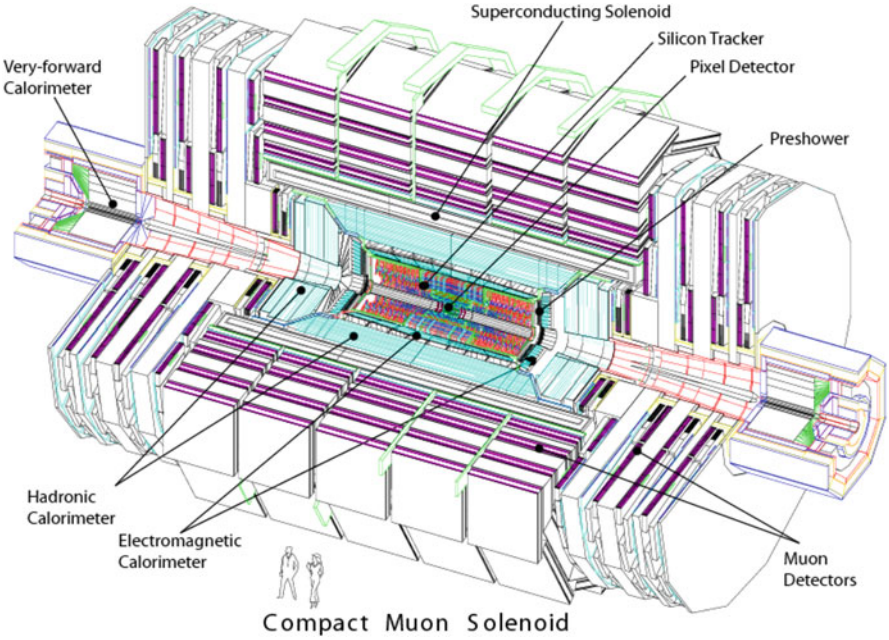

Fig. 6.2 Different sections of the CMS detector

6.2 Tracking System

The tracking system is at the center of the CMS detector and uses silicon technology to measure the tracks of charged particles that originate from the collision point and bend in the 3.8 T magnetic field of the CMS solenoid. In each bunch crossing, hundreds or thousands of particles pass through the tracker. This necessitates a detector with a quick response and high granularity. These features are needed to ensure precise measurements of charged particle trajectories. Moreover, the detector should be extremely resistant to high intensity radiation from the collisions. Building a detector that would operate for as long as 10 years in an intense radiation environment was the main challenge during the development of the CMS tracking system. On the other hand, silicon detector technology has proven to be relatively radiation safe, as the detector contains only a small amount of material and it responds pretty quickly to hits from charged particles crossing its layers. All these features together make silicon detectors a suitable choice for the CMS tracking system.

The tracking system consists of the pixel detector and the silicon strip tracker, which itself is made of the inner tracker and the outer tracker. These are located at different positions in the CMS detector, as is illustrated in Fig. 6.3.

6.2.1 The Pixel Detector

The pixel detector is only $\sim$4 cm from the z axis, making it the closest element of the detector to the beam line. It is made of silicon pixel detectors, each having a dimension of 100 μm $\times$ 150 μm $\times$ 250 μm. In the central region, the pixel detector is made of three barrels each 53 cm long, which are located at distances of 4.4, 7.3, and 10.2 cm from the z axis. There also exist four endcap disks with radii ranging from 6 to 15 cm, located at $\pm$34.5 and $\pm$46.5 cm along the z axis. The pixel detector records three hits per track and provides a seed to the outer part of the tracking system.

6.2.2 The Silicon Strip Tracker

There are three major subsections of the strip tracker detector:

- The tracker inner barrel (TIB) and disks (TID),
- The tracker outer barrel (TOB),
- The tracker endcaps (TEC),

which are shown in Fig. 6.3. The four layers of the tracker inner barrel and the three disks of the tracker inner disks are located from $r = 20$ cm to $r = 55$ cm. These are, unlike the pixel tracker, located in a region with less radiation flux and are made of

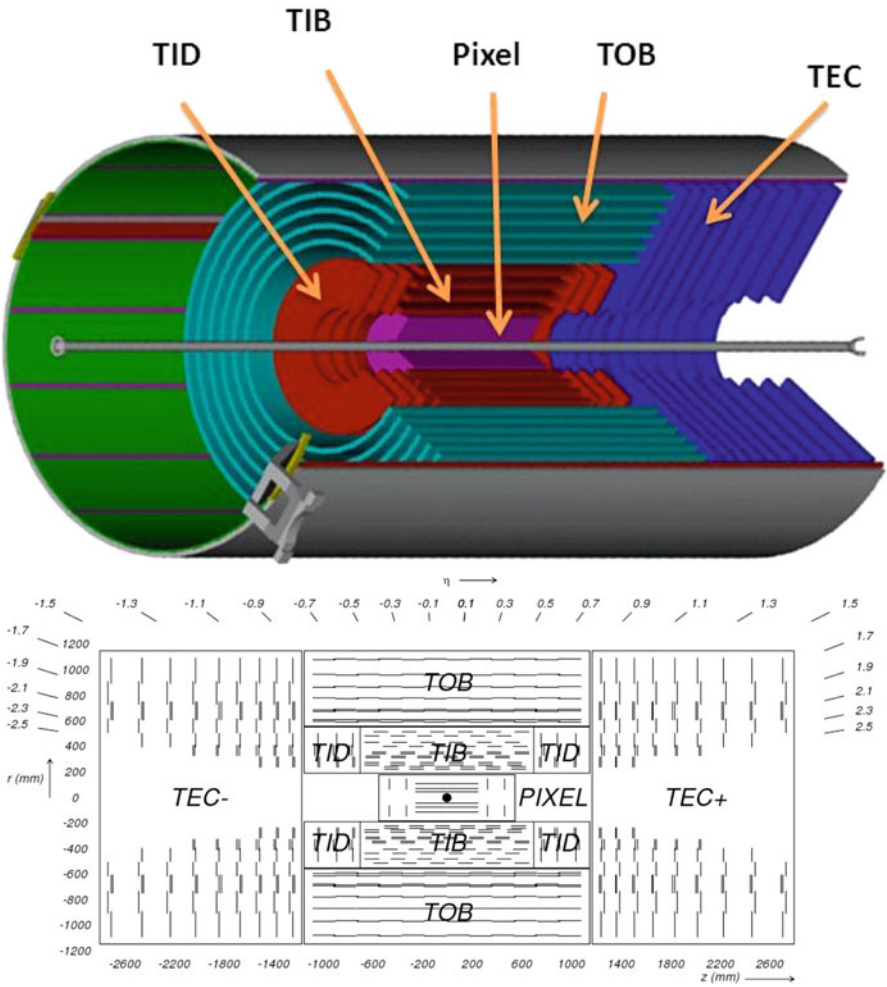

Fig. 6.3 (Top) A graphical illustration of the tracking system around the z axis. (Bottom) The r–z view of the tracking system. The tracking system is symmetric around both z and r, which is the distance from the z axis in the x–y plane. The lines indicate detector modules

silicon microchips. Next to the inner trackers are the six layers of the tracker outer barrel (TOB), which extend from $r = 55\,\text{cm}$ to $r = 116\,\text{cm}$ in the x–y plane and $z = -118\,\text{cm}$ to $z = 118\,\text{cm}$ in the r–z plane. Lastly, the nine layers of the tracker endcaps are located between $r = 22.5\,\text{cm}$ and $r = 113.5\,\text{cm}$ in the x–y plane and between $z = \pm 124\,\text{cm}$ and $z = \pm 282\,\text{cm}$ in the r–z plane.

6.2.3 *Performance of the Trackers*

The silicon trackers at CMS are designed such that accurate measurements of charged particles hitting them are possible and therefore the vertex as well as the tracks can be reconstructed efficiently. The hit resolution in the silicon tracker has been studied by measuring residuals, defined as the difference between the measured and the expected hit position as predicted by the fitted track. For a track that has a transverse momentum greater than 12 GeV, the resolution in the x–y plane is measured to be $\sim 10\,\mu\text{m}$. In the r–z plane, however, the resolution depends on how tracks hit the sensors and it ranges from ~ 14 to $\sim 36\,\mu\text{m}$ [2, 3]. The track reconstruction efficiency is measured by studying how often we find a well reconstructed and isolated track originating from the primary vertex. The efficiency is $\sim 99\%$, which is extremely high [2].

6.3 Electromagnetic Calorimeter

Photons and electrons deposit their energies in the electromagnetic calorimeter (ECAL), which is located directly outside of the tracking system. A thorough review of the CMS electromagnetic calorimeter is given in [4, 5] and its layout is shown in Fig. 6.4. The electromagnetic calorimeter has two major sections. The electromagnetic barrel (EB) calorimeter has a volume of $8.14\,\text{m}^3$ and its closest point to the z axis is at $r = 129\,\text{cm}$. The electromagnetic endcap (EE) calorimeter is located at $z = \pm 315\,\text{cm}$. Both sections are built symmetrically and homogeneously over the x–y and r–z planes. The coverage of the ECAL is $|\eta| < 3$, which is a relatively large angle. Electromagnetic calorimeters measure the energy of electrons and photons as they interact with the charged particles in the dense material of the detector volume and make "electromagnetic" showers consisting of secondary electrons and photons. Here we use the fact that charged particles decelerating through matter emit photons via bremsstrahlung radiation. These radiated photons, as well as prompt photons from collisions, decay to an electron-positron pair when passing within the material and these particles also start to lose their energy through bremsstrahlung radiation. This cycle continues until the energy of the electrons and photons falls below a threshold and the loss of their energies by ionization dominates. The characteristic thickness of the material in the ECAL is the radiation length X_0. This X_0 is the mean distance over which a high energy electron loses e^{-1} of its energy by bremsstrahlung radiation, and $7/9$ of the mean free path for pair production for a high energy photon. The whole volume of the CMS ECAL detector is used to initiate electromagnetic showers and also as a scintillator to detect the deposited energy by particles created in the showers. The material necessary for scintillation must have a quick response, be resistant to harsh radiation, and also be compact in volume. Therefore, lead tungstate ($PbWO_4$) was chosen for building the scintillator crystals. The barrel ECAL is made of 61,200 $22 \times 22\,\text{mm}^2$ crystals

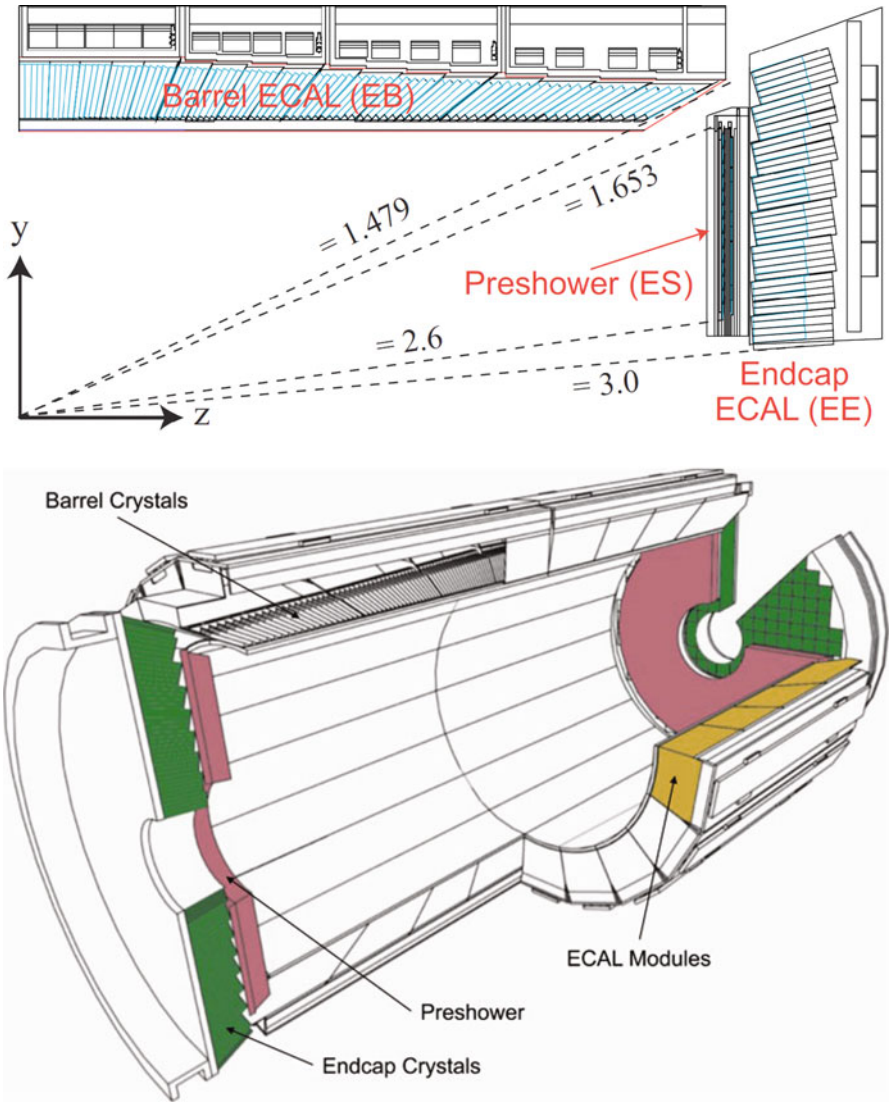

Fig. 6.4 Layout of the electromagnetic calorimeter within the CMS detector. As shown here, the subdetector is divided into the barrel and endcap

where each is 23 cm long, corresponding to $25.8X_0$, while the endcaps contain 7324 crystals with an area of $28.6 \times 28.6\,\text{mm}^2$ and a length of 22 cm, corresponding to $24.7X_0$. In front of the endcaps there is a preshower detector (ES) to discriminate between prompt photons and pairs of photons that result from a neutral pion decay.

When a scintillator is ionized or excited by a shower resulting from energy of electrons and photons, it emits a light which is considered as a signal. This signal is read by avalanche photodiodes (APD) in the barrels and by vacuum phototriodes (VPT) in the endcaps. This process is very temperature dependent and therefore the temperature of the environment needs to be monitored regularly.

A very important aspect of the electromagnetic calorimeter is its energy resolution [6] which is measured using $Z \rightarrow e^+e^-$ for electrons and using $Z \rightarrow \mu^+\mu^-\gamma$ for photons. The energy resolution σ can be written in terms of a stochastic term S, a noise term N, and energy E in the following form:

$$\left(\frac{\sigma}{E}\right)^2 = \left(\frac{S}{\sqrt{E}}\right)^2 + \left(\frac{N}{E}\right)^2 + C^2, \tag{6.2}$$

where C is a constant. The values of the different parameters in this equation are obtained through test beam measurements and are

$$S = 0.028\,\sqrt{\text{GeV}},$$
$$N = 0.12\,\text{GeV},$$
$$C = 0.003.$$

The electromagnetic calorimeter energy resolution as a function of the energy of electrons is given in Fig. 6.5.

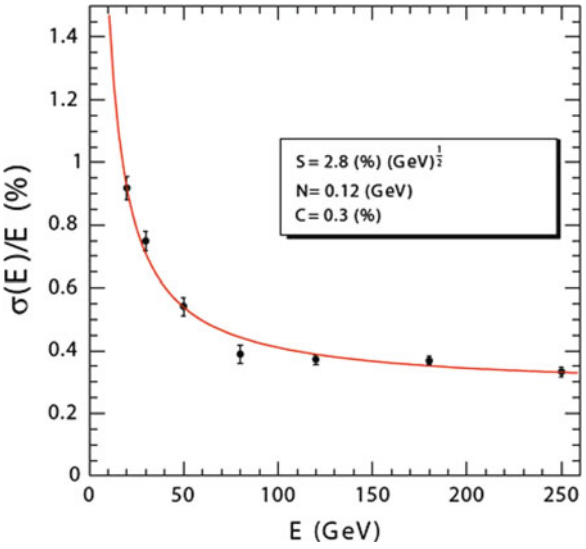

Fig. 6.5 The resolution of electron energy in the ECAL subdetector

6.4 Hadronic Calorimeter

Directly outside the ECAL detector is the hadronic calorimeter (HCAL), which measures the energy of hadrons passing through it. Hadrons, composed of quarks and gluons, interact with the nuclei of the materials in the HCAL and develop hadronic showers. Unlike the ECAL case, here the interactions are governed by quantum chromodynamics (QCD). The hadrons produced in pp collisions start interacting in the active material of the HCAL and develop their own showers. This process continues until their energy falls below the level that can excite or ionize the scintillators. The scintillators emit light that will be read out by photosensors. Analogous to the radiation length in the ECAL, one can define a nuclear interaction length λ_I that contains e^{-1} of the energy in a shower. It is longer than the radiation length in the ECAL because the typical cross section is smaller for a nuclear interaction than for an electromagnetic interaction. The HCAL is a sampling calorimeter in the sense that it does not need complete containment of the shower in one single absorber. In the HCAL, plastic scintillators, whose relatively low price is the reason for using them, are interleaved with massive and thick absorbers made of steel and brass. The hadronic calorimeter is made of four major sections that are reviewed below and depicted in Fig. 6.6.

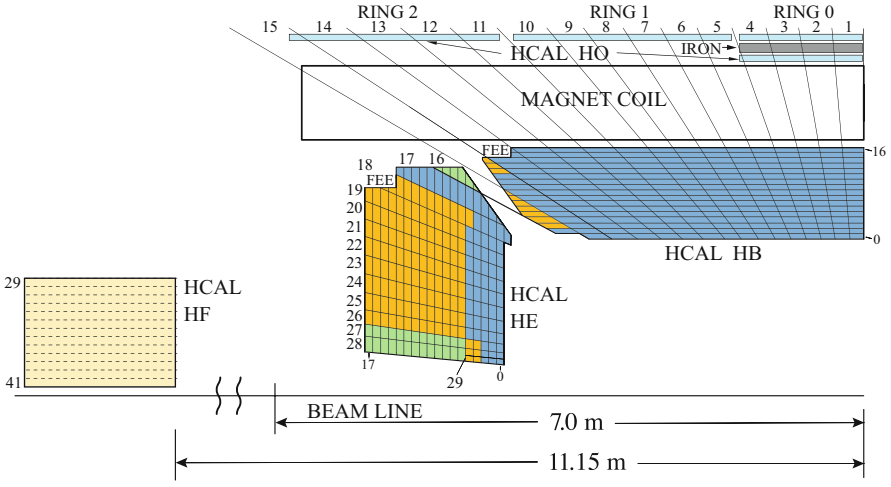

Fig. 6.6 One-quarter view of the hadronic calorimeter detector in the r–z plane

6.4.1 The HCAL Barrel (HB)

The first section of the hadronic calorimeter is the barrel (HB), which is located directly outside the ECAL and is therefore inside the magnetic solenoid. It covers a pseudorapidity of $|\eta| < 1.392$ and will be discussed in the next section. The HB is segmented into 16 columns in η on each η side and into 72 towers for the whole 2π azimuthal area. Therefore, the segmentation of the HB is $\Delta\eta \times \Delta\phi = 0.087 \times 0.087$.

6.4.2 The HCAL Outer Calorimeter (HO)

The second part of the hadronic calorimeter is the HO, or outer calorimeter. This section is complementary to the HB and is located outside of the solenoid magnet. The reason for extending the HCAL to this outer area is the low probability of strong interactions that happen inside the absorbers and therefore generate the need for larger detector thickness. The HO coverage is slightly smaller than HB and is $|\eta| < 1.3$. The solenoid magnet plays the role of the first absorber for the HO, initiating part of the showers that are detected in the HO. The segmentation of the HO in azimuthal and polar angles is the same as that of the HB.

6.4.3 The HCAL Endcaps (HE)

The barrel calorimeter provides limited coverage in polar angle and therefore needs to be supplemented by two endcaps (HE) covering $|\eta|$ from 1.3 to 3. The segmentation of the HE in the polar and azimuthal angles is different for different pseudorapidities. The segmentation in η ranges from $\Delta\eta = 0.087$ for $|\eta| < 1.74$ to $\Delta\eta = 0.35$ at the highest $|\eta|$. The segmentation in ϕ is $\Delta\phi = 5^\circ$ (0.087 radians) for $|\eta| < 1.74$ and 10° for higher $|\eta|$. In the central region the energy resolution is given by

$$\left(\frac{\sigma}{E}\right)^2 = \left(\frac{0.09}{\sqrt{E}}\right)^2 + (0.045)^2\,, \tag{6.3}$$

where E is the energy of a hadron.

6.4.4 The HCAL Forward Calorimeter (HF)

To extend the coverage of the HCAL to $|\eta| < 5.2$, two forward calorimeters (HF) are located far from the center of the collision along the z axis at $z = \pm 11.2$ m. The HF is designed to detect the Cherenkov radiation from particle showers. There is

no electromagnetic calorimeter in front of it, so the HF serves to measure both electromagnetic and hadronic showers. Here, since the radiation dose is much larger than in the central region, i.e., the barrel and endcap, quartz fibers are used instead of plastic scintillators. Also unlike the central regions where the absorbers are mainly made of brass, those in HF contain more steel. The segmentation in HF also varies over the polar angle. It is $\Delta\eta \times \Delta\phi = 0.175 \times 0.175$ for $|\eta| \leq 4.7$ and increases up to $\Delta\eta \times \Delta\phi = 0.35 \times 0.35$ for $|\eta| > 4.7$. The energy resolution σ is given by

$$\left(\frac{\sigma}{E}\right)^2 = \left(\frac{1.72}{\sqrt{E}}\right)^2 + (0.09)^2\,, \tag{6.4}$$

where E is the energy of a hadron.

6.5 Superconducting Solenoid

As mentioned before, there is a need for a strong magnetic field in the interior part of the CMS detector to bend the motion of charged particles and make momentum measurements possible based on the curvatures of their trajectories. It will be shown in the next section that there is a need for a magnetic field in the outer region of the detector where the muon chambers are located. These magnetic fields are generated by a superconducting solenoid that surrounds the tracker system, as well as major sections of the ECAL and the HCAL.

The solenoid is 13 m long with an interior diameter of 6 m, and it is the largest superconducting magnet in the world. At full functionality, it is capable of storing an energy of around 2.6 GJ by producing a magnetic field of 3.8 T in the interior region. While the tracker and the calorimeters are inside the magnet coil, the muon chambers, which will be discussed next, are outside the magnet coil. The muon chambers are interleaved with a 12-sided iron structure that contains the magnetic field for the muon chambers. This secondary magnetic field is only 2 T and is generated by returning the magnetic flux of the coils through a 10,000-ton iron yoke. The superconducting solenoid and the iron return yoke, as well as the direction of the magnetic fields in different parts of the CMS detectors, can be seen in Fig. 6.7.

6.6 Muon System

The muon chambers are the outermost layers of the CMS detector. Muons are basically the only charged particles that penetrate through the inner detectors discussed earlier and are detected in these chambers. Here, the gaseous chambers are interleaved in the iron return yoke in order to measure the momentum of the muons. The muon system can be divided into two major sections, the barrel and the endcaps. These two are themselves made of different subdetectors and are illustrated in Fig. 6.8 and explained below.

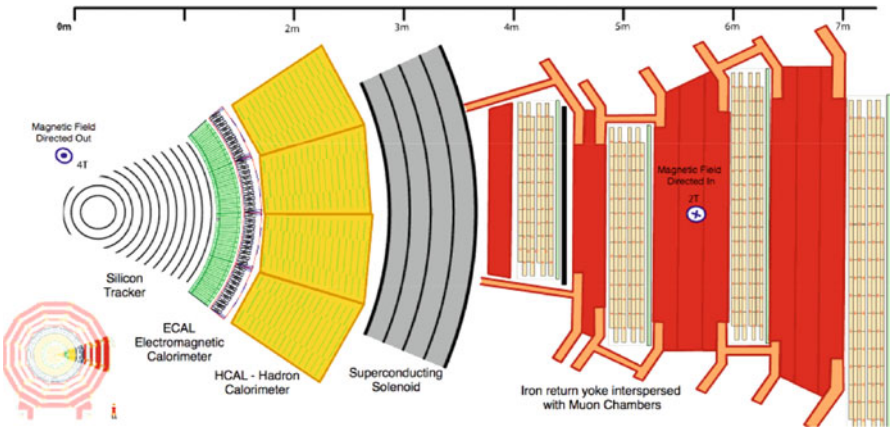

Fig. 6.7 A slice of the CMS detector in which the superconducting solenoid, the iron yoke, and the direction of the magnetic fields are illustrated

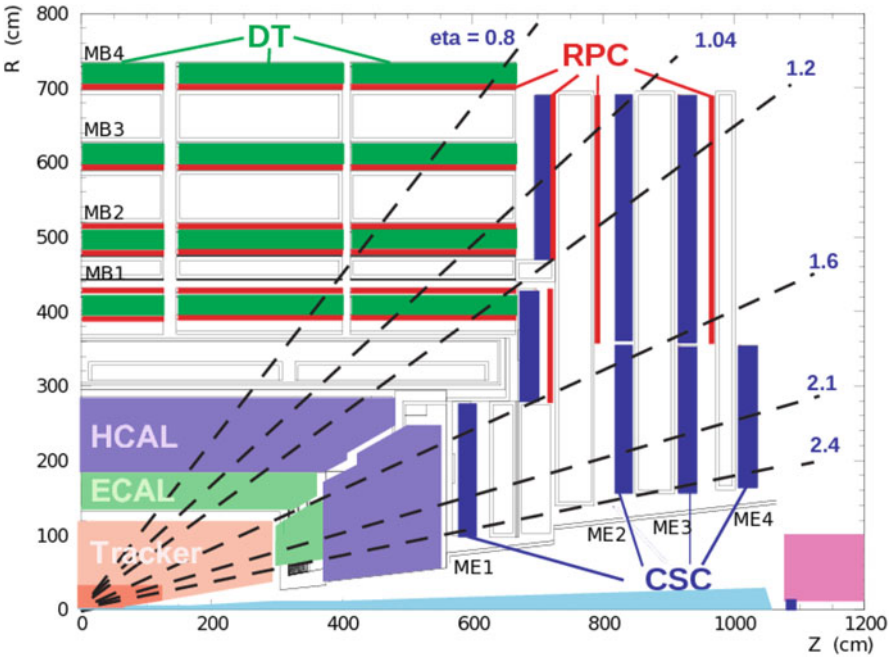

Fig. 6.8 A quarter layout of the muon system in the barrel and the endcap region

The barrel section is made of five iron wheels among which the muon stations are located. The iron wheels are themselves made of 12 azimuthal sectors. In this area the hit occupancy is not high; therefore, a very quick response is not required, unlike in the endcaps. As a result the gaseous chambers are made of drift tubes (DT).

There are 250 DT chambers located in the barrel section. A DT chamber is made of tiny DT cells which are themselves tubes with a positively charged wire inside, 4 cm wide and filled with a gas. There are 12 (3×4) layers of DT cells in each chamber making the size of the chambers something around 2×2.5 m. The two outer layers of the DT chambers, and eight layers out of twelve, are responsible for measuring the transverse coordinates of the muons, while the middle four layers measure the location along the z coordinate. This middle four layers do not exist in the outermost chamber and therefore that chamber is only capable of measuring x–y coordinates. The four DT chambers, each made of 12 layers as discussed above, are positioned between the five iron return yokes. When a charged particle passes through the DTs, it produces electrons and positively charged ions, which are heavier than electrons. The electrons quickly move toward the anode wire while it takes longer for ions to arrive at the cathode. The charge associated with the electrons is read as signal.

In addition to DT chambers, there are also 610 resistive plate chambers (RPC), which are a different type of gaseous chamber used in both the barrel and endcaps. The RPCs have two resistive plastic plates at two different electric potentials filled with a gas in the area between the plates. On top of one of the plates, there is a readout strip which receives the light generated by the gas when a muon passes through. The RPCs have a time resolution of 1 ns, which corresponds to a very fast response, and they are also radiation resistant, which is why they are used in both the barrel and endcaps. In the barrel there are two layers of RPCs in each of the first two muon stations and one layer in each of last two muon stations. The barrel section covers a polar angle of $|\eta| < 1.2$.

Since the barrel subdetector covers only a limited range of polar angles, two endcap subdetectors are in place to extend the coverage to $|\eta| < 2.4$. The endcaps are made of three iron disks holding four muon stations. Due to the harsh radiation exposure in this section, the gaseous chambers, unlike in the barrel section, are made of 540 cathode strip chambers (CSC). CSCs are chambers containing a gas surrounding six anode wires and seven copper cathode strips. Here the azimuthal position is measured by the anode wires while the cathode strips determine the transverse distance from the z axis. In the endcaps, RPC chambers are also used. Except for the last muon station, each station contains one layer of RPCs.

6.7 Triggers

The frequency of bunch crossings ($\sim$40 MHz) is so high that current technology does not allow the CMS detector to record them all. Moreover, even if it is technologically possible to record all the events, it is still not justified because most of those events are already well understood and physicists would like to analyze only more interesting types of collisions. Therefore, a framework is needed to reduce the drastic rate of events and select the more interesting ones. The framework should still have a high efficiency for recording the data for various areas of interest in

particle physics. Roughly 40 million events per second are generated in the CMS detector. This number should be reduced to several hundreds of events per second.

The trigger system in CMS reduces the rate of events in two steps. The first step, the Level 1 (L1) trigger [7], has been developed to make a very fast decision and reduce the rate from 40 MHz to 100 kHz. It is made of electronic hardware that can be programmed. The second step, the High Level Trigger (HLT) [8], is made of computer programs that run on a huge computing cluster called the event filter farm. These two trigger levels are discussed more in the following sections.

6.7.1 L1 Trigger

The L1 trigger is made of three main components, namely the local, the regional, and the global. The decision on passing or blocking an event, which is made after combining the information from all three major components, should be made in only 3.2 μs. Even if these electronics allow an event to be recorded, it may be blocked due to other subdetectors or data acquisition system not being ready. Electronics at the frontend of the detector store the detailed data needed for a L1 decision, while some coarse data are also collected from the calorimeters and the muon system.

In the calorimeters, the cells of the HCAL and ECAL are considered as the trigger towers, the local part of the trigger, that provide trigger primitives by measuring the transverse energy of hits in the trigger towers. This raw information is then passed to the regional part of the trigger to find the regional candidates for jets, photons, and charged leptons. On the other hand, the information about the total missing energy and the transverse momentum of each event is provided by the global part of the L1 trigger.

The muon system makes up another parallel part of the L1 trigger system. Here, the DT and the CSCs provide information about the tracks and their transverse momenta. RPCs also provide parallel independent information about the regional hit patterns. The information from these three are then passed to the global muon trigger. The latter also receives information from the calorimeter global trigger about the isolation of the muons and finally selects up to four muon trigger candidates and provide their properties like momentum and charge.

Both the global muon and the global calorimeter triggers send their information to the global trigger for the final decision to pass or drop the event. Up to 128 parallel algorithms can be run to make the final decision. The architecture of the L1 trigger is shown in Fig. 6.9.

6.7.2 HLT Trigger

When an event passes the L1 trigger, the data acquisition system reads the event information from the whole detector, at a maximum rate of 100 kHz, and passes

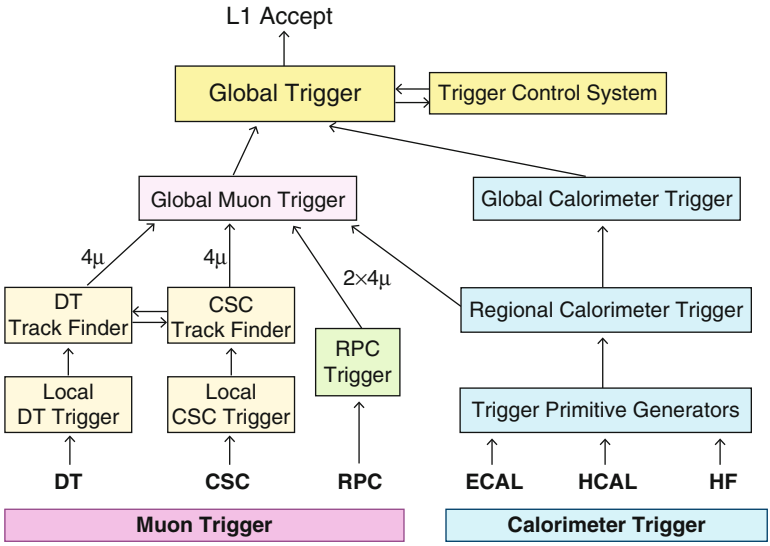

Fig. 6.9 Schematic of the L1 trigger architecture

it to the event filter farm where the HLT algorithms quickly analyze the data and make further selections. The HLT consists of software only. Each HLT filter is called a path and is made of a series of independent pieces of code that decide if an event should be stored or abandoned. These trigger paths are organized into several groups, each of which defines a primary dataset (PD). Paths in a PD are usually triggered by the same objects. SingleMu, for instance, is a PD which contains all the HLT paths that are triggered by at least one muon in the event.

The HLT decision is made in around tens of milliseconds, which is orders of magnitude larger than the time L1 takes for decision making. However, it still needs to stay within the computing and storage capacity limits. The event rate must be low enough such that saving the information on tape is doable while the efficiency of keeping interesting events is maximized. Also the selected events should consist of objects that can be easily reconstructed by the offline reconstruction tools. These are all accomplished by looking at a minimal number of physics objects such as muons or jets, for instance.

6.8 Event and Object Reconstruction

For most of the analyses using CMS data, it is essential to know what the final stable particles in a given event are; therefore, an accurate reconstruction and identification of these particles are inevitable. When a particle emerges from a collision, it will be observed by different subdetectors of CMS. Reconstruction

and identification of the particle means collecting all the information from different subdetectors and combining it to assess the particle type and its kinematic properties based on the measurements by the subdetectors. More accurately speaking, event reconstruction is the process of determining the collision point, the primary vertex, the particles, and the energy and momentum of particles in an event. The CMS experiment employs the Particle Flow (PF) algorithm for event reconstruction. The PF algorithm identifies most of the stable particles, or long-lived ones, using the identified tracks and calorimeter hits in the event. The basic idea is that a charged particle passing through the CMS detector follows a semi-circular path due to the strong magnetic field provided by the CMS solenoid. The curvature of this path depends on the momentum of the particle, whose energy is measured by the calorimeters. In addition, different types of particles interact with each subdetector differently. Therefore by combining these pieces of information, the CMS particle flow algorithm identifies five different types of particles: photons, electrons, muons, charged hadrons, and neutral hadrons. A graphical illustration of the tracks and the hits in the calorimeter is shown in Fig. 6.10 and more details about the PF can be found in [9].

As was highlighted above, reconstructing the tracks in an event is one of the cornerstones of the particle flow algorithm. The track reconstruction uses an iterative strategy described in detail in [10]. The algorithm that reconstructs the tracks in the event starts by first identifying the tracks that can be easily recognized, i.e., tracks with high quality, and then reconstructing them. These tracks tend to have high transverse momentum and emerge from the primary vertex. They also should have passed through all the three layers of the pixel tracker. In the next iteration, tracks similar to those reconstructed in the first iteration but have only two instead of three hits in the pixel detector are reconstructed. In the third iteration, tracks with low transverse momentum are also taken into consideration. At this point, the PF reconstructs muons with an efficiency of 99.5% and charged hadrons with an efficiency of 90%. In the end, tracks emerging from secondary vertices are also reconstructed.

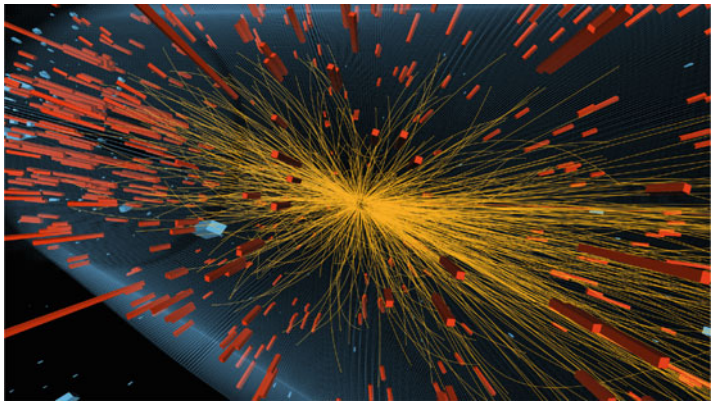

Fig. 6.10 A sample event in a proton–proton collision in the CMS detector

Gathering the information from the HCAL and ECAL calorimeters is another cornerstone of the particle flow algorithm and is performed through the calorimeter clustering algorithm. Through this algorithm the neutral and charged hadrons are distinguished and the energy of photons, neutral and charged hadrons, and electrons is determined. The clustering happens in parallel in the endcap and barrel sections of the ECAL and HCAL. There are three main steps in each of the clustering algorithms. First, the reconstruction starts by finding the calorimeter cells with energy above a threshold. These cells are considered as "cluster seeds." Next, the energy of cells around the primary cell is added and therefore the "topological clusters" are constructed. If there is more than one seed in a topological cluster, each of them gives rise to a "particle flow cluster." In this case the energy of each cell is shared between all of the particle flow clusters depending on the distance between the cell and the cluster.

Identifying a particle happens through the link algorithms and is done by associating a track with a few of PF clusters and at most one muon track. The information from these different algorithms determines the type of the particle. The same algorithm also tries to link different particles together.

In the following subsections we will discuss how different physics objects are reconstructed mostly through the linking algorithms.

6.8.1 Electrons

When an electron is created by a proton–proton collision, it will pass through the tracker system and it deposits its energy in the ECAL. When passing through the tracker, it ionizes the detector and therefore leaves a track. Moreover, when its energy is deposited in the cells in the ECAL, an electromagnetic shower is generated. Therefore, if we find a few PF clusters in the ECAL in the same direction as a charged track and find no PF cluster in the extrapolated direction in the HCAL, it will be considered to be an electron. The energy of an electron is determined by considering the ECAL measurement, the momentum of the track, and the sum of the energy of all the bremsstrahlung photons linked to its track.

6.8.2 Photons

The signature of a photon is no track in any of the tracking systems, including the muon system, plus a deposit of energy in the ECAL. Therefore, if a PF cluster in the ECAL is not associated with any track, it is considered a photon. The reason a photon does not leave a track in the tracker is because it does not carry electric charge, i.e., it is electrically neutral.

6.8.3 Muons

Muons do not shower in the ECAL because they are heavy enough to pass through the ECAL material without emitting bremsstrahlung photons. Muons leave only minimal deposits of energy when passing through the ECAL and HCAL. The linking algorithm extrapolates a track's direction in the tracker and if it is consistent with a track or some hits in the muon system, it will be considered to be a muon. The energy of the muon can be determined by measuring the momentum of its track.

6.8.4 Hadrons

If a charged particle track is not identified as an electron or muon, it is identified as a charged hadron. Also, a charged hadron should cause several showers in the HCAL. A neutral hadron can leave an excess of energy in the ECAL and HCAL. It also cannot be associated with a track. Hence, any indication of these two signs can be considered as a neutral hadron.

6.8.5 Jets

In each event, reconstructed particles are grouped to build an object called a hadronic jet. Jets are reconstructed by clustering the four-momentum vectors of particle-flow candidates. The particle-flow algorithm combines information from all relevant CMS subdetectors to identify and reconstruct all visible particles in the event, namely muons, electrons, photons, charged hadrons, and neutral hadrons as discussed above. At CMS, an algorithm known as the anti-k_T jet clustering algorithm [11] is used for grouping particle-flow candidates to form jets. Charged particle-flow candidates from extraneous proton–proton interactions within the same or a nearby bunch crossing ("pileup") are removed from inputs to the jet clustering algorithm in order to reduce effects of pileup interactions [12]. The particle-flow candidate should be in a cone with $R < 0.4$ where R is defined as

$$R = \sqrt{\delta\eta^2 + \delta\phi^2}. \tag{6.5}$$

Here, $\delta\eta$ and $\delta\phi$ are the angles between the direction of the jet and its constituents. The jet's direction is defined as the direction of the sum of the momenta of all the particles that are included in the jet.

The jet energy is calibrated using a set of corrections [13, 14]: an offset correction accounting for neutral energy arising from pileup interactions in the area of the reconstructed jet; a relative correction that makes the jet energy response, i.e., the ratio of the reconstructed to the original jet energy, uniform in p_{T} and η; an

absolute correction that restores the average jet energy response to unity; and a residual correction applied to account for remaining differences between data and simulation.

6.8.6 b-Jets

The identification of jets originating from b quarks, or containing b quarks, is crucial both for searches for new physics and for the measurement of standard model processes. A variety of algorithms are used to select b-quark jets based on variables such as the impact parameter of charged particle tracks, properties of reconstructed secondary vertices from heavy hadron decays, and the presence or absence of a lepton in the jet, or a combination of methods [15]. Among them, the combined secondary vertex (CSV) algorithm is used for the analysis described in Chap. 7, which uses secondary vertices and track-based lifetime information to build a likelihood-based discriminator to distinguish between jets from b-quarks and those from charm or light quarks and gluons. With the specific requirement on this CSV discriminator chosen for the analysis, the efficiency of identifying b-quark jets is approximately 65% for jets originating from b quarks with momenta typical of top quark pair events.

6.8.7 Missing Transverse Energy

The magnitude of an imbalance in the transverse momentum of an event is stored as the event's missing transverse energy, $E_{\mathrm{T}}^{\mathrm{miss}}$. The transverse momentum of an event is equal to the vector sum of the momentum of the PF candidates in the event. The Lorentz symmetry in particle physics leads to the principle of conservation of momentum, according to which the vectorial sum of the transverse momentum of all the true particles in an event should be zero. In CMS events, however, we often see that the vector sum of the momentum of the reconstructed particles is not zero. This can be due to the mismeasurement of energy of jets or other particles in the event, or due to existence of some genuine particles like neutrinos or the stable lightest supersymmetric particles, which pass through the detectors without leaving any trace.

References

1. CMS Collaboration, JINST **3**, S08004 (2008)
2. P. Merkel, CMS Tracker Performance, CMS Conference Report CMS-CR-2012-102, CERN, Geneva, 2012

3. CMS Collaboration, JINST **9**, P10009 (2014) [arXiv:1405.6569]
4. A. Breskin, R. Voss, The CERN Large Hadron Collider: Accelerator and Experiments, CERN, Geneva, 2009
5. CMS Collaboration, The Electromagnetic Calorimeter Project - Technical Design Report, CERN/LHCC 97-33, 15 December 1997
6. CMS Collaboration, JINST **8** (2013) [arXiv:1306.2016]
7. CMS Collaboration, CMS Technical Design Report for the Level-1 Trigger Upgrade. No. CERN-LHCC-2013-011, CMS-TDR-12, CERN, 2013
8. W. Adam et al., The CMS high level trigger. Eur. Phys. J. C **46**, 605 (2006) [arXiv:hep-ex/0512077]
9. CMS Collaboration, Particle-Flow Event Reconstruction in CMS and Performance for Jets, Taus, and MET, CMS Physics Analysis Summary CMS-PAS-PFT-09-001, CERN, 2009
10. T. Speer, W. Adam, R. Frühwirth, A. Strandlie, T. Todorov, M. Winkler, Nucl. Instrum. Methods Phys. Res. Sect. A **559**, 1 (2006)
11. M. Cacciari, G.P. Salam, G. Soyez, JHEP **04**, 063 (2008)
12. CMS Collaboration, Pileup Removal Algorithms, CMS Physics Analysis Summary CMS-PAS-JME-14-001, CERN, 2014
13. CMS Collaboration, JINST **6**, 11002 (2011) [arXiv:1107.4277]
14. CMS Collaboration, JINST **12**, P02014 (2017) [arXiv:1607.03663]
15. CMS Collaboration, Performance of b tagging at $\sqrt{s} = 8\,\text{TeV}$ in multijet, ttbar and boosted topology events, CMS Physics Analysis Summary CMS-PAS-BTV-13-001, CERN, 2013

Chapter 7
Search for Supersymmetry in the Multijet and Missing Transverse Momentum Channel in pp Collisions at 13 TeV

This chapter published as: The CMS Collaboration, "Search for supersymmetry in the multijet and missing transverse momentum channel in pp collisions at 13 TeV," Phys. Lett. B 758 (2016) 152.

7.1 Introduction

As described in Chap. 4, supersymmetry is a well-motivated extension to the standard model. According to this theory, each particle in the standard model has a supersymmetric partner whose spin differs from the standard model particle by one-half unit. The naturalness principle suggests that the masses of the superparticles should be of the order of 1 TeV [1–3]; therefore, the superparticles should be within our reach at high energy colliders like the LHC at CERN. One of the supersymmetry signals with a relatively high cross section is the production of a pair of gluinos that decay to four or more hadronic jets in the final state. In this search, in addition to the above-mentioned assumptions, we also assume that R-parity is conserved with the consequence that the lightest SUSY particle is stable [4] and perhaps weakly interacting. Therefore, it leaves our detectors undetected, resulting in a huge amount of missing energy. As a result, one possible signal that we can search for is characterized by significant missing energy and a large number of jets.

The data used in this study [5] correspond to 2.3 fb^{-1} of proton–proton collisions at a center-of-mass energy of 13 TeV, collected by the CMS detector during Run 2 of the LHC. We mainly focus on gluino pair production scenarios denoted T1 and T5. In T1 scenarios, the two gluinos $\tilde{g}$ each decay to a pair of quarks and a stable superparticle, the LSP. In T5 scenarios both of the gluinos undergo a cascade decay. The scenarios are shown in Figs. 7.1 and 7.2 and are motivated in [6]. The LSP candidate in these scenarios is assumed to be the lightest neutralino, $\tilde{\chi}_1^0$, a combination of the superpartners of the Higgs boson and gauge bosons. We further

A. Borzou, *Theoretical and Experimental Approaches to Dark Energy and the Cosmological Constant Problem*, Springer Theses,
https://doi.org/10.1007/978-3-319-69632-4_7

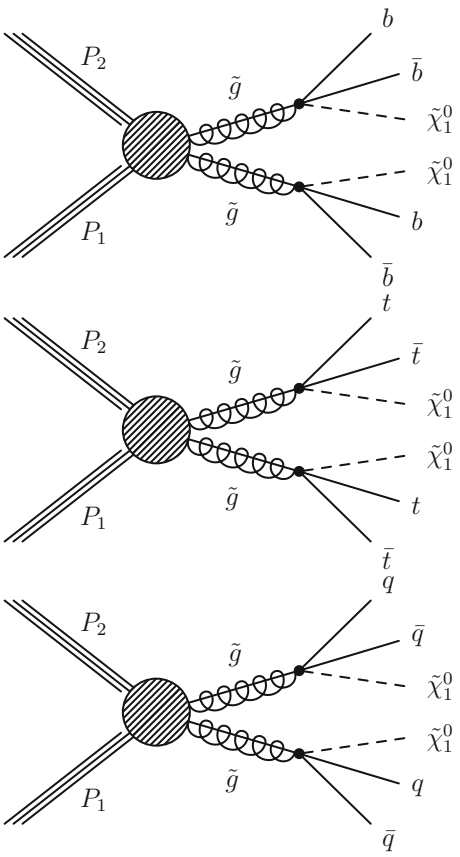

Fig. 7.1 Event diagrams for the new-physics scenarios considered in this study: (top) T1bbbb, (middle) T1tttt, (bottom) T1qqqq

assume that all other superparticles are heavy enough to be neglected. We expect at least four jets in each signal event, which results in a large amount of H_{T}, defined as the scalar sum of the transverse momentum of the jets. Generally, our search is for events that have large H_{T}, a large number of jets N_{jet}, and large $H_{\mathrm{T}}^{\text{miss}}$, which is defined as the magnitude of

$$\vec{H}_{\mathrm{T}}^{\text{miss}} = -\sum_{\text{jet}} \vec{p}_{\mathrm{T}} \tag{7.1}$$

and is a measure of the missing energy of the event. In addition, we count the number of tagged bottom quarks, $N_{\text{b-jet}}$. Therefore, we categorize the data using a total of four variables: N_{jet}, $N_{\text{b-jet}}$, H_{T}, and $H_{\mathrm{T}}^{\text{miss}}$.

There are several types of processes predicted by the standard model (SM) that can generate large missing energy in addition to large scalar sum of transverse momentum of jets, thereby mimicking the supersymmetry signals that we aim to search for. These are called the (SM) background of the analysis and need to

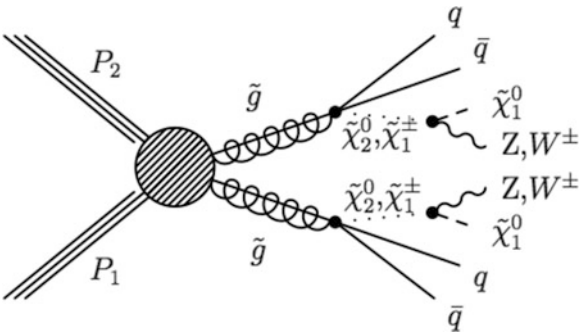

Fig. 7.2 SUSY T5qqqqVV simplified scenario considered in this study

be precisely predicted and subtracted from the total event yield in data. The first category of these backgrounds arises when a W boson decays to a neutrino and a lepton. The events that can lead to such a background are mainly top quark-antiquark pair production, single top production, and production of a W boson accompanied by jets. These events are suppressed by removing events with reconstructed electron and muon candidates; however, some events do not get rejected when the electrons and muons escape detection or τ leptons decay hadronically. Another type of background comes from Z + jets production events in which a Z boson decays to two neutrinos and therefore cannot be detected, leaving a large missing energy in the event. This category of background is often referred to as the invisible Z background. Most of QCD multijet events do not carry large missing energies. However, occasionally they result in large missing energies due to an imperfect measurement of the energy of their jets.

The study presented here [5] is mainly based on two of the CMS Run 1 analyses [7, 8] that utilized the $\sqrt{s} = 8\,\text{TeV}$ data. The combination of the two has proven to be more sensitive to a wide variety of supersymmetry signals.

7.2 Triggers

In this analysis events are collected using a trigger with two thresholds on H_T and E_T^miss. The trigger requires an online calorimeter-based $H_\text{T} > 280\,\text{GeV}$ and calorimeter-based $E_\text{T}^\text{miss} > 70\,\text{GeV}$. The efficiency of the trigger is estimated in terms of H_T and H_T^miss. For this purpose, we first choose events that have passed an independent trigger that has no H_T or H_T^miss threshold and therefore the H_T or H_T^miss of the events are solely categorized by our own trigger. These events are called the base sample. The fraction of the events in the base sample that are also triggered by our primary H_T–H_T^miss trigger is taken as the efficiency. Our studies show that the efficiency is greater than 98% for the search region as shown in Fig. 7.3.

The trigger that we use for the analysis, as described above, has a relatively high H_T^miss threshold and is not suitable for the purpose of estimating hadronically

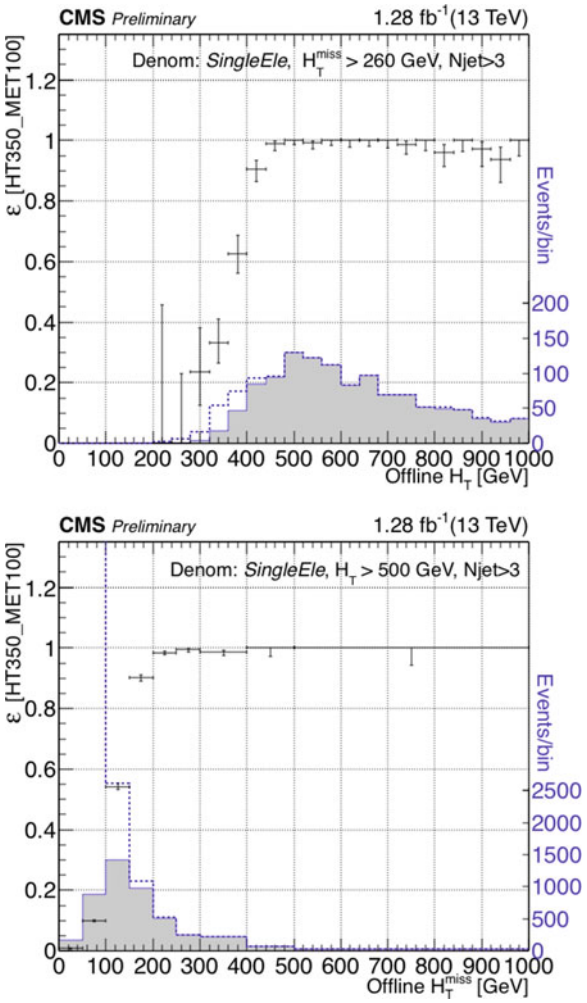

Fig. 7.3 The efficiency of our search trigger as a function of the search variables. For the efficiency as a function of H_T, a threshold on the H_T^{miss} of 260 GeV is applied to ensure full efficiency of the E_T^{miss} component of the trigger. For the efficiency as a function of H_T^{miss}, the baseline selection of $H_T > 500$ GeV is applied. The dashed (solid) blue lines show the distributions of the denominator (numerator) samples

decaying τ lepton and invisible Z backgrounds. The reason is that the two backgrounds are estimated based on a control sample that should in principle contain events with very low or no H_T^{miss}, as described in detail in Sects. 7.5.2 and 7.5.3.2. Therefore, for the sake of estimating the hadronically decaying τ lepton background, we employ a trigger that has only a threshold in H_T but also requires a muon with $p_T > 15$ GeV in the event. The efficiency of this trigger is measured in terms of H_T and muon transverse momentum p_T. As shown in Fig. 7.4, the efficiency is greater than 95% in the search region.

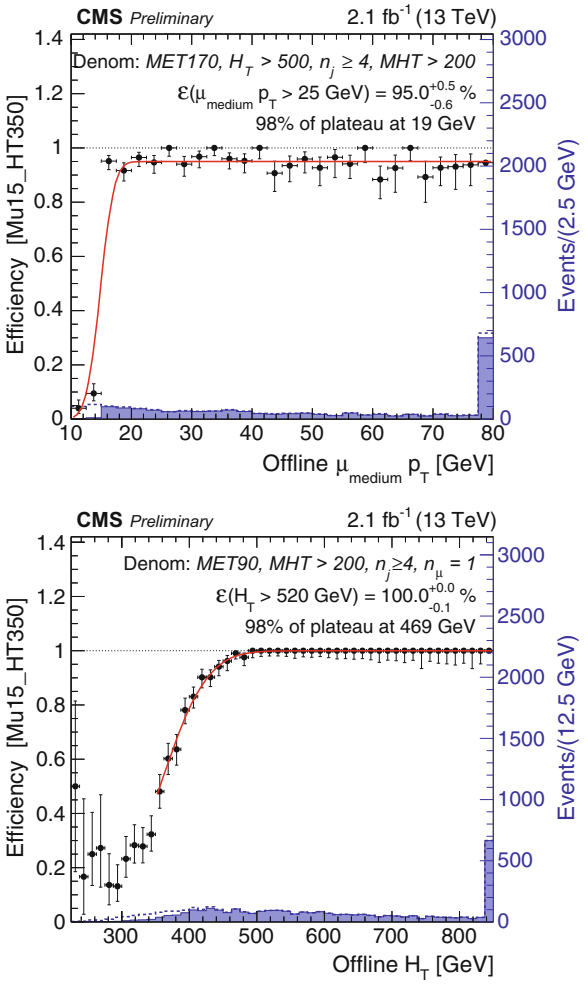

Fig. 7.4 Efficiency of the muon + H_T trigger as a function of H_T and muon p_T. This is the trigger employed to select the leptonic control sample for the hadronically decaying τ lepton background estimation

The same trigger that was used for collecting the hadronically decaying τ lepton background, together with its electron counterpart, is employed for estimating the invisible Z background. In this case, the trigger has a higher efficiency of 98–100% due to the existence of two electrons in the control sample, and either one of them can trigger the event. The method for estimating the Z invisible background in our analysis requires another photon control sample collected by triggering on $H_T > 500\,\text{GeV}$ as well as a photon candidate with $p_T > 90\,\text{GeV}$. Figure 7.5 shows the efficiency of this last trigger versus H_T and photon p_T, which is measured to be 96% for photon $p_T > 105\,\text{GeV}$.

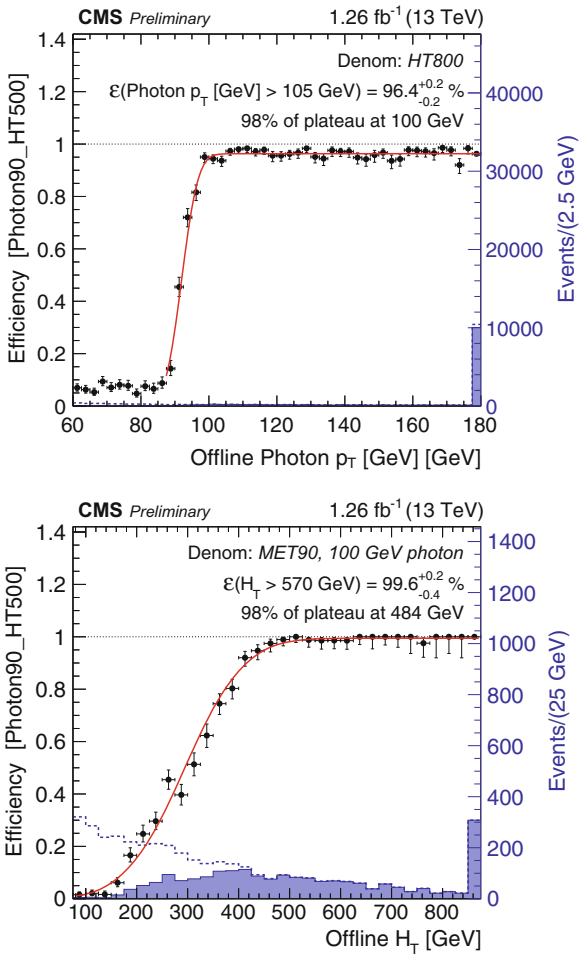

Fig. 7.5 Efficiency of the photon + H_T trigger as a function of H_T and photon p_T employed to select the control sample for the invisible Z background estimation

7.3 Event Selection and Search Regions

The following requirements define the selection criteria for signal event candidates:

- $N_{\text{jet}} \geq 4$, where the jets must satisfy $p_T > 30\,\text{GeV}$ and $|\eta| < 2.4$; we require at least four jets because of our focus on gluino pair production;
- $H_T > 500\,\text{GeV}$, where H_T is the scalar p_T sum of jets with $|\eta| < 2.4$;
- $H_T^{\text{miss}} > 200\,\text{GeV}$, where H_T^{miss} is the magnitude of the vector p_T sum of jets with $|\eta| < 5$; the η range is extended in this case to improve the E_T^{miss} measurement;
- no identified isolated electron or muon candidate with $p_T > 10\,\text{GeV}$; electron candidates are restricted to $|\eta| < 2.5$ and muon candidates to $|\eta| < 2.4$; muon

candidates must have a distance of closest approach to the primary vertex less than 0.5 mm in the direction along the beam axis and 0.2 mm in the transverse plane;
- no isolated charged-particle track with $|\eta| < 2.4$, $m_{\mathrm{T}} < 100\,\mathrm{GeV}$, and $p_{\mathrm{T}} > 10\,\mathrm{GeV}$ ($p_{\mathrm{T}} > 5\,\mathrm{GeV}$ if the track is identified as an electron or muon candidate by the PF algorithm), where m_{T} is the transverse mass [9] formed from the $E_{\mathrm{T}}^{\mathrm{miss}}$ and isolated-track p_{T} vectors, with $E_{\mathrm{T}}^{\mathrm{miss}}$ defined by the projection onto the transverse plane of the negative of the vector sum of all PF candidates;
- $\Delta\phi_{H_{\mathrm{T}}^{\mathrm{miss}},j_i} > 0.5$ (>0.3) for the two highest p_{T} jets j_1 and j_2 (the next two highest p_{T} jets j_3 and j_4), with $\Delta\phi_{H_{\mathrm{T}}^{\mathrm{miss}},j_i}$ the angle between the $H_{\mathrm{T}}^{\mathrm{miss}}$ vector and the p_{T} vector of jet j_i.

In the above event selection, only isolated leptons are considered because leptons from $\mathrm{W} \to \ell\nu$ decays, which we would like to veto, tend to be isolated from other hadrons in the same events unlike leptons coming from heavy flavor quark decays. The lepton isolation I in this analysis is defined as the scalar sum of the transverse momenta of all neutral and charged PF candidates within a cone $\Delta R = \sqrt{(\Delta\eta)^2 + (\Delta\phi)^2}$ divided by the lepton p_{T}, where the cone size varies from 0.05 to 0.2 depending on the lepton p_{T} [10]. Muons and electrons are considered to be isolated when the isolation variable I is less than 0.2 and 0.1, respectively.

The isolated-track veto requirement eliminates events with hadronically decaying τ leptons as well as isolated electrons or muons in cases when the lepton is not identified; the m_{T} requirement restricts this veto to tracks consistent with W boson decay in order to minimize the impact on signal efficiency and is defined as

$$m_{\mathrm{T}}(\mathrm{tk}, E_{\mathrm{T}}^{\mathrm{miss}}) = \sqrt{2{p_{\mathrm{T}}}^{\mathrm{tk}} E_{\mathrm{T}}^{\mathrm{miss}}(1 - \cos\Delta\phi)}, \tag{7.2}$$

where ${p_{\mathrm{T}}}^{\mathrm{tk}}$ is the transverse momentum of the track and $\Delta\phi$ is the azimuthal separation between the track and $\vec{p}_{\mathrm{T}}^{\,\mathrm{miss}}$. The $\Delta\phi_{H_{\mathrm{T}}^{\mathrm{miss}},j_i}$ requirements reduce the background from QCD multijet processes in which $E_{\mathrm{T}}^{\mathrm{miss}}$ is usually aligned along a jet direction.

The search is performed in the following exclusive intervals of the four search variables:

- N_{jet}: 4–6, 7–8, ≥9;
- $N_{\mathrm{b\text{-}jet}}$: 0, 1, 2, ≥3;
- H_{T}: 500–800, 800–1200, ≥1200 GeV;
- $H_{\mathrm{T}}^{\mathrm{miss}}$: 200–500, 500–750, ≥750 GeV.

The bins with $H_{\mathrm{T}} < 800\,\mathrm{GeV}$ and $H_{\mathrm{T}}^{\mathrm{miss}} > 750\,\mathrm{GeV}$ are discarded because $H_{\mathrm{T}}^{\mathrm{miss}}$ cannot exceed H_{T} in a physical event. Additionally, for $500 < H_{\mathrm{T}}^{\mathrm{miss}} < 750\,\mathrm{GeV}$, an expanded interval $500 < H_{\mathrm{T}} < 1200\,\mathrm{GeV}$ is used, and for $H_{\mathrm{T}}^{\mathrm{miss}} > 750\,\mathrm{GeV}$ a single interval $H_{\mathrm{T}} > 800\,\mathrm{GeV}$ is used, because of the low expected number of events at large $H_{\mathrm{T}}^{\mathrm{miss}}$. The six search intervals in the $H_{\mathrm{T}}^{\mathrm{miss}}$ versus H_{T} plane are illustrated schematically in Fig. 7.6. The total number of search regions is 72.

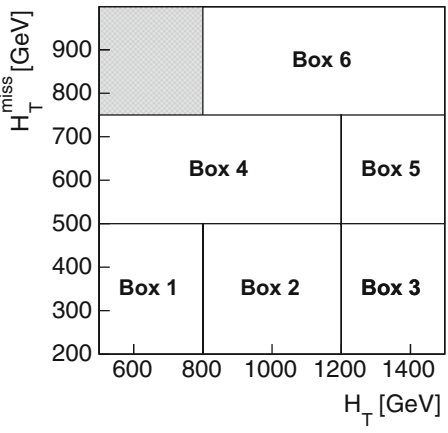

Fig. 7.6 Schematic illustration of the search intervals in the H_T^{miss} versus H_T plane. Each of the six H_T and H_T^{miss} intervals is examined as a function of three N_{jet} bins and four $N_{b\text{-}jet}$ bins for a total of 72 search regions

7.4 Event Simulation

The background is mostly evaluated using data control regions, as described below (Sect. 7.5). Simulated samples of SM events are used to construct and validate the procedures and to estimate a few of the smaller background components. The MADGRAPH5_aMC@NLO [11] event generator at leading order is used to simulate $t\bar{t}$, W + jets, Z + jets, γ + jets, and QCD multijet events. Single-top events in the t and tW channels are described using the POWHEG v1.0 [12–16] program, and in the s channel using the MADGRAPH5_aMC@NLO [11] program at next-to-leading (NLO) order. The latter generator is also used to simulate events with dibosons (WW, ZZ, WH production, etc., where H stands for a Higgs boson) and rare processes ($t\bar{t}W$, $t\bar{t}Z$, WWZ combinations, etc.), except that POWHEG [17] is used for WW events in which both W bosons decay leptonically. Simulation of the detector response is based on the GEANT4 [18] package. The simulated samples are normalized using the most accurate cross section calculations currently available [19–30], generally with NLO or next-to-NLO accuracy.

The signal events for T1bbbb, T1tttt, T1qqqq, and T5qqqqVV are generated for a range of gluino $m_{\tilde{g}}$ and LSP $m_{\tilde{\chi}_1^0}$ mass values, with $m_{\tilde{\chi}_1^0} < m_{\tilde{g}}$. For the T5qqqqVV model, the masses of the intermediate $\tilde{\chi}_2^0$ and $\tilde{\chi}_2^{\pm}$ states are taken to be the mean of $m_{\tilde{\chi}_1^0}$ and $m_{\tilde{g}}$. The signal samples are generated with the MADGRAPH5_aMC@NLO program at leading order, with up to two partons present in addition to the gluino pair. The decays of the gluino are described with a pure phase-space matrix element [31]. The signal production cross sections are computed [32–36] with NLO plus next-to-leading-logarithm (NLL) accuracy. To reduce computational requirements, the detector is modeled with the CMS fast simulation program [37, 38], which yields consistent results compared with the GEANT4-based simulation, except that we apply a correction of 1% to account for differences in the efficiency of the jet quality requirements [39], and corrections of 3–10% to account for differences in the b-jet tagging efficiency.

Table 7.1 Summary of systematic uncertainties that affect the signal event selection efficiency

Item	Uncertainty (%)
Trigger efficiency	0.5–1.1
Pileup reweighting	0.1–0.5
Jet quality requirements	1.0
Renormalization and factorization scales	0.1–3.0
Initial-state radiation	0.02–10.0
Jet energy scale	0.5–4.0
Isolated lepton and track vetoes (T1tttt and T5qqqqVV only)	2.0
Total	1.5–11.0

The results are averaged over all search regions. The variations correspond to different signal models and choices of the gluino and LSP masses

The NNPDF3.0LO [40] parton distribution functions (PDF) are used for the simulated samples generated at leading order, and the NNPDF3.0NLO [40] PDFs for the samples generated at NLO. All simulated samples use the PYTHIA 8.2 [31] program to describe parton showering and hadronization. To model the effects of extraneous proton–proton interactions (pileup), the simulated events are generated with a nominal distribution of pp interactions per bunch crossing and then reweighted to match the corresponding distribution in data. We evaluate systematic uncertainties in the signal model predictions. Those that are relevant for the selection efficiency are listed in Table 7.1. The uncertainty associated with the renormalization and factorization scales is determined by varying each scale independently by factors of 2.0 and 0.5 [41, 42]. An uncertainty related to the modeling of initial-state radiation (ISR) is determined by comparing the simulated and measured p_{T} spectra of the system recoiling against the ISR jets in $\mathrm{t\bar{t}}$ events, using the technique described in [43]. The two spectra are observed to agree. The uncertainties associated with the renormalization and factorization scales, and with ISR, integrated over all search regions, typically lie below 0.1% but can be as large as 1–3% and 3–10%, respectively, for $m_{\tilde{\chi}_1^0} \sim m_{\tilde{g}}$. The uncertainty associated with the jet energy scale is evaluated as a function of jet p_{T} and η. Note that the isolated lepton and track vetoes do not affect the T1bbbb and T1qqqq samples since events in these samples rarely contain an isolated charged track.

The sources of systematic uncertainty associated with the trigger efficiency, pileup reweighting, renormalization and factorization scales, ISR, and jet energy scale can also affect the shapes of the signal distributions, i.e., cause a migration of events between signal regions.

Systematic uncertainties are also evaluated in the signal predictions related to the b-jet tagging and misidentification efficiencies and to the statistical uncertainties in the signal event samples. Systematic uncertainties associated with PDFs are evaluated [44–46] following the recommendations of [47, 48] and are applied to the normalization of the signal event cross sections. The systematic uncertainty in the determination of the integrated luminosity is 4.6%.

7.5 Background Evaluation

7.5.1 Background from QCD Multijet Events

Most of the time, the background from QCD multijet events arises due to mismeasurement of the energy of jets in the events. As a result, the direction of the $H_{\mathrm{T}}^{\mathrm{miss}}$, which is not genuine, is usually close to a jet. To evaluate the background associated with QCD multijet production, we select a QCD-dominated CR, called the low-$\Delta\phi$ region, by inverting the $\Delta\phi_{H_{\mathrm{T}}^{\mathrm{miss}},j_i}$ requirements described in Sect. 7.3, i.e., by requiring at least one of the four highest p_{T} jets in an event to fail the respective $\Delta\phi_{H_{\mathrm{T}}^{\mathrm{miss}},j_i}$ selection criterion. The QCD background in each search region is given by the product of the observed event yield in the corresponding region of the low-$\Delta\phi$ CR multiplied by a factor R^{QCD}. This ratio is defined as the amount of the expected QCD multijet background in the signal region divided by the amount of the expected QCD multijet background in the low-$\Delta\phi$ region, after subtracting the contributions from non-QCD standard model processes. The non-QCD standard model contributions to the low-$\Delta\phi$ CR, which correspond to around 14% of the events in this CR, are evaluated using techniques that are described in this section for the top quark, W + jets, and Z + jets backgrounds, but with the inverted $\Delta\phi_{H_{\mathrm{T}}^{\mathrm{miss}},j_i}$ requirements. The R^{QCD} terms are determined primarily from data, as described below. The R^{QCD} factor increases with N_{jet} but is empirically found to have only a small dependence on $N_{\text{b-jet}}$ for a given N_{jet} value. We therefore divide the $4 \leq N_{\mathrm{jet}} \leq 6$ search region into three exclusive bins: $N_{\mathrm{jet}} = 4$, 5, and 6. Once this is done, there is no dependence of R^{QCD} on $N_{\text{b-jet}}$. Similarly, we divide the $200 \leq H_{\mathrm{T}}^{\mathrm{miss}} \leq 500\,\mathrm{GeV}$ search region into two bins: $200 < H_{\mathrm{T}}^{\mathrm{miss}} < 300\,\mathrm{GeV}$ and $300 < H_{\mathrm{T}}^{\mathrm{miss}} < 500\,\mathrm{GeV}$. The first of these bins ($200 < H_{\mathrm{T}}^{\mathrm{miss}} < 300\,\mathrm{GeV}$) is enhanced in QCD background events, both in the low-$\Delta\phi$ and signal regions. The H_{T}, $H_{\mathrm{T}}^{\mathrm{miss}}$, and N_{jet} dependence of R^{QCD} is modeled as:

$$R^{\mathrm{QCD}}_{i,j,k} = K_{H_{\mathrm{T}},i} S_{H_{\mathrm{T}}^{\mathrm{miss}},j} S_{N_{\mathrm{jet}},k}, \tag{7.3}$$

where i, j, and k are bin indices. The $K_{H_{\mathrm{T}},i}$ term is the ratio of the expected number of QCD multijet events in the signal region to that in the low-$\Delta\phi$ region for H_{T} bin i in the first $H_{\mathrm{T}}^{\mathrm{miss}}$ and N_{jet} bins. The $S_{H_{\mathrm{T}}^{\mathrm{miss}},j}$ term represents a correction for $H_{\mathrm{T}}^{\mathrm{miss}}$ bin j with respect to the first $H_{\mathrm{T}}^{\mathrm{miss}}$ bin, and the $S_{N_{\mathrm{jet}},k}$ term a correction for N_{jet} bin k with respect to the first N_{jet} bin. The $K_{H_{\mathrm{T}},i}$ and $S_{N_{\mathrm{jet}},k}$ terms are determined from a fit to data in the $200 < H_{\mathrm{T}}^{\mathrm{miss}} < 300\,\mathrm{GeV}$ bin, with the non-QCD SM background taken into account. The $S_{H_{\mathrm{T}}^{\mathrm{miss}},j}$ terms are taken from the QCD multijet simulation. Based on studies of the different contributions of events in which the jet with the largest p_{T} mismeasurement is or is not among the four highest p_{T} jets, uncertainties of 50, 100, and 100% are assigned to the $300 < H_{\mathrm{T}}^{\mathrm{miss}} < 500\,\mathrm{GeV}$, $500 < H_{\mathrm{T}}^{\mathrm{miss}} < 750\,\mathrm{GeV}$, and $H_{\mathrm{T}}^{\mathrm{miss}} \geq 750\,\mathrm{GeV}$ bins, respectively, to account for potential differences between data and simulation in the $S_{H_{\mathrm{T}}^{\mathrm{miss}},j}$ factors.

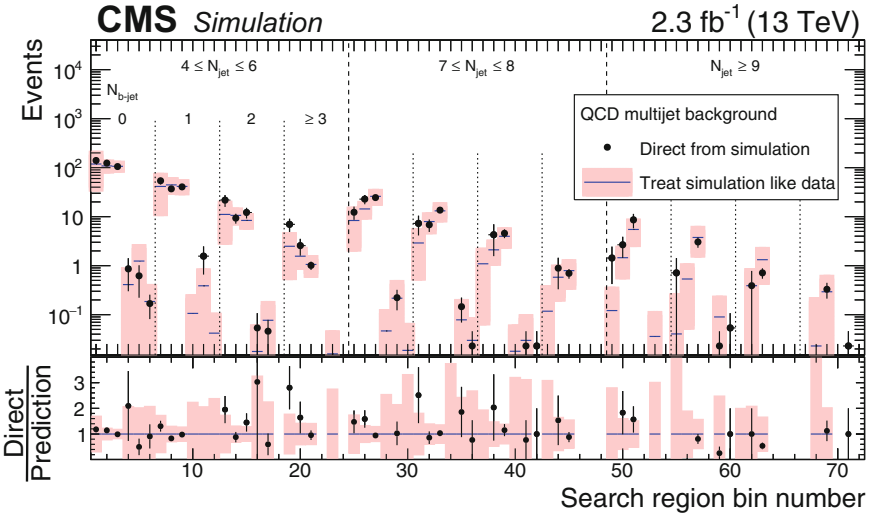

Fig. 7.7 The QCD multijet background in the 72 search regions of the analysis as predicted directly from QCD multijet simulation (points, with statistical uncertainties) and as predicted by applying the QCD multijet background determination procedure to simulated event samples (histograms, with statistical and systematic uncertainties added in quadrature). The lower panel shows the same results following division by the predicted value. The six results within each region delineated by dashed lines correspond sequentially to the six regions of H_{T} and $H_{\mathrm{T}}^{\mathrm{miss}}$ indicated in Fig. 7.6

To validate the performance of the method, the QCD multijet background expectation, based on the generator level truth information in a set of simulated events, is compared with the background prediction by applying the method to the same simulated events. This procedure is called a closure test and is presented in Fig. 7.7, where it is shown that the expectation directly from simulation and the prediction of the method, applied to the same simulated events, are consistent.

For the lowest $H_{\mathrm{T}}^{\mathrm{miss}}$ search region, the uncertainty in the prediction of the QCD multijet background is dominated by the uncertainties in $K_{H_{\mathrm{T}},i}$ and $S_{N_{\mathrm{jet}},k}$, which themselves are mostly due to uncertainties in the non-QCD SM background in the signal regions. For the two higher $H_{\mathrm{T}}^{\mathrm{miss}}$ search regions, the uncertainty in $S_{H_{\mathrm{T}}^{\mathrm{miss}},j}$ and the limited statistical precision of the low-$\Delta\phi$ CR dominate the uncertainty. The uncertainties related to potential nonclosure (Fig. 7.7) are either small in comparison or statistical in nature and are not considered.

7.5.2 *Background from $Z(\rightarrow \nu\bar{\nu})$ Events*

Another important background in this search is the invisible Z background. In this type of event, a Z boson decays to two neutrinos and therefore introduces

a genuine $H_{\mathrm{T}}^{\mathrm{miss}}$. A simple method to estimate the invisible Z background is to start with Z + jets events that consist of $\mathrm{Z}(\to \ell^+\ell^-)$ ($\ell = e, \mu$) and, except for the lepton and isolated track vetoes, pass the event selection criteria of Sect. 7.3. Next, one needs to use the fact that the ratio of branching fractions of Z, decays $\mathcal{B}(\mathrm{Z}(\to \ell^+\ell^-))/\mathcal{B}(\mathrm{Z}(\to \nu\bar{\nu}))$, is a constant and it is not correlated with associated jet production. Therefore, one can remove the ℓ^+ and ℓ^- to emulate the $\mathrm{Z}(\to \nu\bar{\nu})$ process. The resulting efficiency-corrected event yields can be directly translated into a prediction for the $\mathrm{Z}(\to \nu\bar{\nu})$ background through multiplication by the known ratio of branching fractions [49]. An obstruction of this procedure is that the $\mathrm{Z}(\to \ell^+\ell^-)$ branching fraction is only around 10% of the total branching fraction.

An alternative approach is to utilize the similarity between Z boson and photon radiation. Knowing events that contain a photon and pass the selection criteria of Sect. 7.3, the ratio $N(\mathrm{Z}(\to \nu\bar{\nu}))/N(\gamma)$ can be used to evaluate the invisible Z background by removing the photon from the event and replacing it with a Z boson decaying to two neutrinos. The γ + jets process differs from the Z + jets process because of threshold effects associated with the Z boson mass and because of the different couplings of Z bosons and photons to up- and down-type quarks. These differences are generally well understood [50–53] and described adequately with simulation.

The estimation of the $\mathrm{Z}(\to \nu\bar{\nu})$ background employs both approaches described above. Fits as described in [7, 8] are used to extract the prompt-photon and Z boson yields, respectively. Because of current limitations in the simulations for the theoretical modeling of γ + jets versus Z + jets production with heavy flavor jets, we restrict the use of γ + jets events to the 18 search regions with $N_{\text{b-jet}} = 0$. The $\mathrm{Z}(\to \ell^+\ell^-)$ sample, integrated over H_{T} and $H_{\mathrm{T}}^{\mathrm{miss}}$, because of the limited statistical precision, is used to extrapolate the $N_{\text{b-jet}} = 0$ results to the $N_{\text{b-jet}} > 0$ search regions.

The following equation is used in order to evaluate the invisible Z background in the search regions with $N_{\text{b-jet}} = 0$, the number $N^{\mathrm{pred}}_{\mathrm{Z}(\to\nu\bar{\nu})}$ of $\mathrm{Z}(\to \nu\bar{\nu})$ + jets events, from the number $N_{\gamma}^{\mathrm{data}}$ of events in the corresponding N_{jet}, H_{T}, and $H_{\mathrm{T}}^{\mathrm{miss}}$ bin of the γ + jets CR:

$$N^{\mathrm{pred}}_{\mathrm{Z}(\to\nu\bar{\nu})}\Big|_{N_{\text{b-jet}}=0} = \rho\mathcal{R}_{\mathrm{Z}(\to\nu\bar{\nu})}\beta_{\gamma}N_{\gamma}^{\mathrm{data}}, \tag{7.4}$$

where $\mathcal{R}_{\mathrm{Z}(\to\nu\bar{\nu})}$ is the ratio of the numbers of $\mathrm{Z}(\to \nu\bar{\nu})$ + jets events to γ + jets events from simulation. The γ + jets term is obtained from a MADGRAPH5_aMC@NLO calculation at leading order. Also, β_{γ} is the purity of the CR and is defined as the fraction of all photons that are prompt

$$\beta_{\gamma} = \frac{N_{\text{prompt}}}{N_{\text{prompt}} + N_{\text{non-prompt}}}, \tag{7.5}$$

with prompt photons being defined as those that are radiated from a quark while non-prompt photons are the decay products of mesons. The factor ρ [8] in Eq. (7.4), defined as

$$\rho = \frac{\mathcal{R}^{\text{data}}_{\text{Z}(\to\ell^+\ell^-)/\gamma}}{\mathcal{R}^{\text{sim}}_{\text{Z}(\to\ell^+\ell^-)/\gamma}} = \frac{N^{\text{data}}_{\text{Z}(\to\ell^+\ell^-)}}{N^{\text{data}}_{\gamma}} \frac{N^{\text{sim}}_{\gamma}}{N^{\text{sim}}_{\text{Z}(\to\ell^+\ell^-)}}, \tag{7.6}$$

uses the $\text{Z}(\to \ell^+\ell^-)$ CR to account for potential differences in $\mathcal{R}_{\text{Z}(\to\nu\bar{\nu})}$ between simulation and data, such as those expected due to missing higher-order terms in the γ + jets calculation, and is found to have a value of 0.92 (taken to be constant). The uncertainties are deduced from linear fits to projections onto each dimension, and they vary with N_{jet}, H_{T}, and $H^{\text{miss}}_{\text{T}}$ between 8 and 60%.

For search regions with $N_{\text{b-jet}} > 0$, the $\text{Z}(\to \nu\bar{\nu})$ background estimate is

$$\left(N^{\text{pred}}_{\text{Z}(\to\nu\bar{\nu})}\right)_{j,b,k} = \left(N^{\text{pred}}_{\text{Z}(\to\nu\bar{\nu})}\right)_{j,0,k} \mathcal{F}_{j,b}; \tag{7.7}$$

$$\mathcal{F}_{j,b} = \left(N^{\text{data}}_{\text{Z}(\to\ell^+\ell^-)}\beta_{\ell\ell}\right)_{0,b} / \left(N^{\text{data}}_{\text{Z}(\to\ell^+\ell^-)}\beta_{\ell\ell}\right)_{0,0} \mathcal{J}_{j,b}; \tag{7.8}$$

$$\mathcal{J}_{j,b} = N^{\text{model}}_{j,b}/N^{\text{model}}_{0,b}. \tag{7.9}$$

The first term on the right-hand side of Eq. (7.7) is obtained from Eq. (7.4) where j, b, and k are bin indices (numbered from zero) for the N_{jet}, $N_{\text{b-jet}}$, and kinematic (i.e., H_{T} and $H^{\text{miss}}_{\text{T}}$) variables, respectively. The $N_{\text{b-jet}}$ extrapolation factor $\mathcal{F}$ [Eq. (7.8)] is obtained from the fitted $\text{Z}(\to \ell^+\ell^-)$ yields, with data-derived corrections $\beta_{\ell\ell}$ to account for the $N_{\text{b-jet}}$-dependent purity. The dependence of the $N_{\text{b-jet}}$ shape of $\mathcal{F}$ on N_{jet} is described with the factor $\mathcal{J}$ [Eq. (7.9)], which is determined using a model estimate because of the limited statistical precision of the $\text{Z}(\to \ell^+\ell^-)$ data. The model uses the results of the $\text{Z}(\to \ell^+\ell^-)$ simulation for the central value of $\mathcal{J}$. Corresponding upper and lower bounds are determined, based on simulation studies, to define a systematic uncertainty in $\mathcal{J}$ that ranges from a few percent up to 60%, depending on N_{jet} and $N_{\text{b-jet}}$.

In Fig. 7.8 a closure test of the method is presented where the shaded bands represent the systematic uncertainty (10–20%, depending on $N_{\text{b-jet}}$) arising from the treatment of $\mathcal{F}$ as independent of the kinematic parameters, combined with the statistical uncertainty of the $\text{Z}(\to \ell^+\ell^-)$ + jets simulation. Moreover, systematic uncertainties associated with the statistical precision of the simulation, the photon reconstruction efficiency, the photon and dilepton purities, and the $\rho\mathcal{R}_{\text{Z}(\to\nu\bar{\nu})}$ term are evaluated. Of these, the $\rho\mathcal{R}_{\text{Z}(\to\nu\bar{\nu})}$ term (10–60%) dominates the overall uncertainty except in the highest (N_{jet}, $N_{\text{b-jet}}$) search regions where the overall uncertainty is dominated by the statistical precision of the simulation (70–110%) and by the uncertainty in the $\text{Z}(\to \ell^+\ell^-)$ purity (40%). The underlying source of the leading systematic uncertainties is the limited number of events in the CR.

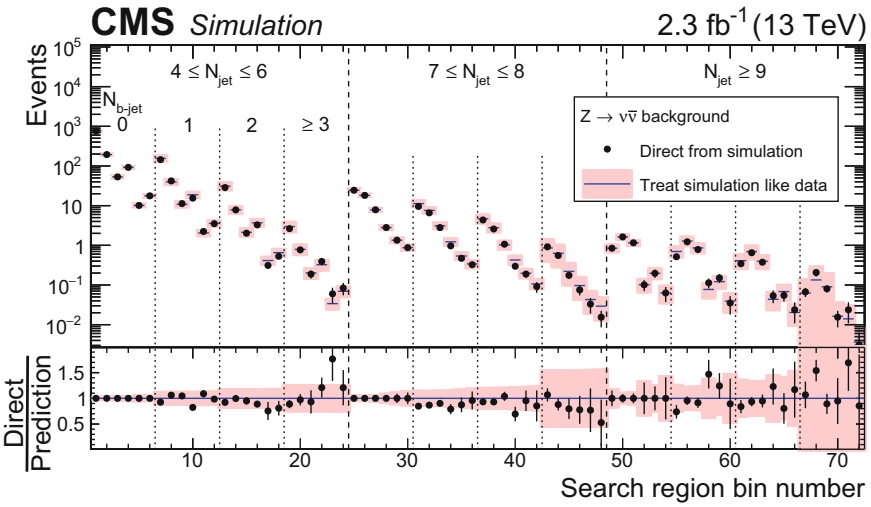

Fig. 7.8 The $Z(\rightarrow \nu\bar{\nu})$ background in the 72 search regions of the analysis as predicted directly from $Z(\rightarrow \nu\bar{\nu})$ + jets and $t\bar{t}Z$ simulation (points), and as predicted by applying the $Z(\rightarrow \nu\bar{\nu})$ background determination procedure to statistically independent $Z(\rightarrow \ell^+\ell^-)$ + jets simulated event samples (histogram). For bins corresponding to $N_{\text{b-jet}} = 0$, the agreement is exact by construction. The lower panel shows the ratio between the true and predicted yields. For both the upper and lower panels, the shaded regions indicate the quadrature sum of the systematic uncertainty associated with the dependence of $\mathcal{F}$ on the kinematic parameters (H_{T} and $H_{\text{T}}^{\text{miss}}$) and the statistical uncertainty of the simulated sample. The labeling of the search regions is the same as in Fig. 7.7

7.5.3 Background from Top Quark and W + Jets Events

One of the major backgrounds in this analysis arises when a W boson that can be found mostly in $t\bar{t}$, W + jets, or even single top events, decays to a lepton that is not identified and a neutrino that leaves a genuine $H_{\text{T}}^{\text{miss}}$. The lepton can be a τ that has decayed hadronically and therefore is hard to identify, or it can be an electron or muon that is lost for some reason. The former is referred to as the hadronic-τ background, while the latter is called the lost-lepton background. The approach for estimating the backgrounds is explained in the following subsections.

7.5.3.1 Lost-Lepton Background

The lost-lepton background can arise if an electron or muon lies outside the analysis acceptance, is not isolated, or is not reconstructed. The lost-lepton background is evaluated following the procedures established in [8, 54, 55]. Briefly, single-lepton control regions (CRs) are selected by inverting the electron and muon vetoes.

Each CR event is entered into one of the 72 search regions with a weight that represents the probability for a lost-lepton event to appear with the corresponding values of H_T, H_T^{miss}, N_{jet}, and $N_{b\text{-}jet}$.

The CRs are selected by requiring events to satisfy the criteria of Sect. 7.3 except that exactly one isolated electron or muon must be present and the isolated-track veto is not applied. The transverse mass formed from the E_T^{miss} and lepton p_T vector is required to satisfy $m_T < 100\,GeV$. The weights, accounting for the probability for a lepton to be "lost," are determined from the $t\bar{t}$, W + jets, single top quark, and rare process simulations through evaluation of the efficiency of the acceptance, reconstruction, and isolation requirements as a function of H_T, H_T^{miss}, N_{jet}, lepton p_T, and other kinematic variables. Corrections are applied to the weights to account for the trigger efficiency, contamination due to non-prompt electrons, contamination due to dilepton events in which one of the leptons is lost, and the selection efficiency of the m_T requirement. Corresponding efficiencies are evaluated for dileptonic events in which both leptons are lost. This latter source of background is predicted to account for <2% of the total lost-lepton background. Finally, a correction is applied to account for the selection efficiency of the isolated-track veto discussed in Sect. 7.3.

The weighted distributions of the search variables, summed over the events in the CRs, define the lost-lepton background prediction. The procedure is performed separately for single-electron and single-muon events. The two independent predictions yield consistent results and are averaged to obtain the final lost-lepton background prediction. The method is validated with a closure test, namely by determining the ability of the method, applied to simulated samples, to predict correctly the true number of background events. The results of the closure test are shown in Fig. 7.9.

The dominant uncertainties in the lost-lepton background prediction are statistical uncertainties due to the limited number of CR events in the most sensitive search regions. As a systematic uncertainty, we take the larger of the observed nonclosure in Fig. 7.9 or the statistical uncertainty in the nonclosure, for each search region, where "nonclosure" refers to the difference between the solid points and histogram. Additional systematic uncertainties are assigned based on a comparison between data and simulation of the lepton reconstruction, lepton isolation, and isolated track veto efficiencies. Within the statistical precision, there are no such differences observed, and the statistical uncertainty in the respective comparison is assigned as a systematic uncertainty. Uncertainties in the acceptance associated with the PDFs, including those related to the renormalization and factorization scales, are evaluated by varying the PDF sets used to produce the simulated samples. These uncertainties are defined by the maximum deviations observed from 100 variations of the NNPDF3.0LO PDFs for $t\bar{t}$ and W + jets events. The uncertainty in the jet energy correction is propagated to E_T^{miss}, and the resulting change in the m_T selection efficiency is used to define a systematic uncertainty. Small systematic uncertainties related to the purity of the electron and muon CRs and to the statistical uncertainties in the simulated efficiencies are also evaluated.

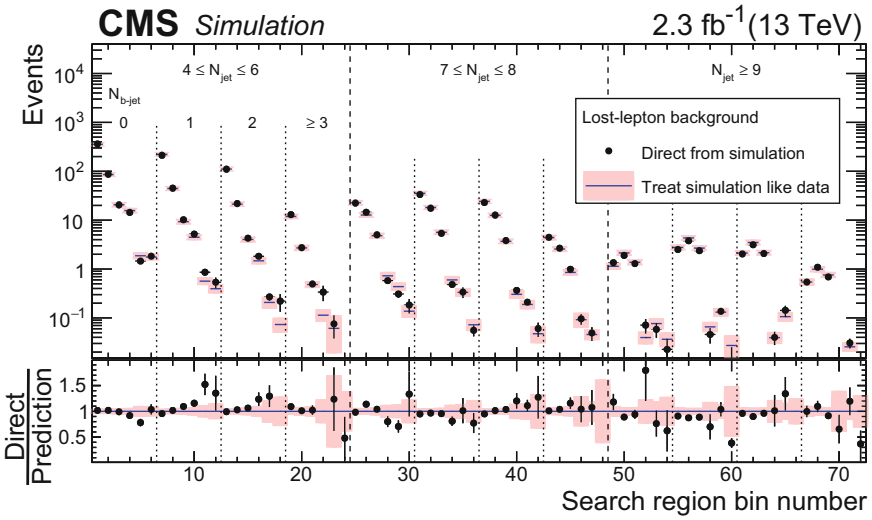

Fig. 7.9 The lost-lepton background in the 72 search regions of the analysis as predicted directly from $t\bar{t}$, single top quark, W + jets, diboson, and rare-event simulation (points, with statistical uncertainties) and as predicted by applying the lost-lepton background determination procedure to simulated electron and muon control samples (histograms, with statistical uncertainties). The lower panel shows the same results following division by the predicted value. The six results within each region delineated by dashed lines correspond sequentially to the six regions of H_T and H_T^{miss} indicated in Fig. 7.6

7.5.3.2 Hadronically Decaying τ Lepton Background

The $t\bar{t}$, single-top, and W + jets background events with $W \to \tau\nu_\tau$ decays are major backgrounds of this search. The τ lepton is the heaviest lepton, and it is the only lepton that decays to hadrons as well as to lighter leptons as shown in Table 7.2. Events with τ decaying to lighter leptons are suppressed by vetoes on electrons and muons, and residual events are considered as a part of the lost-lepton background discussed above. When τ leptons decay hadronically, they typically decay into either one charged hadron (1-prong decays) or three charged hadrons (3-prong decays) with up to two neutral pions (π^0) and one neutrino (ν_τ). The isolated track veto reduces about 40% of hadronically decaying τ (τ_h) background events, mostly those with 1-prong τ decays; however, residual events still constitute one of the most major backgrounds of this search. The estimation of this critical background is the author's most significant contribution to this search and it is discussed in detail below.

In order to estimate this τ_h background, the tau-template method is employed [8, 54, 55]. In this approach, the τ_h background is estimated from a control sample (CS) of μ + jets events, which we select by requiring exactly one muon with $p_T > 20$ GeV and $|\eta| < 2.1$. This single-muon CS is mainly composed of $W(\to \mu\nu)$ + jets events from W or top quark production. Since μ + jets and τ_h + jets production both arise

Table 7.2 Approximate branching fractions of different τ lepton decay modes [49]

Decay mode	$\mathcal{B}$ (%)
$\tau^- \to e^- \bar{\nu}_e \nu_\tau$	17.8
$\tau^- \to \mu^- \bar{\nu}_\mu \nu_\tau$	17.4
$\tau^- \to h^- \nu_\tau$	11.5
$\tau^- \to h^- \pi^0 \nu_\tau$	26.0
$\tau^- \to h^- \pi^0 \pi^0 \nu_\tau$	10.8
$\tau^- \to h^- h^+ h^- \nu_\tau$	9.8
$\tau^- \to h^- h^+ h^- \pi^0 \nu_\tau$	4.8
Other hadronic modes	1.8
All hadronic modes	64.8

The generic symbol h^- represents a charged pion or kaon

from the same underlying processes, kinematics of these two classes of events are expected to be the same, aside from the response of the detector to a muon or to a τ_h jet. The basic idea of the method is to smear the muon p_T in the CS events, using MC-derived response functions (the "templates"), in order to emulate the τ_h jet response. Global hadronic variables such as N_jet, $N_\mathrm{b\text{-}jet}$, H_T, and $H_\mathrm{T}^\mathrm{miss}$ are then recomputed, and the full analysis selection procedure is subsequently applied.

The smearing of muon p_T in the CS usually causes $H_\mathrm{T}^\mathrm{miss}$ to increase, which is due to existence of neutrinos in the hadronically decaying τ events that carry away a part of the energy in the event. This itself in most of the cases leads to a lower response which means the muon in the event will be replaced by a less energetic component. To ensure that the whole $H_\mathrm{T}^\mathrm{miss}$ range in the search region is covered after the smearing is fulfilled, CS events need to be collected with a lower $H_\mathrm{T}^\mathrm{miss}$ threshold than the nominal search trigger provides. Therefore, we use a $\mu + H_\mathrm{T}$ cross trigger, `HLT_Mu15_IsoVVVL_PFHT350_v`. The performance of this trigger is discussed in Sect. 7.2. The trigger is fully efficient in terms of the hadronic variables (N_jet, H_T, $H_\mathrm{T}^\mathrm{miss}$) in the search region. The muon trigger efficiency is $\epsilon^{\mu}_{\mathrm{Trig}} = 95.1^{+0.5}_{-0.6} \pm 1.0\%$ and we correct for it.

7.5.3.3 The τ_h Response Templates

The τ_h response templates are obtained from $\mathrm{t\bar{t}}$ and W + jets simulation as follows. A reconstructed jet, defined as described below, is matched to a generator-level τ_h lepton with $|\eta| < 2.1$ and $p_\mathrm{T}(\tau_h^\mathrm{true}) > 20\,\mathrm{GeV}$, where $p_\mathrm{T}(\tau_h)_\mathrm{gen}$ is the p_T value of the generator-level τ_h lepton including the contribution of the daughter neutrino. For the purposes of this matching, the direction of the generator-level τ_h lepton is defined by its three-momentum minus the daughter-neutrino three-momentum. The matching criterion is $\Delta R(\mathrm{jet}, \tau_h^\mathrm{true}) = \sqrt{(\Delta\eta)^2 + (\Delta\phi)^2} < 0.1$ for $p_\mathrm{T}(\tau_h^\mathrm{true}) > 50\,\mathrm{GeV}$, and $\Delta R(\mathrm{jet}, \tau_h^\mathrm{true}) < 0.2$ for $20 < p_\mathrm{T}(\tau_h^\mathrm{true}) < 50\,\mathrm{GeV}$, where we use a less restrictive matching criterion in the latter case in order to maintain a high matching efficiency even for small $p_\mathrm{T}(\tau_h^\mathrm{true})$. The matched detector-level jet with the smallest ΔR is considered to be the reconstructed τ_h jet.

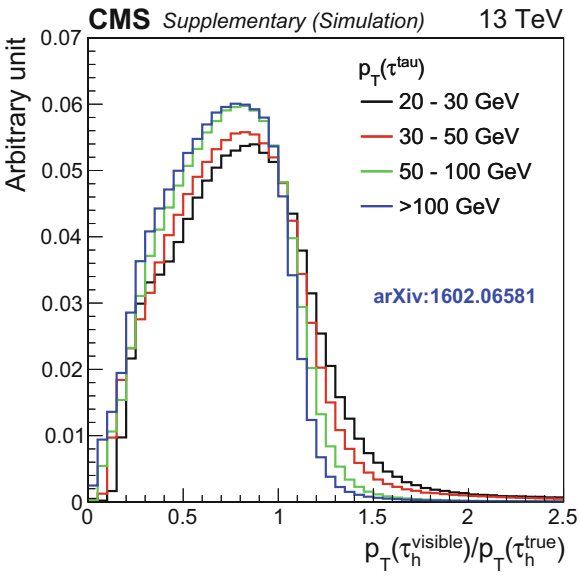

Fig. 7.10 The hadronically decaying τ lepton (τ_h) response templates: distributions of τ_h visible-p_T over true p_T of τ_h, $p_T(\tau_h^{visible})/p_T(\tau_h^{true})$, in intervals of $p_T(\tau_h^{true})$ as determined from simulated $t\bar{t}$ and W + jets events

The ratio between the p_T values of the matched detector- and generator-level τ_h objects, $p_T(\tau_h^{visible})/p_T(\tau_h^{true})$, is formed. The simulated distributions of $p_T(\tau_h^{visible})/p_T(\tau_h^{true})$ for different intervals of $p_T(\tau_h)_{gen}$ are shown in Fig. 7.10. These distributions define the τ_h response templates. The longer tails at large $p_T(\tau_h^{visible})/p_T(\tau_h^{true})$ seen for smaller values of $p_T(\tau_h^{true})$ arise from the degradation of transverse momentum resolution at small p_T.

7.5.3.4 Misidentification of τ_h Jets as b Jets

Hadronically decaying τ leptons have a non-negligible probability to be erroneously identified as b jets. This misidentification must be taken into account in order to accurately predict the $N_{b\text{-jet}}$ distribution of τ_h background events, i.e., to assign a τ_h background event to the most appropriate search bin.

The misidentification rates of τ_h jets as b jets (b-mistag) in simulated $t\bar{t}$ and W + jets events are shown as a function of jet p_T in Fig. 7.11 by the distributions labeled "(a)" and "(b)." The corresponding results for muon jets are shown by the distributions labeled "(c)" and "(d)," where a "muon jet" refers to the CS muons discussed above along with all other particles clustered with the muon into the same jet. It is this muon's p_T that is smeared by the τ_h response function shown in Fig. 7.10 to model the τ_h background. For W + jets events, the b-mistag rate of τ_h jets is seen to be around 4–5% independent of jet p_T. For $t\bar{t}$ events, the b-mistag rate of τ_h jets is around 5% for $p_T \lesssim 50$ GeV, but it increases to 40–50% as p_T increases. For muon jets, the b-mistag rate is negligible for W + jets events, while for $t\bar{t}$ events it is negligible for $p_T \lesssim 50$ GeV but increases to ~40% at high p_T.

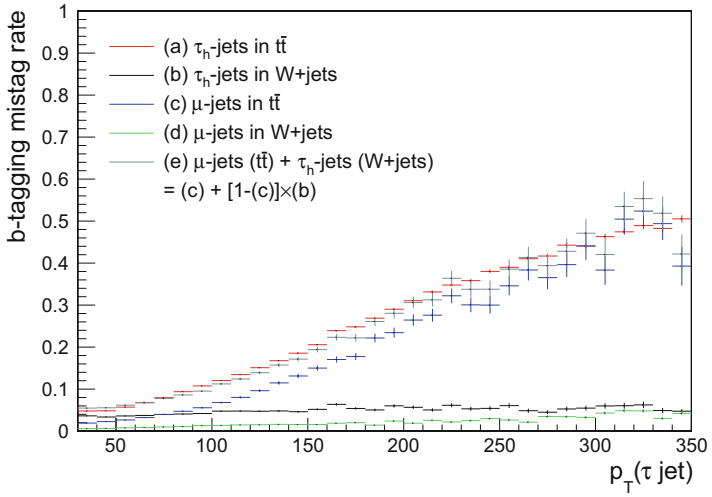

Fig. 7.11 The rate for τ_h jets (a,b) and muon jets (c,d) to be misidentified as a b jet as a function of jet p_T in simulated $t\bar{t}$ and W + jets events. The distribution labeled "(e)" shows the performance of our model in which we apply the τ_h b-mistag rate from W + jets events to muon jets in $t\bar{t}$ events to emulate the overall τ_h b-mistag behavior. It is similar to the MC expectation shown by distribution "(a)"

The conclusion is that the intrinsic b-mistag rate of τ_h and muon jets is what is obtained from the W + jets sample and is between 0 and 5% in both $t\bar{t}$ and W + jets events. The increase in the b-mistag rates of τ_h and muon jets in $t\bar{t}$ events as p_T increases is due to the nearby true b quark from the same top-quark decay. Therefore, the behavior of τ_h and muon jet events is the same with respect to the presence of a nearby b quark, i.e., with respect to increasing p_T in $t\bar{t}$ events.

Based on these results, the $N_{\text{b-jet}}$ distribution of the τ_h background is constructed as follows. The probability $P^{\tau_h}_{\text{b-mistag}}$ for a τ_h jet to be b-mistagged is determined to be

$$P^{\tau_h}_{\text{b-mistag}} = P^{\mu}_{\text{b-mistag}} + (1 - P^{\mu}_{\text{b-mistag}})P^{\text{W+jets}}_{\text{b-mistag}}, \tag{7.10}$$

where $P^{\mu}_{\text{b-mistag}}$ is the probability for a muon jet to be b-mistagged and accounts for b-mistagging due to proximity to a b quark. The second term on the right-hand side of Eq. (7.10) is to account for probability for an intrinsic τ_h jet b-mistag and has a value of about 5%. This term consists of the probability $1 - P^{\mu}_{\text{b-mistag}}$ that a muon jet is not b-mistagged (thus making it consistent with the expectation for muon jets in W + jets and in low-p_T $t\bar{t}$ events) multiplied by the probability $P^{\text{W+jets}}_{\text{b-mistag}}$ for a τ_h jet in a W + jets event or low-p_T $t\bar{t}$ event to be mistagged. In Fig. 7.11 (left), $P^{\tau_h}_{\text{b-mistag}}$ is shown by (e), which is the combination of distributions (e) = (c) + [1 − (c)] (b).

We determine the b-jet multiplicity $N_{\text{b-CS}}$ of each CS event using the nominal b-tagging requirements described in Sect. 7.3. If the muon jet in the CS event is not

b-tagged, the CS event is entered into the $N_{\text{b-jet}}$ distribution of the τ_h background twice. Once for $N_{\text{b-jet}} = \text{N}_{\text{b-CS}}$ with weight $w^{\tau_h}_{\text{b-mistag}} = 1 - P^{\tau_h}_{\text{b-mistag}}$, and once for $N_{\text{b-jet}} = \text{N}_{\text{b-CS}} + 1$ with weight $w^{\tau_h}_{\text{b-mistag}} = P^{\tau_h}_{\text{b-mistag}}$, i.e., we adjust the number of tagged b jets contributed by the CS event upwards by one in correspondence with the probability for the event-by-event τ_h b-misidentification. In contrast, if the muon jet in the CS event is b-tagged, we enter the event into the τ_h background distribution once, with value $N_{\text{b-jet}} = \text{N}_{\text{b-CS}}$ and weight $w^{\tau_h}_{\text{b-mistag}} = 1$. Note that τ_h jets with $p_{\text{T}}(\tau_h)_{\text{reco}} < 30\,\text{GeV}$ are not included in the above procedure since jets (including b jets) are required to have $p_{\text{T}} > 30\,\text{GeV}$ in this analysis.

This procedure works well to emulate the $N_{\text{b-jet}}$ distribution for the τ_h background as shown in the closure tests presented in Fig. 7.18.

7.5.3.5 Muon Control Sample Selection and Hadronic τ Background Prediction

Events in the muon data control sample are selected using the following criteria:

- exactly one isolated muon with $p_{\text{T}} > 20\,\text{GeV}$ and $|\eta| < 2.1$, based on the muon isolation and ID criteria of Sect. 7.3;
- No isolated electron candidate defined according to the criteria of Sect. 7.3;
- $m_{\text{T}}(\mu, E^{\text{miss}}_{\text{T}}) < 100\,\text{GeV}$, to reduce potential contributions of signal events.

Here the $m_{\text{T}}(\mu, E^{\text{miss}}_{\text{T}}) < 100\,\text{GeV}$ requirement reduces the signal contamination. The idea is, if supersymmetric interactions happen to exist in the events, they may decay to muons and consequently the muons can end up entering the control sample. Since the template method is based on the assumption that muons in the control sample are from W decays, this will bias the final background estimation. On the other hand, it can be shown that m_{T} of muons is always smaller than the mass of their parents and also supersymmetric particles are heavier than W boson. Therefore, one way to filter out muons from signal events is to set a selection on their m_{T}.

For each event in this sample, the measured muon transverse momentum $p_{\text{T}}(\mu)$ is smeared according to the τ_h response functions of Fig. 7.10. The smearing is performed as follows. We assume that the value of $p_{\text{T}}(\mu)$ can be used to represent the generator-level $p_{\text{T}}(\tau_h)_{\text{gen}}$ of the simulated τ_h leptons. This assumption is justified by the good momentum resolution achieved for muons in the CMS detector, i.e., the close correspondence expected between the detector-level and underlying true values of muon momentum. A τ_h response template is chosen based on the $p_{\text{T}}(\tau_h)_{\text{gen}}$ interval into which $p_{\text{T}}(\mu)$ falls. For a given template, we successively choose each bin in the template, replacing $p_{\text{T}}(\mu)$ in the CS event with the value of $p_{\text{T}}(\tau_h)_{\text{reco}}$ corresponding to that bin. In this manner, all bins in the template are uniformly sampled. For each choice of $p_{\text{T}}(\tau_h)_{\text{reco}}$, the kinematic variables in the event, viz., N_{jet}, H_{T}, $H^{\text{miss}}_{\text{T}}$, and the $\Delta\phi(j_i,\ H^{\text{miss}}_{\text{T}})$ variables, are calculated. A weight is then determined for the event to contribute to each bin of the kinematic distributions and thus to each search bin. We include a weight to account for the probability that a τ_h jet is misidentified as a b jet; see Sect. 7.5.3.4. The following corrections are also incorporated:

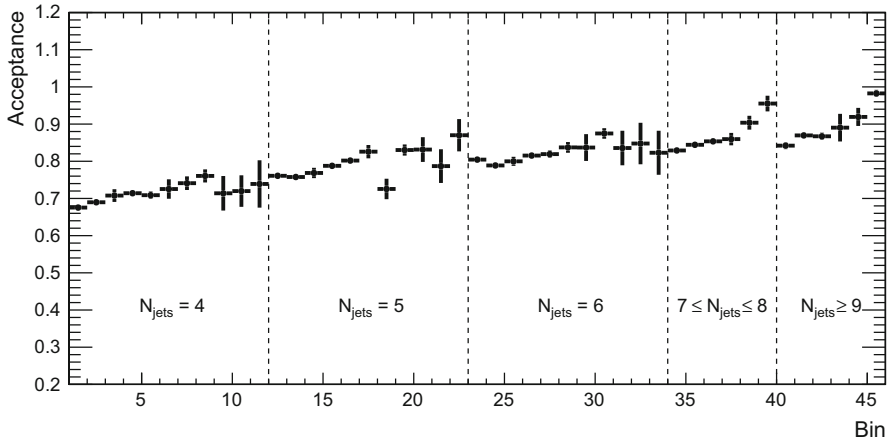

Fig. 7.12 Acceptance $\epsilon^{\mu}_{\text{Acc}}$ of hadronically decaying τ leptons for $p_{\text{T}} > 20\,\text{GeV}$ and $|\eta| < 2.1$. The results are shown for eleven (six) H_{T}–$H_{\text{T}}^{\text{miss}}$ bins as defined in Fig. 7.13 (7.6) for $N_{\text{jet}} = 4$, 5, and 6 (7–8, 9+) bins integrated over the four bins of $N_{\text{b-jet}}$ (in total 45 bins)

- the ratio of branching fractions $\mathcal{B}(\text{W} \to \tau_h \nu)/\mathcal{B}(\text{W} \to \mu\nu) = 0.6476 \pm 0.0024$ [56];
- the muon reconstruction and identification efficiency $\epsilon^{\mu}_{\text{Reco}}$, and the muon isolation efficiency $\epsilon^{\mu}_{\text{ISO}}$ [p_{T}, activity[1]];
- the muon acceptance ($\epsilon^{\mu}_{\text{Acc}}$) [$N_{\text{jet}}$, $H_{\text{T}}^{\text{miss}}$] (see Figs. 7.12 and 7.13);
- the m_{T} selection efficiency ($\epsilon_{m_{\text{T}}}$) [N_{jet}, H_{T}, $H_{\text{T}}^{\text{miss}}$] (see Fig. 7.14);
- the contamination of the CS by $\text{W} \to \tau\nu_\tau \to \mu\nu_\mu\bar{\nu}_\tau\nu_\tau$ events (as opposed to the assumed $\text{W} \to \mu\nu_\mu$ events), accounted for with the correction term $(1 - f_{\tau\to\mu})$ [N_{jet}, H_{T}, $H_{\text{T}}^{\text{miss}}$] (see Fig. 7.15);
- the dileptonic event contamination of the CS, accounted for with the correction term $(1 - f_{\ell\ell})$, where $f_{\ell\ell} = 0.02$;
- the isolated-track veto efficiency (ϵ_{isotrk}) [N_{jet}, H_{T}, $H_{\text{T}}^{\text{miss}}$] (see Fig. 7.16).

The muon reconstruction and identification efficiency and the muon isolation efficiency are the same as that used for the lost-lepton background determination, and they refer to the fractions of muons that satisfy each selection requirement. The variables in block parentheses are those that are used to parameterize the indicated correction. For items without block parentheses, a constant correction factor is used. The muon reconstruction and identification efficiency is generally higher than 90%. The isolation efficiency is typically higher than 95%; however, it drops rapidly with increasing activity variable. The muon acceptance accounts for muons that fall outside the kinematic region of $p_{\text{T}} > 20\,\text{GeV}$ and $|\eta| < 2.1$, which is typically 20–30%.

[1]The activity variable is defined as the sum p_{T} of PF candidates in an annulus outside the isolation cone up to $\Delta R = 0.4$ relative to the p_{T} of the lepton. This variable is designed as a measure of hadronic activities around each lepton.

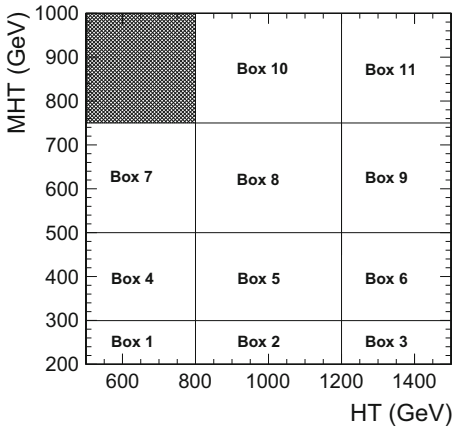

Fig. 7.13 Two-dimensional plane in H_T and H_T^{miss} showing bins used to parametrize the acceptance (ϵ_{Acc}^{μ}), m_T selection efficiency (ϵ_{m_T}), contamination of the CS by $W \to \tau\nu_\tau \to \mu\nu_\mu\bar{\nu}_\tau\nu_\tau$ events ($f_{\tau\to\mu}$), and the isolated-track veto efficiency (ϵ_{isotrk}) for $N_{jet} \leq 6$. For $N_{jet} \geq 7$, coarser bins in H_T–H_T^{miss} as shown in Fig. 7.6 are used

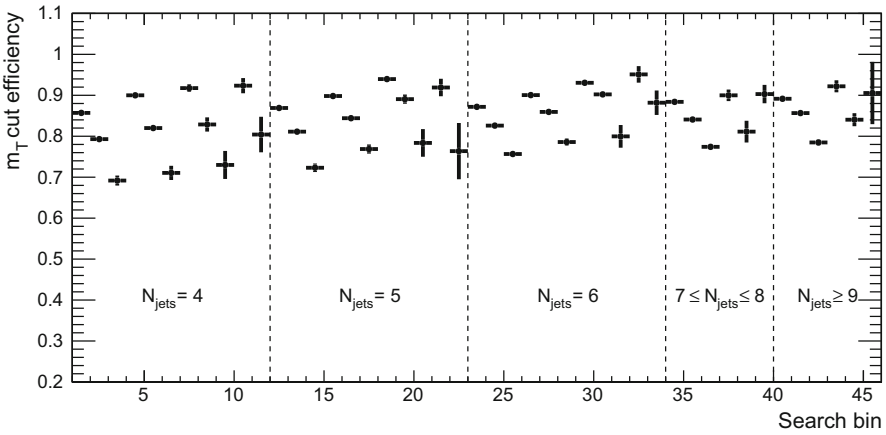

Fig. 7.14 The efficiency ϵ_{m_T} of the muon m_T selection. The results are shown for eleven (six) H_T–H_T^{miss} bins as defined in Fig. 7.13 (7.6) for $N_{jet} = 4$, 5, and 6 (7–8, 9+) bins integrated over the four bins of $N_{b\text{-jet}}$ (in total 45 bins)

This τ_h background estimation method utilizes the similarity between $W \to \mu\nu_\mu$ and $W \to \tau\nu_\tau$ events; therefore, contributions of muons from τ decays need to be subtracted, which is done by the correction term $1 - f_{\tau\to\mu}$. The value $f_{\tau\to\mu}$ is typically 15–25%. The contamination due to dilepton events in which one of the leptons is lost is accounted for by the correction term $1 - f_{\ell\ell}$.

About 30–40% of the τ_h background is rejected by the isolated-track veto, which works efficiently against 1-prong τ_h decays. The efficiency of this veto is obtained from simulated $t\bar{t}$, W + jets, and single-top quark event samples based on the fraction of events that survive the isolated-track veto.

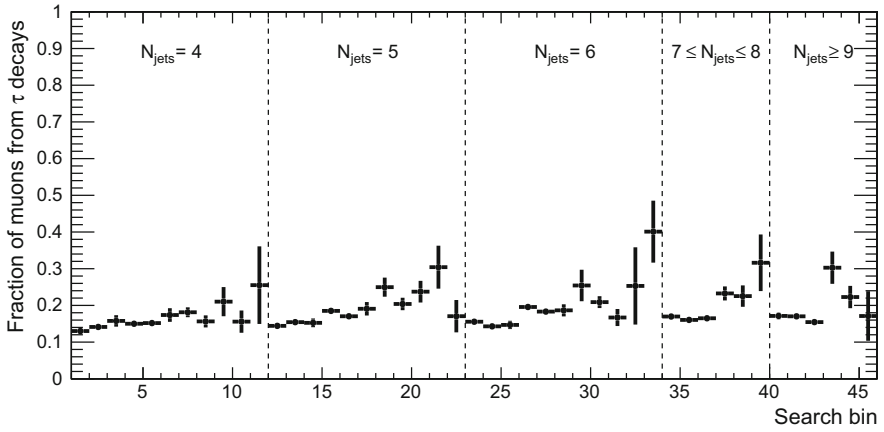

Fig. 7.15 The fraction $f_{\tau\to\mu}$ of muons from τ decays in the single-muon control sample, as determined from simulation. The results are shown for eleven (six) H_{T}–$H_{\mathrm{T}}^{\mathrm{miss}}$ bins as defined in Fig. 7.13 (7.6) for $N_{\mathrm{jet}} = 4$, 5, and 6 (7–8, 9+) bins integrated over the four bins of $N_{\text{b-jet}}$ (in total 45 bins)

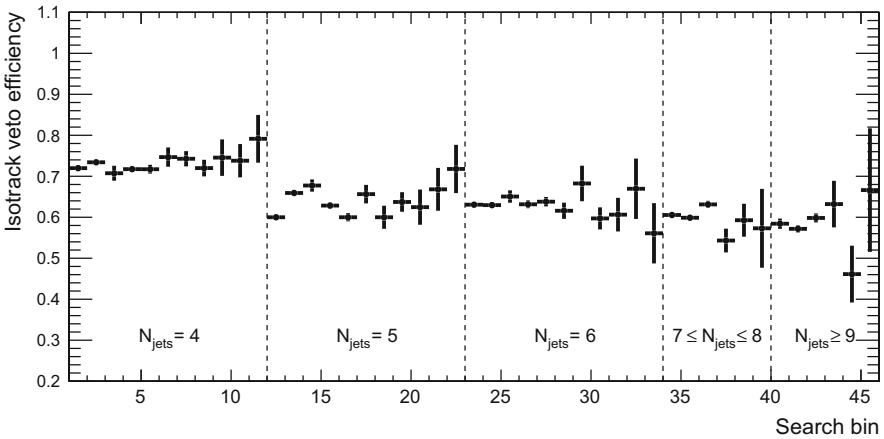

Fig. 7.16 The isolated-track veto efficiency $\epsilon_{\mathrm{isotrk}}$. The results are shown for eleven (six) H_{T}–$H_{\mathrm{T}}^{\mathrm{miss}}$ bins as defined in Fig. 7.13 (7.6) for $N_{\mathrm{jet}} = 4$, 5, and 6 (7–8, 9+) bins integrated over the four bins of $N_{\text{b-jet}}$ (in total 45 bins)

The τ_h background is given by

$$N_{\tau_h} = \sum_{i}^{N_{\mathrm{CS}}^{\mu}} \left(\sum_{j}^{\text{Template bins}} \left(P_{\tau_h}^{\mathrm{resp}} \sum_{k} w_{\text{b-mistag}}^{\tau_h} \right) \frac{1}{\epsilon_{\mathrm{Trig}}^{\mu} \epsilon_{\mathrm{Reco}}^{\mu} \epsilon_{\mathrm{ISO}}^{\mu}} \right.$$
$$\left. \times \frac{1}{\epsilon_{\mathrm{Acc}}^{\mu} \epsilon_{m_{\mathrm{T}}}^{\mu}} (1 - f_{\tau\to\mu})(1 - f_{\ell\ell}) \frac{\mathcal{B}(\mathrm{W} \to \tau_h \nu)}{\mathcal{B}(\mathrm{W} \to \mu\nu)} \epsilon_{\mathrm{isotrk}} \right), \tag{7.11}$$

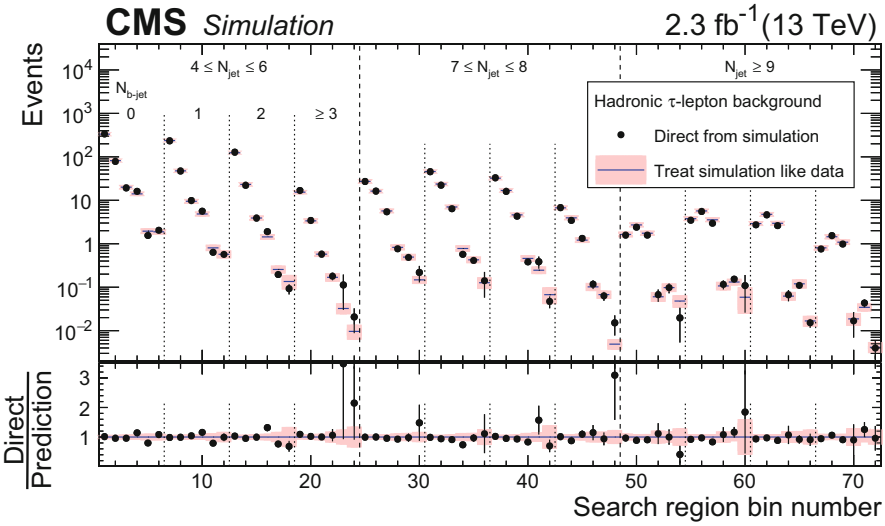

Fig. 7.17 The τ_h background in the 72 search bins of the analysis (intervals of H_T, H_T^{miss}, N_{jet}, and $N_{b\text{-jet}}$) as predicted directly from simulation (solid points) and as predicted by the data-driven background-determination procedure (shaded regions). The simulation makes use of $t\bar{t}$, W + jets, single-top, Drell-Yan, and other rare SM event samples

where the first summation is over the events in the μ + jets control sample, the second is over the bins of the τ_h response template ($P_{\tau_h}^{resp}$), and the third accounts for the probability to misidentify a τ_h jet as a b jet ($w_{b\text{-mistag}}^{\tau_h}$).

Closure tests of the τ_h background determination method, based on simulated $t\bar{t}$, W + jets, single-top, WW/WZ/ZZ, Drell-Yan samples, and other SM rare process samples are shown in Figs. 7.17 and 7.18. As shown in Fig. 7.17, the method closes within about 10% in most of the high statistics bins, validating this background estimation method. The larger of either the statistical uncertainty of the closure test in each search bin or the amount of the nonclosure is assigned as the systematic uncertainty in order to account for potential residual biases.

7.5.3.6 Systematic Uncertainties

Our estimation of hadronic τ background comes with uncertainties from different factors that are listed below:

- **Hadronic tau response template:** The response template of hadronic tau jets is modeled using MC simulation, so potential data-MC energy scale differences have to be considered. The uncertainty in the jet energy scale is evaluated in detail by the CMS jet and missing E_T physics object group (JetMET POG) using events with a dijet topology, as well as photon + jet, Z + jet and QCD multijet

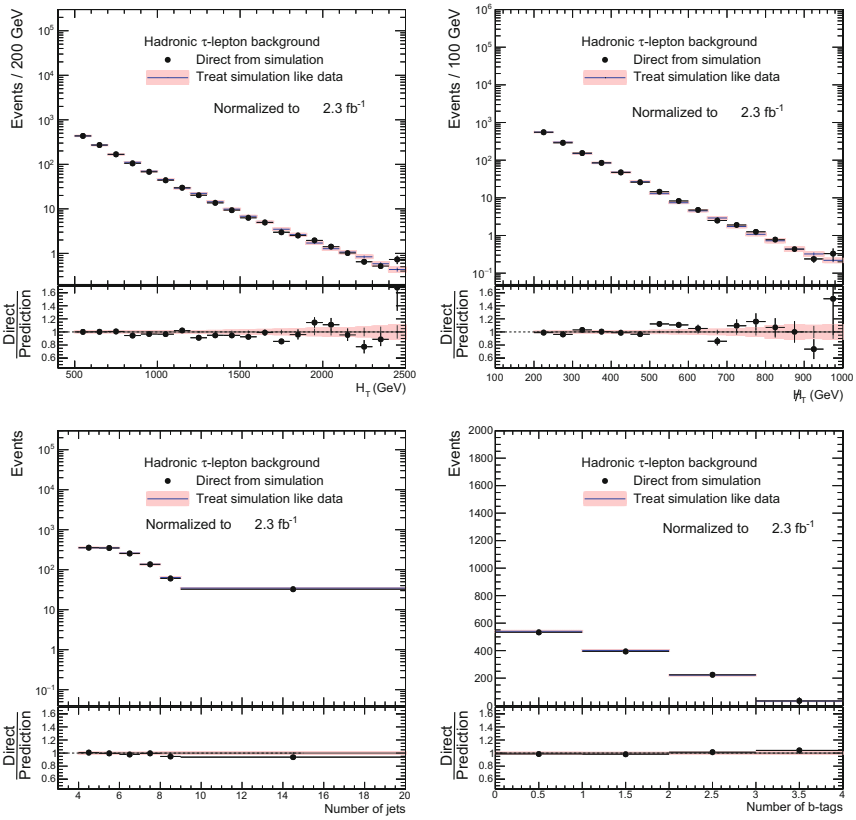

Fig. 7.18 The H_{T}, $H_{\mathrm{T}}^{\mathrm{miss}}$, N_{jet}, and $N_{\text{b-jet}}$ distributions as predicted directly from simulation (solid points) and as predicted by the data-driven background-determination procedure (shaded regions), for the baseline selection. The simulation makes use of $\mathrm{t\bar{t}}$, $\mathrm{W}+\mathrm{jets}$, single-top, Drell-Yan, and other rare SM event samples

events [57, 58]. The hadronic tau jet energy is varied by the amount of this jet energy scale uncertainty and the variation in the τ_h background prediction provides the background uncertainty from this source. This uncertainty is correlated across all signal bins and are modeled with a single nuisance parameter.

- **Mistagging rate of hadronic tau jet:** The b-tagging mistag rate for hadronic tau jets as measured in $\mathrm{W}+\mathrm{jets}$ simulated events is used in the method as discussed earlier. We conservatively vary this mistag rate by 50% to evaluate the uncertainty. This uncertainty is correlated across all signal bins and is modeled with a single nuisance parameter.
- **Muon reconstruction/ID/isolation efficiency:** The uncertainties on the data/MC corrections from "tag-and-probe" studies [59] with high purity $\mathrm{Z} \rightarrow \mu^{+}\mu^{-}$ events by the SUSY lepton scale factor (SF) group are considered [60]. In this method, one of the muons from $\mathrm{Z} \rightarrow \mu^{+}\mu^{-}$ decays is tagged by a stringent

muon selection and the fractions of the other muon candidates, called probes, that pass the reconstruction or identification or isolation requirements are measured to extract the efficiency of each muon selection criterion. These are correlated across all signal bins and are modeled with a single nuisance parameter.

- **Acceptance:** The uncertainty of the acceptance efficiency consists of the uncertainty in the parton distribution functions (PDF) and in the renormalization and factorization scales used for the MC generation as well as the uncertainty arising from the statistical precision of the corrections. The uncertainties due to PDF are evaluated by computing the acceptance with 100 different sets of PDF weights stored in events representing uncertainties from NNPDF3.0 (100 MC replicas [40, 61]) and by finding the maximum variation in the acceptance. The uncertainties due to the renormalization and factorization scale are evaluated by computing the acceptance with eight different sets of renormalization and factorization scales varied by a factor of two up and down from the nominal values and by finding the maximum variation in the acceptance. These are done in $\mathrm{t\bar{t}}$ and W + jets MC samples in which these weights for the PDF, renormalization, and factorization scale uncertainties are available.
- **Dilepton correction:** This contamination is determined to be about 2% across all search regions. 100% of this subtraction is considered for the systematic uncertainty.
- $\boldsymbol{m_{\mathrm{T}}}$ **cut efficiency:** The uncertainty associated with the m_{T} cut comes from (1) the statistical uncertainty of determining this efficiency from MC, and the uncertainty in the $E_{\mathrm{T}}^{\mathrm{miss}}$ scale. $E_{\mathrm{T}}^{\mathrm{miss}}$ is scaled up/down by 30% and we evaluate the variations in the m_{T} cut efficiency. The variation of the cut efficiency is then assigned as a systematic uncertainty. This procedure yields about 5% uncertainties across the search bins. These uncertainties are treated as correlated across all signal bins and are modeled with a single nuisance parameter.
- **Isolated track vetoes:** The isolated track veto efficiency that matters most here is the efficiency of hadronic track vetoes on τ_h jets. There is no straightforward way to evaluate the isolation efficiency of hadronic tracks; instead we must extrapolate the validation of the muon track efficiencies to the hadronic tracks. We justify the assumption that the track isolation efficiencies for muon tracks are an appropriate proxy for the track isolation efficiencies for hadronic tracks by arguing (1) most of the τ leptons in the events rejected by the hadronic track veto undergo one-prong decays, (2) since the isolation is computed by summing over neighboring charged tracks, and no neutral candidates, the isolation distributions for muon tracks should be similar to those for pions from 1-prong tau decays.
- **MC closure:** The MC closure test is found to be good within 10% in most of the search bins with high statistics except for three bins as discussed above, and in tight search regions the statistical uncertainties of the closure test go beyond 10%. The larger value of the nonclosure or the statistical uncertainty on nonclosure is assigned for each bin as bin-to-bin uncorrelated uncertainties. In case this closure evaluation is dominated by low MC statistics and a high spread in weights, the assigned nonclosure uncertainty is cut off at 100%.

Many of the systematic uncertainties (muon reconstruction/ID/isolation efficiency, acceptance, dilepton correction, m_{T} cut efficiency) are common with the lost-lepton background estimation method and these uncertainties are considered fully correlated in the statistical interpretation of the search discussed in Sect. 7.6.

7.5.3.7 Hadronic-Tau Background Prediction

Figure 7.19 presents the full predictions for the hadronic-tau background based on 2.3 fb^{-1} of the single muon dataset for 72 search bins (blue lines with light-red shades). The shaded areas represent statistical uncertainties which include the extra additional uncertainty term to account for statistical uncertainties of zero observed events with high weights in the μ + jets control sample. This is done based on the Poisson statistical error on zero observed as given by the Garwood interval [62], which gives a good coverage of the background in statistics tests. These data-based predictions are compared to the MC expectations of τ_h background as a reference. Figure 7.20 presents the predictions as a function of four search variables, H_{T}, $H_{\mathrm{T}}^{\mathrm{miss}}$, N_{jet}, and $N_{\text{b-jet}}$ where the expectation from MC and the data-driven predictions have overall similar shapes but are different in normalization. This difference demonstrates the importance of data-driven methods and why a background estimation should not directly rely on predictions from MC samples.

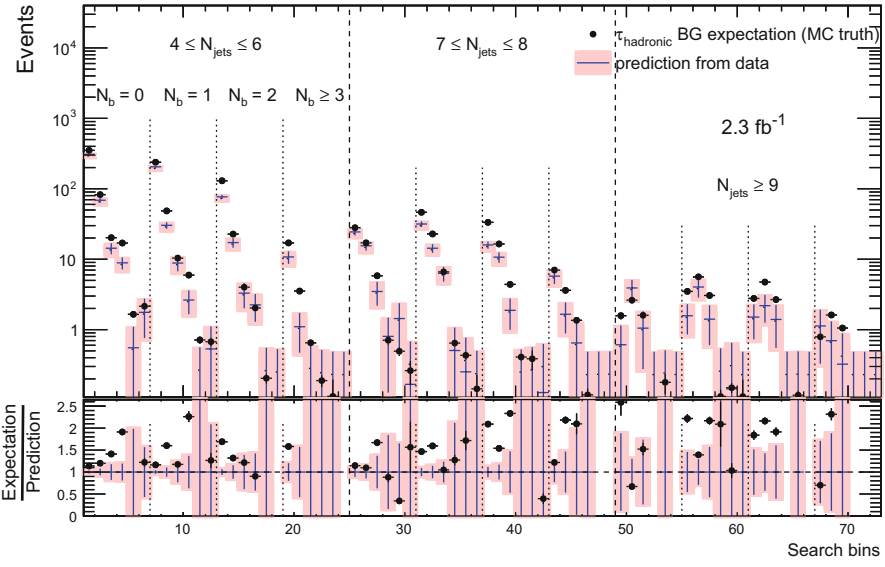

Fig. 7.19 The τ_h background in the 72 search bins of the analysis (intervals of H_{T}, $H_{\mathrm{T}}^{\mathrm{miss}}$, N_{jet}, and $N_{\text{b-jet}}$) as predicted by performing the data-driven background-determination procedure on the 2.3 fb^{-1} of data (shaded regions) compared to the τ_h background expectations from simulation (solid points). The simulation makes use of $\mathrm{t\bar{t}}$, W + jets, single-top, Drell-Yan, and other rare SM event samples

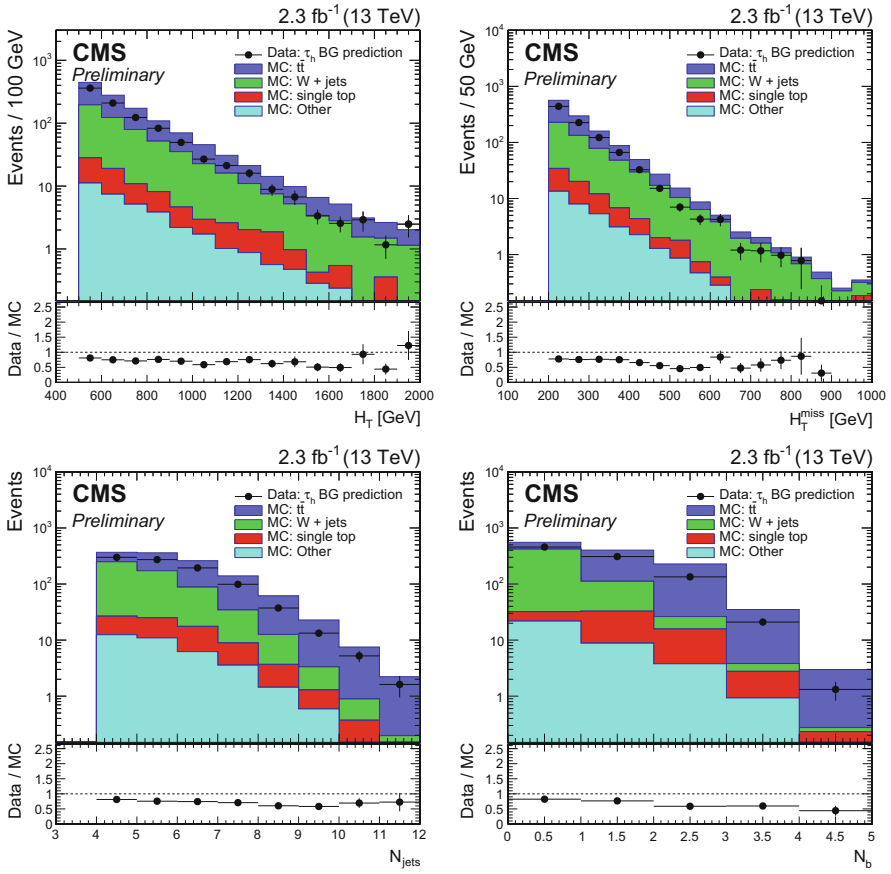

Fig. 7.20 The H_T, H_T^{miss}, N_{jet}, and $N_{b\text{-jet}}$ distributions as predicted by performing the data-driven background-determination procedure on the 2.3 fb^{-1} of data (shaded regions), compared to the τ_h background expectations from simulation (solid points) for the baseline selection. The simulation makes use of $t\bar{t}$, W + jets, single-top, Drell-Yan, and other rare SM event samples

7.6 Results

The observed numbers of events in the 72 search regions are shown in Fig. 7.21 in comparison to the summed predictions for the SM backgrounds, with numerical values tabulated in Appendix. The predicted background is observed to be statistically compatible with the data for all 72 regions. Therefore, we do not observe evidence for new physics.

Figure 7.22 presents one-dimensional projections of the results in H_T^{miss} or H_T after criteria are imposed, as indicated in the legends, to select intervals of the search region parameter space particularly sensitive to the T1bbbb, T1tttt, T1qqqq, or T5qqqqVV scenario. In each case, example distributions are shown for two signal

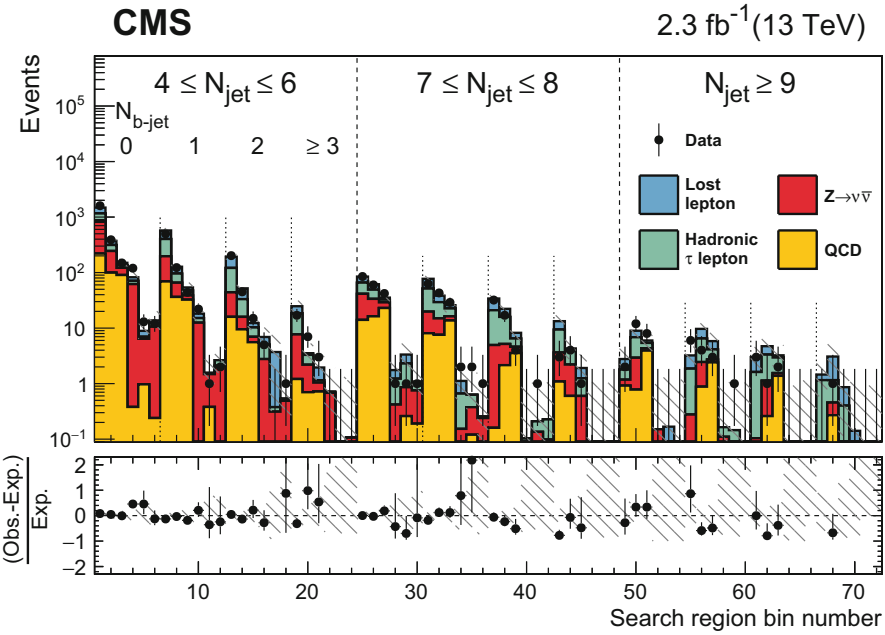

Fig. 7.21 Observed numbers of events and corresponding SM background predictions in the 72 search regions of the analysis, with fractional differences shown in the lower panel. The shaded regions indicate the total uncertainties in the background predictions. The labeling of the search regions is the same as in Fig. 7.7

scenarios not excluded by Run 1 studies [7, 8]. These scenarios, one with $m_{\tilde{g}} \gg m_{\tilde{\chi}_1^0}$ and one with $m_{\tilde{\chi}_1^0} \sim m_{\tilde{g}}$, lie well within the parameter space excluded by the present analysis. A likelihood fit to data is used to set limits on the production cross sections of the signal scenarios. The limits are determined as a function of $m_{\tilde{\chi}_1^0}$ and $m_{\tilde{g}}$. The likelihood function is the product of Poisson probability density functions, one for each signal region, and constraint terms that account for uncertainties in the background predictions and signal yields. These uncertainties are treated as nuisance parameters with log-normal probability density functions. Correlations are taken into account where appropriate. The signal model uncertainties associated with the renormalization and factorization scales, ISR, the jet energy scale, the b jet tagging, and the statistical fluctuations vary substantially with the event kinematics and are evaluated as a function of $m_{\tilde{\chi}_1^0}$ and $m_{\tilde{g}}$. The test statistic is $q_\mu = -2\ln\left(\mathcal{L}_\mu/\mathcal{L}_{\max}\right)$, where $\mathcal{L}_{\max}$ is the maximum likelihood determined by allowing all parameters including the SUSY signal strength μ to vary, and $\mathcal{L}_\mu$ is the maximum likelihood for a fixed signal strength. To set limits, we use asymptotic results for the test statistic [63] and the CL_s method described in [64, 65]. More details are provided in [66, 67].

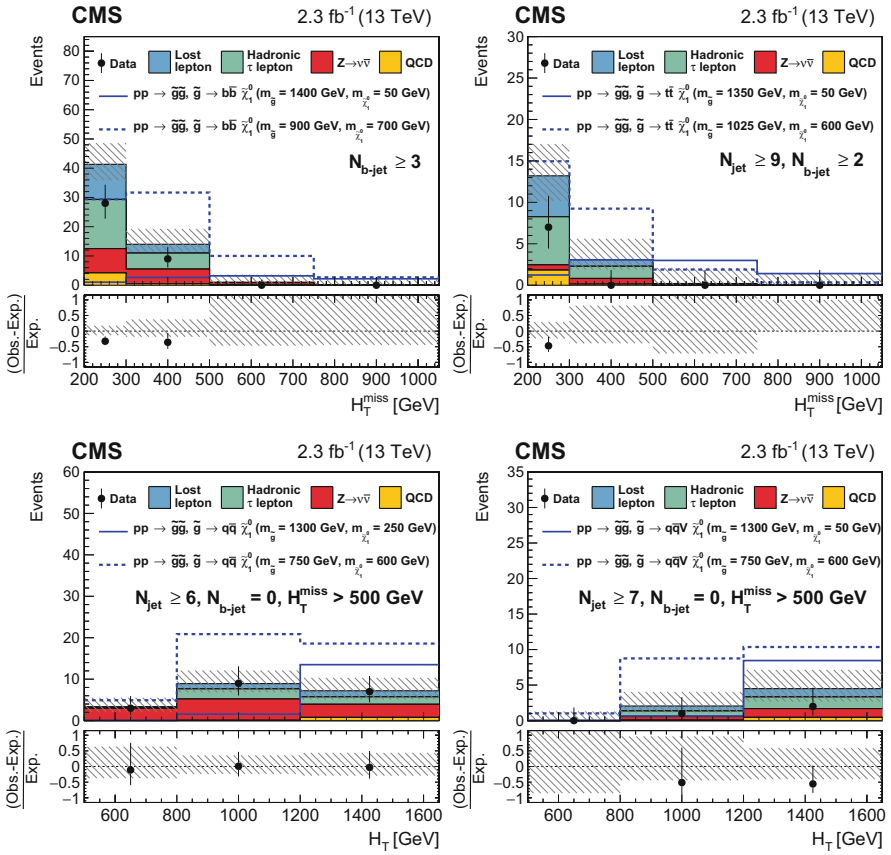

Fig. 7.22 Observed numbers of events and corresponding SM background predictions for intervals of the search region parameter space particularly sensitive to the (upper left) T1bbbb, (upper right) T1tttt, (lower left) T1qqqq, and (lower right) T5qqqqVV scenarios. The selection requirements are given in the figure legends. The hatched regions indicate the total uncertainties in the background predictions. The (unstacked) results for two example signal scenarios are shown in each instance, one with $m_{\tilde{g}} \gg m_{\tilde{\chi}_1^0}$ and the other with $m_{\tilde{\chi}_1^0} \sim m_{\tilde{g}}$. Note that for purposes of presentation, the four-bin scheme discussed in Sect. 7.5.1 is used for the $H_{\mathrm{T}}^{\mathrm{miss}}$ variable

We proceed to evaluate 95% confidence level (CL) upper limits on the signal cross sections. The potential contributions of signal events to the control regions are taken into account when computing these limits. The cross section computed at the NLO + NLL accuracy is used as a reference to evaluate corresponding 95% CL exclusion curves. In addition to the observed limits, expected limits are derived by evaluating the expected Poisson fluctuations around the predicted numbers of background events when evaluating the test statistic. The results are shown in Fig. 7.23. For a massless LSP, we exclude gluinos with masses below 1600, 1550, 1440, and 1450 GeV, respectively, for the T1bbbb, T1tttt, T1qqqq, and T5qqqqVV

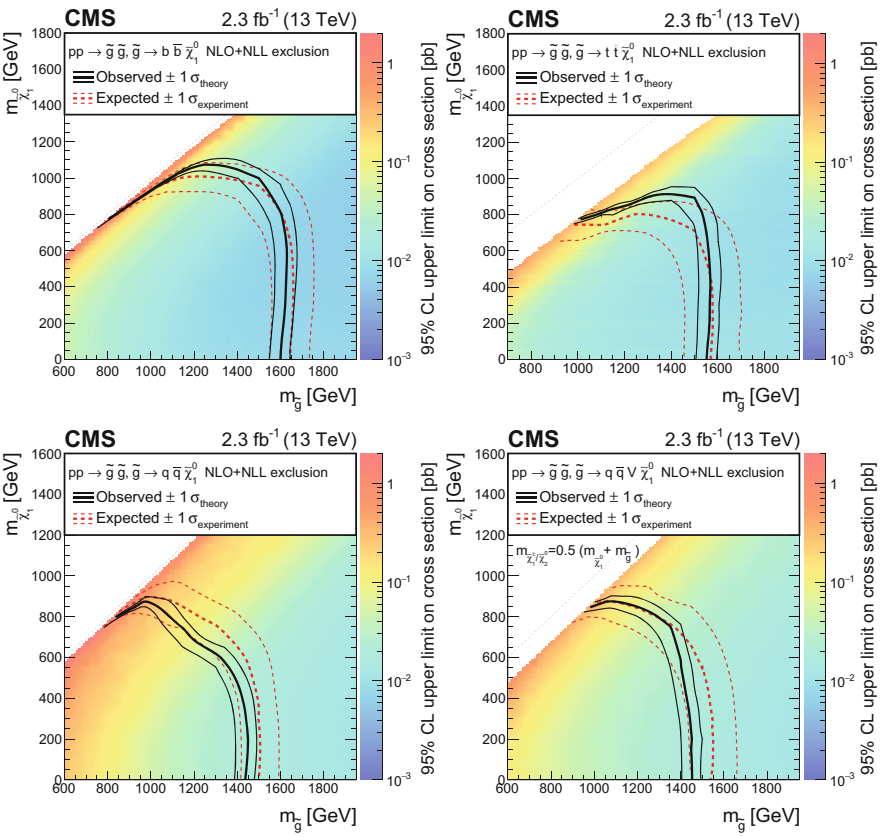

Fig. 7.23 The 95% CL upper limits on the production cross sections for the (upper left) T1bbbb, (upper right) T1tttt, (lower left) T1qqqq, and (lower right) T5qqqqVV simplified models of supersymmetry, shown as a function of the gluino and LSP masses $m_{\tilde{g}}$ and $m_{\tilde{\chi}_1^0}$. For the T5qqqqVV model, the masses of the intermediate $\tilde{\chi}_2^0$ and $\tilde{\chi}_1^\pm$ states are taken to be the mean of $m_{\tilde{\chi}_1^0}$ and $m_{\tilde{g}}$. The solid (black) curves show the observed exclusion contours assuming the NLO + NLL cross sections [32–36], with the corresponding ± 1 standard deviation uncertainties [68]. The dashed (red) curves present the expected limits with ± 1 standard deviation experimental uncertainties. The diagonal dashed (grey) lines indicate the kinematic limits of the respective decay

scenarios. These results significantly extend those obtained at $\sqrt{s} = 8\,\text{TeV}$, for which the corresponding limits are around 1150 GeV [7, 8] for the three T1 models and 1280 GeV [8] for the T5 model.

References

1. S. Dimopoulos, G.F. Giudice, Phys. Lett. B **357**, 573 (1995) [arXiv:hep-ph/9507282]
2. R. Barbieri, D. Pappadopulo, JHEP **10**, 061 (2009) [arXiv:0906.4546]

3. M. Papucci, J.T. Ruderman, A. Weiler, JHEP **09**, 035 (2012) [arXiv:1110.6926]
4. G.R. Farrar, P. Fayet, Phys. Lett. B **76**, 575 (1978)
5. CMS Collaboration, Phys. Lett. B **758**, 152 (2016) [arXiv:1602.06581]
6. CMS Collaboration, Phys. Rev. D **88**, 052017 (2013) [arXiv:1301.2175]
7. CMS Collaboration, Phys. Lett. B **725**, 243 (2013) [arXiv:1305.2390]
8. CMS Collaboration, JHEP **06**, 055 (2014) [arXiv:1402.4770]
9. UA1 Collaboration, Phys. Lett. B **122**, 103 (1983)
10. CMS Collaboration, Phys. Rev. Lett. **119**, 151802 (2017) [arXiv:1605.04608]
11. J. Alwall et al., JHEP **07**, 079 (2014) [arXiv:1405.0301]
12. P. Nason, JHEP **11**, 040 (2004) [arXiv:hep-ph/0409146]
13. S. Frixione, P. Nason, C. Oleari, JHEP **11**, 070 (2007) [arXiv:0709.2092]
14. S. Alioli, P. Nason, C. Oleari, E. Re, JHEP **09**, 111 (2009) [arXiv:0907.4076]
15. S. Alioli, P. Nason, C. Oleari, E. Re, JHEP **06**, 043 (2010) [arXiv:1002.2581]
16. E. Re, Eur. Phys. J. C **71**, 1547 (2011) [arXiv:1009.2450]
17. T. Melia, P. Nason, R. Rontsch, G. Zanderighi, JHEP **11**, 078 (2011) [arXiv:1107.5051]
18. S. Agostinelli et al., Nucl. Instrum. Methods A **506**, 250 (2003)
19. S. Alioli, P. Nason, C. Oleari, E. Re, JHEP **09**, 111 (2009) [arXiv:0907.4076] [Erratum: JHEP **02**, 011 (2010)]
20. E. Re, Eur. Phys. J. C **71**, 1547 (2011) [arXiv:1009.2450]
21. J. Alwall, R. Frederix, S. Frixione, V. Hirschi, F. Maltoni, O. Mattelaer, H.S. Shao, T. Stelzer, P. Torrielli, M. Zaro, JHEP **07**, 079 (2014) [arXiv:1405.0301]
22. T. Melia, P. Nason, R. Rontsch, G. Zanderighi, JHEP **11**, 078 (2011) [arXiv:1107.5051]
23. M. Beneke, P. Falgari, S. Klein, C. Schwinn, Nucl. Phys. B **855**, 695 (2012) [arXiv:1109.1536]
24. M. Cacciari, M. Czakon, M. Mangano, A. Mitov, P. Nason, Phys. Lett. B **710**, 612 (2012) [arXiv:1111.5869]
25. P. Bärnreuther, M. Czakon, A. Mitov, Phys. Rev. Lett. **109**, 132001 (2012) [arXiv:1204.5201]
26. M. Czakon, A. Mitov, JHEP **12**, 054 (2012) [arXiv:1207.0236]
27. M. Czakon, A. Mitov, JHEP **01**, 080 (2013) [arXiv:1210.6832]
28. M. Czakon, P. Fiedler, A. Mitov, Phys. Rev. Lett. **110**, 252004 (2013) [arXiv:1303.6254]
29. R. Gavin, Y. Li, F. Petriello, S. Quackenbush, Comput. Phys. Commun. **184**, 208 (2013) [arXiv:1201.5896]
30. R. Gavin, Y. Li, F. Petriello, S. Quackenbush, Comput. Phys. Commun. **182**, 2388 (2011) [arXiv:1011.3540]
31. T. Sjöstrand, S. Ask, J.R. Christiansen, R. Corke, N. Desai, P. Ilten, S. Mrenna, S. Prestel, C.O. Rasmussen, P.Z. Skands, Comput. Phys. Commun. **191**, 159 (2015) [arXiv:1410.3012]
32. W. Beenakker, R. Höpker, M. Spira, P.M. Zerwas, Nucl. Phys. B **492**, 51 (1997) [arXiv:hep-ph/9610490]
33. A. Kulesza, L. Motyka, Phys. Rev. Lett. **102**, 111802 (2009) [arXiv:0807.2405]
34. A. Kulesza, L. Motyka, Phys. Rev. D **80**, 095004 (2009) [arXiv:0905.4749]
35. W. Beenakker, S. Brensing, M. Krämer, A. Kulesza, E. Laenen, I. Niessen, JHEP **12**, 041 (2009) [arXiv:0909.4418]
36. W. Beenakker, S. Brensing, M. Krämer, A. Kulesza, E. Laenen, L. Motyka, I. Niessen, Int. J. Mod. Phys. A **26**, 2637 (2011) [arXiv:1105.1110]
37. D. Orbaker, J. Phys. Conf. Ser. **219**, 032053 (2010)
38. CMS Collaboration, Comparison of the fast simulation of CMS with the first LHC data, CMS Detector Performance Summary CMS-DP-2010-039, CERN, 2010
39. CMS Collaboration, Jet performance in pp collisions at $\sqrt{s} = 7$ TeV, CMS Physics Analysis Summary CMS-PAS-JME-10-003, CERN, 2010
40. R.D. Ball et al., JHEP **04**, 040 (2015) [arXiv:1410.8849]
41. S. Catani, D. de Florian, M. Grazzini, P. Nason, JHEP **07**, 028 (2003) [arXiv:hep-ph/0306211]
42. M. Cacciari, S. Frixione, M.L. Mangano, P. Nason, G. Ridolfi, JHEP **04**, 068 (2004) [arXiv:hep-ph/0303085]
43. CMS Collaboration, Eur. Phys. J. C **73**, 2677 (2013) [arXiv:1308.1586]

44. J. Pumplin, D.R. Stump, J. Huston, H.-L. Lai, P. Nadolsky, W.-K. Tung, JHEP **07**, 012 (2002) [arXiv:hep-ph/0201195]
45. A.D. Martin, W.J. Stirling, R.S. Thorne, G. Watt, Eur. Phys. J. C **63**, 189 (2009) [arXiv:0901.0002]
46. R.D. Ball, V. Bertone, F. Cerutti, L. Del Debbio, S. Forte, A. Guffanti, J.I. Latorre, J. Rojo, M. Ubiali, Nucl. Phys. B **849**, 296 (2011) [arXiv:1101.1300]
47. S. Alekhin et al., The PDF4LHC Working Group Interim Report (2011) [arXiv:1101.0536]
48. M. Botje, J. Butterworth, A. Cooper-Sarkar, A. de Roeck, J. Feltesse, S. Forte, A. Glazov, J. Huston, R. McNulty, T. Sjöstrand, The PDF4LHC Working Group Interim Recommendations (2011) [arXiv:1101.0538]
49. Particle Data Group, K.A. Olive et al., Chin. Phys. C **38**, 090001 (2014)
50. Z. Bern, G. Diana, L.J. Dixon, F.F. Cordero, S. Hoeche, H. Ita, D.A. Kosower, D. Maitre, K.J. Ozeren, Phys. Rev. D **84**, 114002 (2011) [arXiv:1106.1423v2]
51. J.H. Kuhn, A. Kulesza, S. Pozzorini, M. Schulze, JHEP **03**, 059 (2006) [arXiv:hep-ph/0508253]
52. S. Ask, M.A. Parker, T. Sandoval, M.E. Shea, W.J. Stirling, JHEP **10**, 058 (2011) [arXiv:1107.2803]
53. Z. Bern, G. Diana, L.J. Dixon, F.F. Cordero, S. Hoeche, H. Ita, D.A. Kosower, D. Maitre, K.J. Ozeren, Phys. Rev. D **87**, 034026 (2013) [arXiv:1206.6064]
54. CMS Collaboration, JHEP **08**, 155 (2011) [arXiv:1106.4503]
55. CMS Collaboration, Phys. Rev. Lett. **109**, 171803 (2012) [arXiv:1207.1898]
56. Particle Data Group, Phys. Rev. D **86**, 010001 (2012)
57. CMS Collaboration, JINST **6**, 11002 (2011) [arXiv:1107.4277]
58. CMS Collaboration, JINST **12**, P02014 (2017) [arXiv:1607.03663]
59. CMS Collaboration, JHEP **1110**, 132 (2011) [arXiv:1107.4789]
60. SUS Data/MC Lepton Scale Factor Group, SUS Data/MC Lepton Scale Factors Muons [CMS Internal]İ (2015). https://twiki.cern.ch/twiki/bin/view/CMS/SUSLeptonSF#Muons_AN1
61. J. Butterworth et al., J. Phys. G **43**, 023001 (2016) [arXiv:1510.03865]
62. CMS Statistics Committee, Asymmetric Error Bars for Poisson Event Counts [CMS Internal] (2015). https://twiki.cern.ch/twiki/bin/view/CMS/PoissonErrorBars
63. G. Cowan, K. Cranmer, E. Gross, O. Vitells, Eur. Phys. J. C **71**, 1554 (2011) [arXiv:1007.1727] [Erratum: Eur. Phys. J. C **73**, 2501 (2013)]
64. T. Junk, Nucl. Instrum. Methods A **434**, 435 (1999) [arXiv:hep-ex/9902006]
65. A.L. Read, J. Phys. G **28**, 2693 (2002)
66. ATLAS and CMS Collaborations, Procedure for the LHC Higgs boson search combination in Summer 2011, Tech. Rep. CMS-NOTE-2011-005, ATL-PHYS-PUB-2011-11 (2011)
67. CMS Collaboration, JHEP **05**, 078 (2015) [arXiv:1502.04358]
68. C. Borschensky, M. Krämer, A. Kulesza, M. Mangano, S. Padhi, T. Plehn, X. Portell, Eur. Phys. J. C **74**, 3174 (2014) [arXiv:1407.5066]

Chapter 8
Summary

The cosmological constant problem and a set of suggested solutions have been reviewed. Two of the proposed solutions have been described in detail in this dissertation.

A Lorentz gauge formulation of gravity has been presented in which the metric has no dynamics. Here, the equivalence principle that ensures the existence of a free-falling frame whose coordinate system is locally Minkowskian has been used. Therefore, at any point in space-time there always exists a frame that is both of the coordinate and Lorentz types. This leads to the fact that a tetrad field can be split into two parts, namely, $e_{i\mu} = \eta^{\bar{k}\bar{l}} e_{i\bar{k}} e_{\bar{l}\mu}$, where the free-falling frame has been indicated with a bar. A variation in the tetrad field can therefore stem from either of the two constituents. One leads to Einstein's theory of gravity while the other leads to a formulation with no dynamics for the metric. Because of the spectacular success of the standard model of particle physics, both in terms of experiments and renormalizability, the formulation that is more analogous to the standard model, the latter case, has been investigated. In this framework, it has been shown that a variation of the action with respect to the tetrad results in the trivial angular momentum conservation equation where there exists no source for the resulting field equations. Consequently, the field equations have been derived by varying the action with respect to the spin connections, where the Lagrange multiplier method has been used to impose the tetrad postulate and eliminate the tetrad as a function of the spin connections. A special case of the theory has been presented where the Schwarzschild metric is an exact solution. Moreover, a homogeneous and isotropic space has also been studied within this special case. It is shown that there exists a natural exponentially expanding vacuum solution where the cosmological constant or any other type of dark energy is absent. In addition, quantization of the theory has been studied briefly and all of the basic Feynman diagrams have been derived. It has been shown that the theory is power-counting renormalizable if a certain condition is met.

A. Borzou, *Theoretical and Experimental Approaches to Dark Energy and the Cosmological Constant Problem*, Springer Theses,
https://doi.org/10.1007/978-3-319-69632-4_8

Another well-motivated theory, which can provide some solutions to the cosmological constant problem, is supersymmetry. Following a brief introduction to supersymmetry, a search is presented for an anomalously high rate of events with four or more jets, no identified isolated electron or muon or isolated charged track, large scalar sum H_{T} of jet transverse momenta, and large missing transverse momentum, where this latter quantity is measured with the variable $H_{\mathrm{T}}^{\mathrm{miss}}$, the magnitude of the vector sum of jet transverse momenta. The search is based on a sample of proton-proton collision data collected at $\sqrt{s} = 13\,\mathrm{TeV}$ with the CMS detector at the CERN LHC in 2015, corresponding to an integrated luminosity of 2.3 fb^{-1}. The principal standard model backgrounds, from events with top quarks, W bosons and jets, Z bosons and jets, and QCD multijet production, are evaluated using control samples collected with proton-proton collision data. The study is performed in the framework of a global likelihood fit in which the observed numbers of events in 72 exclusive bins in a four-dimensional array of $H_{\mathrm{T}}^{\mathrm{miss}}$, the number of jets, the number of tagged bottom quark jets, and H_{T}, are compared to the standard model predictions. The standard model background estimates are found to agree with the observed numbers of events within the uncertainties. The results are interpreted with simplified models that, in the context of supersymmetry, correspond to gluino pair production followed by the decay of each gluino to an undetected lightest supersymmetric particle (LSP) neutralino $\tilde{\chi}_1^0$ and to a bottom quark-antiquark pair (T1bbbb model), a top quark-antiquark pair (T1tttt model), or a light-flavored quark-antiquark pair (T1qqqq model). Also considered is a scenario corresponding to gluino pair production followed by the decay of each gluino to a light-flavored quark-antiquark pair and to either a next-to-lightest neutralino $\tilde{\chi}_2^0$ or the lightest chargino $\tilde{\chi}_1^{\pm}$, with $\tilde{\chi}_2^0 \to Z\tilde{\chi}_1^0$ or $\tilde{\chi}_1^{\pm} \to W^{\pm}\tilde{\chi}_1^0$ (T5qqqqVV model). Using the gluino-pair production cross section computed to NLO + NLL accuracy as a reference, and for a massless LSP, gluinos with masses below 1600, 1550, 1440, and 1450 GeV for the four scenarios, respectively, are excluded. These results significantly extend the limits from previous searches.

Appendix: Prefit Background Predictions of the Supersymmetry Search

See Tables 1, 2, and 3.

Table 1 Observed numbers of events and prefit background predictions for $4 \leq N_{\text{jet}} \leq 6$

Bin	$H_{\text{T}}^{\text{miss}}$ (GeV)	H_{T} (GeV)	$N_{\text{b-jet}}$	Lost-e/μ	$\tau \longrightarrow$ had	$Z \longrightarrow \nu\bar{\nu}$	QCD	Total pred.	Obs.
1	200–500	500–800	0	$318.76^{+11.84+28.74}_{-11.82-27.67}$	$310.30^{+10.78+19.37}_{-10.77-18.87}$	$631.79^{+13.20+102.80}_{-13.20-81.76}$	$219.89^{+3.82+109.99}_{-3.75-109.99}$	$1480.74^{+26.46+154.23}_{-26.43-141.08}$	1602
2	200–500	800–1200	0	$59.15^{+4.33+5.47}_{-4.29-5.28}$	$69.08^{+5.21+5.67}_{-5.19-5.59}$	$144.92^{+6.29+25.92}_{-6.29-20.42}$	$99.78^{+1.78+33.52}_{-1.75-33.52}$	$372.93^{+11.57+43.06}_{-11.52-40.00}$	390
3	200–500	1200+	0	$13.84^{+2.25+1.38}_{-2.17-1.30}$	$14.38^{+2.57+1.56}_{-2.53-1.51}$	$31.36^{+2.95+11.93}_{-2.95-8.33}$	$90.43^{+1.95+24.21}_{-1.91-24.21}$	$150.01^{+5.98+27.07}_{-5.87-25.68}$	149
4	500–750	500–800	0	$11.49^{+1.93+1.57}_{-1.84-1.53}$	$8.92^{+1.72+1.33}_{-1.66-1.32}$	$61.62^{+4.41+18.46}_{-4.41-13.29}$	$0.38^{+0.12+0.42}_{-0.09-0.29}$	$82.40^{+5.73+18.57}_{-5.64-13.45}$	120
5	500–750	1200+	0	$1.95^{+1.04+0.50}_{-0.90-0.50}$	$0.56^{+0.52+0.15}_{-0.25-0.15}$	$5.45^{+1.32+2.12}_{-1.32-1.51}$	$0.97^{+0.18+1.02}_{-0.15-0.82}$	$8.92^{+2.05+2.41}_{-1.76-1.80}$	13
6	750+	800+	0	$1.39^{+0.93+0.24}_{-0.77-0.23}$	$1.77^{+0.99+0.34}_{-0.88-0.33}$	$10.35^{+1.80+5.81}_{-1.80-4.06}$	$0.24^{+0.09+0.26}_{-0.06-0.18}$	$13.75^{+2.64+5.83}_{-2.45-4.08}$	12
7	200–500	500–800	1	$171.23^{+8.42+16.95}_{-8.39-16.43}$	$205.71^{+8.53+12.98}_{-8.52-12.60}$	$127.47^{+20.90+30.82}_{-20.90-28.14}$	$69.19^{+2.20+37.42}_{-2.13-37.42}$	$573.60^{+27.00+52.72}_{-26.97-51.19}$	499
8	200–500	800–1200	1	$31.37^{+3.98+2.95}_{-3.94-2.86}$	$30.41^{+3.19+2.01}_{-3.16-1.93}$	$29.24^{+4.92+7.40}_{-4.92-6.66}$	$36.40^{+1.11+14.33}_{-1.07-14.33}$	$127.42^{+8.77+16.49}_{-8.70-16.17}$	123
9	200–500	1200+	1	$6.29^{+1.77+0.84}_{-1.64-0.82}$	$8.86^{+2.08+0.90}_{-2.03-0.83}$	$6.33^{+1.19+2.66}_{-1.19-2.03}$	$32.49^{+1.19+11.01}_{-1.15-11.01}$	$53.96^{+4.20+11.39}_{-4.03-11.26}$	44
10	500–750	500–800	1	$3.07^{+1.17+0.60}_{-1.00-0.59}$	$2.64^{+0.96+0.49}_{-0.85-0.48}$	$12.43^{+2.21+4.34}_{-2.21-3.48}$	$0.07^{+0.04+0.09}_{-0.02-0.05}$	$18.21^{+3.07+4.40}_{-2.88-3.57}$	22
11	500–750	1200+	1	$0.00^{+0.52+0.00}_{-0.00-0.00}$	$0.07^{+0.46+0.02}_{-0.04-0.02}$	$1.10^{+0.32+0.47}_{-0.32-0.36}$	$0.38^{+0.12+0.41}_{-0.09-0.29}$	$1.55^{+1.04+0.62}_{-0.34-0.46}$	1
12	750+	800+	1	$0.00^{+0.50+0.00}_{-0.00-0.00}$	$0.54^{+0.56+0.13}_{-0.32-0.13}$	$2.09^{+0.50+1.23}_{-0.50-0.90}$	$0.02^{+0.06+0.06}_{-0.00-0.02}$	$2.64^{+1.18+1.24}_{-0.59-0.91}$	2
13	200–500	500–800	2	$71.85^{+6.08+7.16}_{-6.05-6.67}$	$77.18^{+4.98+5.48}_{-4.96-5.34}$	$28.08^{+8.07+12.45}_{-8.07-12.14}$	$15.94^{+1.13+8.76}_{-1.06-8.76}$	$193.05^{+13.74+17.46}_{-13.69-17.24}$	202
14	200–500	800–1200	2	$18.80^{+4.79+2.53}_{-4.75-2.20}$	$17.30^{+2.67+1.29}_{-2.63-1.25}$	$6.44^{+1.87+2.90}_{-1.87-2.81}$	$9.49^{+0.61+3.80}_{-0.57-3.80}$	$52.04^{+7.71+5.41}_{-7.63-5.36}$	45
15	200–500	1200+	2	$2.06^{+1.20+0.23}_{-0.98-0.22}$	$3.31^{+1.28+0.34}_{-1.20-0.32}$	$1.39^{+0.42+0.78}_{-0.42-0.68}$	$5.57^{+0.53+1.99}_{-0.49-1.99}$	$12.33^{+2.58+2.17}_{-2.27-2.14}$	15
16	500–750	500–800	2	$1.90^{+1.84+0.65}_{-1.72-0.17}$	$2.26^{+0.94+0.86}_{-0.82-0.86}$	$2.74^{+0.81+1.40}_{-0.81-1.27}$	$0.03^{+0.02+0.04}_{-0.01-0.02}$	$6.92^{+2.90+1.65}_{-2.67-1.54}$	5
17	500–750	1200+	2	$3.33^{+3.37+1.35}_{-3.33-0.00}$	$0.07^{+0.46+0.02}_{-0.05-0.01}$	$0.24^{+0.09+0.14}_{-0.09-0.12}$	$0.07^{+0.08+0.09}_{-0.04-0.03}$	$3.71^{+3.83+0.16}_{-3.38-0.12}$	0
18	750+	800+	2	$0.00^{+0.46+0.00}_{-0.00-0.00}$	$0.04^{+0.46+0.02}_{-0.03-0.01}$	$0.46^{+0.15+0.32}_{-0.15-0.26}$	$0.03^{+0.06+0.05}_{-0.02-0.01}$	$0.53^{+0.93+0.32}_{-0.16-0.26}$	1
19	200–500	500–800	3+	$6.27^{+1.76+0.79}_{-1.65-0.78}$	$10.82^{+2.17+1.66}_{-2.12-1.62}$	$6.48^{+3.77+3.00}_{-3.77-2.71}$	$1.21^{+0.37+0.82}_{-0.29-0.82}$	$24.78^{+5.46+3.59}_{-5.34-3.35}$	17
20	200–500	800–1200	3+	$0.24^{+0.67+0.03}_{-0.24-0.00}$	$1.10^{+0.61+0.15}_{-0.40-0.14}$	$1.49^{+0.87+0.70}_{-0.87-0.62}$	$0.70^{+0.20+0.37}_{-0.16-0.37}$	$3.53^{+1.56+0.80}_{-1.09-0.74}$	7
21	200–500	1200+	3+	$0.80^{+0.91+0.13}_{-0.57-0.13}$	$0.11^{+0.46+0.02}_{-0.05-0.02}$	$0.32^{+0.19+0.19}_{-0.19-0.13}$	$0.72^{+0.23+0.36}_{-0.18-0.36}$	$1.95^{+1.40+0.43}_{-0.67-0.40}$	3
22	500–750	500–800	3+	$0.00^{+0.63+0.00}_{-0.00-0.00}$	$0.03^{+0.46+0.01}_{-0.01-0.01}$	$0.63^{+0.37+0.33}_{-0.37-0.26}$	$0.05^{+0.11+0.09}_{-0.04-0.01}$	$0.71^{+1.15+0.34}_{-0.37-0.26}$	0
23	500–750	1200+	3+	$0.00^{+0.77+0.00}_{-0.00-0.00}$	$0.00^{+0.46+0.00}_{-0.00-0.00}$	$0.06^{+0.04+0.03}_{-0.04-0.02}$	$0.00^{+0.05+0.02}_{-0.00-0.00}$	$0.06^{+1.23+0.04}_{-0.04-0.02}$	0
24	750+	800+	3+	$0.00^{+0.58+0.00}_{-0.00-0.00}$	$0.00^{+0.46+0.00}_{-0.00-0.00}$	$0.11^{+0.06+0.08}_{-0.06-0.04}$	$0.00^{+0.04+0.02}_{-0.00-0.00}$	$0.11^{+1.04+0.08}_{-0.06-0.04}$	0

These results are displayed in the leftmost section of Fig. 7.21. The first uncertainty is statistical and the second systematic

A. Borzou, *Theoretical and Experimental Approaches to Dark Energy and the Cosmological Constant Problem*, Springer Theses,
https://doi.org/10.1007/978-3-319-69632-4

Table 2 Observed numbers of events and prefit background predictions for $7 \leq N_{\text{jet}} \leq 8$

Bin	$H_{\text{T}}^{\text{miss}}$ (GeV)	H_{T} (GeV)	$N_{\text{b-jet}}$	Lost-e/μ	$\tau \rightarrow$ had	$Z \rightarrow \nu\bar{\nu}$	QCD	Total pred.	Obs.
25	200–500	500–800	0	$18.78^{+3.08+2.31}_{-3.05-2.20}$	$24.50^{+2.68+2.02}_{-2.64-2.00}$	$27.40^{+2.78+6.72}_{-2.78-5.14}$	$14.05^{+1.72+8.19}_{-1.54-8.19}$	$84.72^{+6.62+11.00}_{-6.52-10.12}$	85
26	200–500	800–1200	0	$12.53^{+1.83+2.19}_{-1.79-2.17}$	$15.60^{+2.26+1.27}_{-2.22-1.25}$	$17.29^{+2.25+4.19}_{-2.25-3.17}$	$16.29^{+1.20+7.12}_{-1.12-7.12}$	$61.72^{+4.83+8.63}_{-4.73-8.19}$	60
27	200–500	1200+	0	$2.88^{+1.15+0.32}_{-1.07-0.31}$	$3.50^{+1.29+0.31}_{-1.20-0.30}$	$6.03^{+1.29+2.34}_{-1.29-1.66}$	$23.01^{+1.56+8.75}_{-1.46-8.75}$	$35.42^{+3.17+9.07}_{-2.99-8.92}$	42
28	500–750	500–800	0	$0.53^{+0.45+0.14}_{-0.26-0.13}$	$0.81^{+0.66+0.19}_{-0.47-0.19}$	$0.36^{+0.36+0.12}_{-0.36-0.00}$	$0.06^{+0.10+0.09}_{-0.04-0.02}$	$1.75^{+1.17+0.28}_{-0.82-0.23}$	1
29	500–750	1200+	0	$1.03^{+0.88+0.33}_{-0.80-0.24}$	$1.44^{+0.93+0.29}_{-0.80-0.29}$	$0.60^{+0.43+0.26}_{-0.43-0.18}$	$0.26^{+0.17+0.30}_{-0.11-0.15}$	$3.34^{+1.87+0.54}_{-1.66-0.44}$	1
30	750+	800+	0	$0.17^{+0.38+0.09}_{-0.17-0.00}$	$0.17^{+0.49+0.11}_{-0.17-0.00}$	$0.56^{+0.40+0.34}_{-0.40-0.16}$	$0.19^{+0.16+0.23}_{-0.09-0.10}$	$1.09^{+0.97+0.41}_{-0.53-0.19}$	1
31	200–500	500–800	1	$25.79^{+2.93+3.13}_{-2.90-3.04}$	$31.75^{+2.96+2.34}_{-2.93-2.30}$	$11.68^{+2.24+3.63}_{-2.24-3.82}$	$8.08^{+1.36+5.05}_{-1.18-5.05}$	$77.30^{+6.45+7.29}_{-6.35-7.39}$	63
32	200–500	800–1200	1	$9.01^{+1.63+1.28}_{-1.58-1.10}$	$14.38^{+2.02+1.35}_{-1.97-1.34}$	$7.37^{+1.54+2.27}_{-1.54-2.39}$	$7.57^{+0.85+3.69}_{-0.76-3.69}$	$38.34^{+4.06+4.67}_{-3.94-4.73}$	43
33	200–500	1200+	1	$3.25^{+1.12+0.36}_{-1.01-0.34}$	$6.33^{+1.49+0.67}_{-1.42-0.66}$	$2.57^{+0.69+1.11}_{-0.69-0.99}$	$13.70^{+1.22+5.93}_{-1.13-5.93}$	$25.85^{+2.96+6.08}_{-2.77-6.06}$	29
34	500–750	500–800	1	$0.46^{+0.49+0.11}_{-0.27-0.11}$	$0.51^{+0.55+0.11}_{-0.29-0.11}$	$0.15^{+0.16+0.06}_{-0.15-0.00}$	$0.00^{+0.12+0.05}_{-0.00-0.00}$	$1.12^{+1.06+0.17}_{-0.58-0.16}$	2
35	500–750	1200+	1	$0.00^{+0.40+0.00}_{-0.00-0.00}$	$0.25^{+0.49+0.05}_{-0.18-0.05}$	$0.26^{+0.19+0.12}_{-0.19-0.07}$	$0.12^{+0.14+0.16}_{-0.07-0.05}$	$0.63^{+0.92+0.21}_{-0.27-0.10}$	2
36	750+	800+	1	$0.00^{+0.45+0.00}_{-0.00-0.00}$	$0.02^{+0.46+0.01}_{-0.01-0.00}$	$0.24^{+0.17+0.15}_{-0.17-0.07}$	$0.00^{+0.08+0.03}_{-0.00-0.00}$	$0.25^{+0.93+0.16}_{-0.17-0.07}$	1
37	200–500	500–800	2	$13.15^{+2.16+1.54}_{-2.11-1.51}$	$16.03^{+1.87+1.20}_{-1.81-1.18}$	$4.79^{+1.46+2.36}_{-1.46-2.43}$	$0.16^{+0.32+0.57}_{-0.00-0.16}$	$34.13^{+4.29+3.09}_{-4.18-3.10}$	32
38	200–500	800–1200	2	$6.33^{+1.29+0.74}_{-1.22-0.71}$	$10.73^{+1.82+0.89}_{-1.76-0.88}$	$3.03^{+0.95+1.48}_{-0.95-1.53}$	$2.15^{+0.48+1.12}_{-0.40-1.12}$	$22.24^{+3.29+2.18}_{-3.15-2.21}$	17
39	200–500	1200+	2	$1.73^{+0.79+0.20}_{-0.62-0.19}$	$1.89^{+0.88+0.18}_{-0.75-0.18}$	$1.06^{+0.38+0.61}_{-0.38-0.58}$	$3.55^{+0.64+1.64}_{-0.55-1.64}$	$8.22^{+1.82+1.77}_{-1.52-1.76}$	4
40	500–750	500–800	2	$0.00^{+0.39+0.00}_{-0.00-0.00}$	$0.04^{+0.46+0.01}_{-0.02-0.01}$	$0.06^{+0.07+0.03}_{-0.06-0.00}$	$0.00^{+0.12+0.05}_{-0.00-0.00}$	$0.10^{+0.86+0.06}_{-0.06-0.01}$	0
41	500–750	1200+	2	$0.00^{+0.43+0.00}_{-0.00-0.00}$	$0.07^{+0.47+0.04}_{-0.07-0.00}$	$0.11^{+0.08+0.06}_{-0.08-0.02}$	$0.03^{+0.11+0.05}_{-0.02-0.01}$	$0.21^{+0.90+0.08}_{-0.11-0.03}$	1
42	750+	800+	2	$0.00^{+0.34+0.00}_{-0.00-0.00}$	$0.13^{+0.48+0.06}_{-0.13-0.00}$	$0.10^{+0.07+0.07}_{-0.07-0.02}$	$0.00^{+0.08+0.03}_{-0.00-0.00}$	$0.23^{+0.82+0.08}_{-0.15-0.02}$	0
43	200–500	500–800	3+	$3.93^{+1.25+0.46}_{-1.16-0.45}$	$5.78^{+1.31+0.68}_{-1.23-0.67}$	$2.54^{+1.50+1.76}_{-1.50-1.04}$	$1.09^{+0.62+0.86}_{-0.41-0.68}$	$13.34^{+3.03+2.12}_{-2.85-1.48}$	3
44	200–500	800–1200	3+	$0.44^{+0.49+0.05}_{-0.25-0.05}$	$1.66^{+0.76+0.26}_{-0.60-0.26}$	$1.60^{+0.96+1.11}_{-0.96-0.65}$	$0.60^{+0.30+0.39}_{-0.21-0.39}$	$4.30^{+1.60+1.20}_{-1.30-0.80}$	4
45	200–500	1200+	3+	$0.66^{+0.72+0.12}_{-0.52-0.12}$	$0.65^{+0.61+0.10}_{-0.40-0.10}$	$0.56^{+0.35+0.42}_{-0.35-0.21}$	$0.04^{+0.19+0.12}_{-0.00-0.04}$	$1.91^{+1.39+0.47}_{-0.99-0.27}$	1
46	500–750	500–800	3+	$0.00^{+0.52+0.00}_{-0.00-0.00}$	$0.00^{+0.46+0.00}_{-0.00-0.00}$	$0.03^{+0.04+0.02}_{-0.03-0.00}$	$0.04^{+0.09+0.07}_{-0.03-0.01}$	$0.07^{+0.98+0.07}_{-0.05-0.01}$	0
47	500–750	1200+	3+	$0.00^{+0.47+0.00}_{-0.00-0.00}$	$0.00^{+0.46+0.00}_{-0.00-0.00}$	$0.06^{+0.05+0.04}_{-0.05-0.00}$	$0.00^{+0.09+0.03}_{-0.00-0.00}$	$0.06^{+0.94+0.05}_{-0.05-0.00}$	0
48	750+	800+	3+	$0.00^{+0.61+0.00}_{-0.00-0.00}$	$0.01^{+0.46+0.01}_{-0.01-0.00}$	$0.05^{+0.05+0.05}_{-0.05-0.00}$	$0.00^{+0.08+0.03}_{-0.00-0.00}$	$0.06^{+1.07+0.06}_{-0.05-0.00}$	0

These results are displayed in the central section of Fig. 7.21. The first uncertainty is statistical and the second systematic

Table 3 Observed numbers of events and prefit background predictions for $N_{\text{jet}} \geq 9$

Bin	$H_{\text{T}}^{\text{miss}}$ (GeV)	H_{T} (GeV)	$N_{\text{b-jet}}$	Lost-e/μ	$\tau \rightarrow$ had	$Z \rightarrow \nu\bar{\nu}$	QCD	Total pred.	Obs.
49	200–500	500–800	0	$0.99^{+0.59+0.21}_{-0.45-0.21}$	$0.61^{+0.52+0.09}_{-0.23-0.09}$	$0.26^{+0.26+0.12}_{-0.26-0.00}$	$0.92^{+0.54+0.80}_{-0.35-0.57}$	$2.77^{+1.26+0.84}_{-0.81-0.62}$	2
50	200–500	800–1200	0	$2.12^{+0.72+0.33}_{-0.62-0.33}$	$3.92^{+1.17+0.41}_{-1.08-0.41}$	$2.14^{+0.81+0.81}_{-0.81-0.64}$	$0.78^{+0.31+0.56}_{-0.23-0.55}$	$8.96^{+2.08+1.12}_{-1.90-0.99}$	12
51	200–500	1200+	0	$0.58^{+0.54+0.08}_{-0.35-0.08}$	$1.05^{+0.76+0.16}_{-0.61-0.15}$	$0.42^{+0.30+0.18}_{-0.30-0.12}$	$3.93^{+0.67+2.45}_{-0.58-2.45}$	$5.98^{+1.49+2.46}_{-1.15-2.46}$	8
52	500–750	500–800	0	$0.00^{+0.34+0.00}_{-0.00-0.00}$	$0.00^{+0.46+0.00}_{-0.00-0.00}$	$0.15^{+0.15+0.11}_{-0.15-0.00}$	$0.00^{+0.11+0.04}_{-0.00-0.00}$	$0.15^{+0.82+0.11}_{-0.15-0.00}$	0
53	500–750	1200+	0	$0.14^{+0.36+0.05}_{-0.14-0.00}$	$0.02^{+0.46+0.01}_{-0.02-0.00}$	$0.00^{+0.76+0.00}_{-0.00-0.00}$	$0.00^{+0.09+0.04}_{-0.00-0.00}$	$0.17^{+1.13+0.04}_{-0.17-0.00}$	0
54	750+	800+	0	$0.00^{+0.28+0.00}_{-0.00-0.00}$	$0.00^{+0.46+0.00}_{-0.00-0.00}$	$0.00^{+0.79+0.00}_{-0.00-0.00}$	$0.00^{+0.08+0.03}_{-0.00-0.00}$	$0.00^{+1.09+0.03}_{-0.00-0.00}$	0
55	200–500	500–800	1	$1.36^{+0.66+0.20}_{-0.53-0.19}$	$1.58^{+0.71+0.19}_{-0.54-0.19}$	$0.19^{+0.19+0.10}_{-0.19-0.00}$	$0.09^{+0.22+0.15}_{-0.07-0.02}$	$3.22^{+1.40+0.32}_{-1.08-0.27}$	6
56	200–500	800–1200	1	$3.19^{+0.99+0.53}_{-0.91-0.52}$	$4.05^{+1.17+0.37}_{-1.08-0.36}$	$1.57^{+0.64+0.70}_{-0.64-0.67}$	$0.88^{+0.34+0.65}_{-0.25-0.63}$	$9.68^{+2.28+1.15}_{-2.10-1.11}$	4
57	200–500	1200+	1	$1.70^{+0.85+0.25}_{-0.73-0.25}$	$1.41^{+0.79+0.25}_{-0.65-0.25}$	$0.31^{+0.22+0.15}_{-0.22-0.08}$	$2.41^{+0.54+1.61}_{-0.45-1.61}$	$5.83^{+1.74+1.65}_{-1.46-1.65}$	3
58	500–750	500–800	1	$0.00^{+0.40+0.00}_{-0.00-0.00}$	$0.05^{+0.46+0.02}_{-0.05-0.00}$	$0.11^{+0.11+0.08}_{-0.11-0.00}$	$0.00^{+0.11+0.04}_{-0.00-0.00}$	$0.16^{+0.88+0.09}_{-0.12-0.00}$	0
59	500–750	1200+	1	$0.00^{+0.41+0.00}_{-0.00-0.00}$	$0.15^{+0.48+0.04}_{-0.14-0.00}$	$0.00^{+0.66+0.00}_{-0.00-0.00}$	$0.00^{+0.09+0.03}_{-0.00-0.00}$	$0.15^{+1.11+0.03}_{-0.14-0.00}$	1
60	750+	800+	1	$0.00^{+0.33+0.00}_{-0.00-0.00}$	$0.00^{+0.46+0.00}_{-0.00-0.00}$	$0.00^{+0.68+0.00}_{-0.00-0.00}$	$0.00^{+0.08+0.03}_{-0.00-0.00}$	$0.00^{+1.05+0.03}_{-0.00-0.00}$	0
61	200–500	500–800	2	$1.38^{+0.74+0.18}_{-0.62-0.17}$	$1.51^{+0.77+0.15}_{-0.61-0.15}$	$0.10^{+0.11+0.07}_{-0.10-0.00}$	$0.00^{+0.22+0.11}_{-0.00-0.00}$	$3.00^{+1.53+0.27}_{-1.23-0.23}$	3
62	200–500	800–1200	2	$1.39^{+0.68+0.20}_{-0.57-0.20}$	$2.20^{+0.92+0.20}_{-0.80-0.20}$	$0.87^{+0.41+0.54}_{-0.41-0.46}$	$0.26^{+0.22+0.24}_{-0.13-0.13}$	$4.72^{+1.67+0.65}_{-1.43-0.55}$	1
63	200–500	1200+	2	$0.28^{+0.48+0.04}_{-0.20-0.04}$	$1.40^{+0.83+0.19}_{-0.70-0.19}$	$0.17^{+0.13+0.11}_{-0.13-0.04}$	$1.38^{+0.45+0.95}_{-0.35-0.95}$	$3.24^{+1.40+0.98}_{-0.97-0.97}$	2
64	500–750	500–800	2	$0.00^{+0.36+0.00}_{-0.00-0.00}$	$0.00^{+0.46+0.00}_{-0.00-0.00}$	$0.06^{+0.06+0.05}_{-0.06-0.00}$	$0.00^{+0.11+0.04}_{-0.00-0.00}$	$0.06^{+0.83+0.07}_{-0.06-0.00}$	0
65	500–750	1200+	2	$0.00^{+0.45+0.00}_{-0.00-0.00}$	$0.01^{+0.46+0.00}_{-0.01-0.00}$	$0.00^{+0.52+0.00}_{-0.00-0.00}$	$0.00^{+0.09+0.03}_{-0.00-0.00}$	$0.01^{+1.05+0.03}_{-0.01-0.00}$	0
66	750+	800+	2	$0.00^{+0.43+0.00}_{-0.00-0.00}$	$0.00^{+0.46+0.00}_{-0.00-0.00}$	$0.00^{+0.52+0.00}_{-0.00-0.00}$	$0.00^{+0.08+0.03}_{-0.00-0.00}$	$0.00^{+1.04+0.03}_{-0.00-0.00}$	0
67	200–500	500–800	3+	$0.30^{+0.48+0.05}_{-0.21-0.05}$	$1.13^{+0.79+0.16}_{-0.64-0.16}$	$0.02^{+0.03+0.03}_{-0.02-0.00}$	$0.00^{+0.22+0.09}_{-0.00-0.00}$	$1.46^{+1.29+0.20}_{-0.85-0.17}$	0
68	200–500	800–1200	3+	$1.92^{+1.38+0.33}_{-1.33-0.32}$	$0.70^{+0.60+0.09}_{-0.38-0.09}$	$0.18^{+0.13+0.24}_{-0.13-0.06}$	$0.27^{+0.22+0.25}_{-0.13-0.14}$	$3.08^{+1.99+0.48}_{-1.72-0.37}$	1
69	200–500	1200+	3+	$0.46^{+0.64+0.06}_{-0.46-0.00}$	$0.32^{+0.54+0.05}_{-0.28-0.04}$	$0.04^{+0.03+0.05}_{-0.03-0.00}$	$0.04^{+0.10+0.07}_{-0.03-0.01}$	$0.86^{+1.19+0.09}_{-0.75-0.04}$	0
70	500–750	500–800	3+	$0.13^{+0.47+0.05}_{-0.13-0.00}$	$0.00^{+0.46+0.00}_{-0.00-0.00}$	$0.01^{+0.02+0.02}_{-0.01-0.00}$	$0.00^{+0.11+0.04}_{-0.00-0.00}$	$0.14^{+0.93+0.04}_{-0.13-0.00}$	0
71	500–750	1200+	3+	$0.00^{+0.41+0.00}_{-0.00-0.00}$	$0.00^{+0.46+0.00}_{-0.00-0.00}$	$0.00^{+0.30+0.00}_{-0.00-0.00}$	$0.00^{+0.09+0.02}_{-0.00-0.00}$	$0.00^{+0.93+0.02}_{-0.00-0.00}$	0
72	750+	800+	3+	$0.00^{+0.44+0.00}_{-0.00-0.00}$	$0.00^{+0.46+0.00}_{-0.00-0.00}$	$0.00^{+0.28+0.00}_{-0.00-0.00}$	$0.00^{+0.08+0.03}_{-0.00-0.00}$	$0.00^{+0.95+0.03}_{-0.00-0.00}$	0

These results are displayed in the rightmost section of Fig. 7.21. The first uncertainty is statistical and the second systematic